uc3m | Universidad Carlos III de Madrid

TESIS DOCTORAL

Modeling and simulation of bacterial biofilm growth

Author:
Sergei Iakunin

Tutor/Director:
Luis L. Bonilla

Doctorado en Ingeniería Matemática

Departamento de Ciencia e Ingeniería de Materiales e Ingeniería Química
Universidad Carlos III de Madrid

Leganés, Spain
October 2018

Acknowledgments

The four years I spent doing my PhD in the Universidad Carlos III in Madrid for me were a time full of inspiring challenges and interesting discovers, a time when I had a chance to apply all I had got to know during my master study and to open a lot of new things. I am very thankful to my supervisor Luis Bonilla for having suggested me so multifacet problem about simulation of biofilm growth, for helpful and interesting discussions we had, and for providing me the opportunity to study abroad that itself was an adventure. I am also grateful to Ana Carpio for her advices and for inviting me to give a talk during her mini-course in the Fields Institute at Toronto, it was a great experience for me. Before I came to Madrid I had no idea about biofilms so I very much appreciate David Espeso's help who explained to me a lot about bacteria and shared with me interesting photos from experiments demonstrating how these structures may look like. And I am very thankful to those without whom I would probably never had come to Spain: to Sergei Lupuleac who put me in contact with Luis and helped me a lot with paperwork necessary for Spanish visa, and to Miguel Ruíz who was very helpful when I had already come to Madrid and thanks to whom I could adapt very well to a new place.

During the work on my PhD thesis I had a chance to meet many interesting people and had fruitful scientific discussions. I am grateful to all my colleagues in the Group of Modelling, Numerical Simulation and Industrial Mathematics and Instituto Gregorio Millán Barbany for creating a friendly and creative atmosphere, for organizing many seminars both complex, related to the advancing frontier of science, and also more informal and amusing ones, which allow to look at things of the daily life under a different angle. I am thankful to my colleagues from Saint Petersburg State Polytechnical University for their always warm welcomes and for providing me the opportunity to give a talk, to present and discuss my results. I am also thankful to people with whom I had a chance to talk during the conferences and who helped me to see a bigger picture about research in bacterial biofilms. Especially I am grateful to Messoud Efendiev and Vitali Vougalter who explained me how to apply operator theory to prove existence of solution for differential equations; without them I would probably had never done that part of my thesis. And I am also thankful to Maria Rosaria Mattei who showed me the whole picture about the simulation of biofilms: I wrote my review in this thesis under the inspiration of her article and thanks to our discussion.

Finally I want to thank friends and my parents who supported me during all this time. It would probably take another 100 pages to name everybody who helped and encouraged me, to mention all the fruitful discussions, sem-

inars, and lectures, so please excuse me if I forgot somebody in this unfairly short acknowledgement for I was trying to do my best.

This work has been supported by the Ministerio de Economía y Competitividad grants MTM2014-56948-C2-2-P and MTM2017-84446-C2-2-R.

Published and submitted articles and contributions

This thesis partially contains the work published in the following paper:

- **Iakunin, S.**, Bonilla, L.L. (2018). Variational formulation, asymptotic analysis, and finite element simulation of wrinkling phenomena in modified plate equations modeling biofilms growing on agar substrates. *Comp. Methods in Appl. Mech. and Engineering*, 333:257–286, `https://doi.org/10.1016/j.cma.2018.01.033`.

  Parts of this work are included into the following chapters of the thesis:

  - chapter 0;
  - chapter 2, sections 2 and 3;
  - chapter 3, sections 2, 3, and 4;
  - chapter 4, sections 2 and 3;
  - chapter 5, section 1;
  - chapter 6, section 1 and 3;
  - chapter 7, section 1,2, and 4;
  - chapter 9.

  The material is not always singled out with typographic means and references.

Contents

Chapter 0

Introduction

Bacteria are one of the most simplest life form in nature. They are unicellular organisms a few micrometers in length that lacks any membrane-bound organelle such as nucleus or mitochondria. Even though bacteria are very small they play crucial role for all life on Earth. Firstly bacteria are the main agents in nitrogen cycle: a process of supplying plants, animals, and other organisms by nitrogen necessary for proteins, DNA, and chlorophyll. There are plenty of nitrogen on our planet but it mostly exists in biologically inert gas N_2. Bacteria are the only organisms which can turn this gas into nitrates suitable for consumption by more complex life forms. Furthermore bacteria remove toxic nitrates emergent due to metabolic activity and turn them back into N_2 finishing thereby the cycle. Secondly bacteria have a lot of symbiotic relationships with plants and animals. Quite rare but facinating example is Hawaiian squid *Euprymna scolopes* which uses luminescent bacteria to hide its shadow during hunting, Nyholm et al (2000). More common case is bacteria in the gastrointestinal tract of humans and animals which facilitate the digestion process. Some bacterial species like *Bacillus subtilis* can protect plant roots from infections, Bais et al (2004). Thus bacteria is necessary for life however it also can represent a great danger for complex organisms. A lot of diseases and infections such as dental plaque, cystic fibrosis, and tuberculosis are spread by different bacterial species.

What allows so simple microorganisms as bacteria to spread along the world and survive everywhere including volcanic geysers of Yellowstone National Park, subglacial antarctic lakes, and thermal sources on the bottom of the ocean. The reason is that they are organized in complex communities known as biofilms, where bacterial cells cooperate by separating their functions and produce extracellular polymeric substances (EPS) covering the colony. Biofilms are extremely undesireabe in medical area because bacteria in these structures are 1000 times more tolerate to antibiotics than solitary

planktonic cells, Bjarnsholt et al (2013). According to the National Institutes of Health (NIH, USA) biofilms are responsible for 65% of microbial and 80% of chronic infections, Jamal et al (2018). Bacteria can also colonize indwelling medical devices (like heart valves) and cause hospital-acquired infections increasing thereby healthcare costs. In 2007 Center of Disease Control and Prevention (US CDC) reported about 1.7 millions cases of hospital-acquired infections with additional costs by $ 11 billions, Römling et al (2014). Still there are no efficient therapy or drug which can completely eliminate biofilms, Bjarnsholt et al (2013). However not all activity of biofilms is harmful. Microbial consortia organized in biofilms can be efficiently used for synthetic biology applied e.g. to drug and fuel generation, Brenner et al. (2008). In this case extracellular matrix provides a good media for communication between different types of cells allowing them to perform different tasks. Biofilms can be also used in plant protection, Hobley et al. (2015), as a biocatalysts for fermentation process in bioreactors, Gross et al (2009), e.g. for production of vinegar, Fukaya et al (1992), as biobarriers in oil industry, Böl et al (2012), and for development of self-healing materials, Dhami et al (2013).

Since bacterial biofilms have large influence to human life they are quite important subject to study. Apart of many biological and experimental researches, recently a plenty of mathematical model for biofilm development were proposed. The main challenge in simulation of bacterial colonies consists in that these structures are very complex and there are a lot of chemical, biological, and mechanical processes taking place in it. Many efforts are done in simultation of cellular behavior and biomass growth. For this end there are mathematical models based of diffusion and fluid dynamics equations, Eberl et al. (2001); Dockery and Klapper (2002), or based on cellular automata, Lapsidou and Rittman (2004). However mechanical response of biofilms is usually neglected or simplified. It happens because EPS is a complex media which can behave as a solid and as a fluid and which have heterogeneous properties evolving in time, Wilking et al. (2011).

In our work we will focus on mechanical aspects of biofilm growth. Following Espeso et al. (2015); Zhang et al. (2016); Iakunin and Bonilla (2018) we will consider macroscopic development of biofilm growing on air-agar interface. An example is the bacterium *Bacillus subtilis*, which is widely used in experiments, Wilking et al. (2011, 2013); Asally et al. (2012); Seminara et al. (2012). This specie is famous by its ability to organize complex wrinkling patterns during growth on agar layer in a Petri dish. The wrinkles contain much information about the biofilm:

- The wrinkling network is a biofilm "fingerprint" because the geometry of the patterns depends on bacterial growth whereas their frequency

and amplitude depend on properties of EPS and agar layer, Espeso et al. (2015).

- The colony uses wrinkles as a transport network. Thus understanding their emergence helps understanding how the colony infrastructure develops, Wilking et al. (2013).

- Wrinkles are related to defensive mechanisms that bacteria use to survive. In particular, Asally et al. (2012) have shown this for the cannibalism phenomena that takes place in *Bacillus subtilis* colonies, López et al. (2009).

Thus observed wrinkling patterns in bacterial biofilms depend on history and infrastructure of the colony and on properties of the EPS. Part of results presented in this thesis was already published in Iakunin and Bonilla (2018).

The thesis has the following structure. Firstly, in the chapter 1 we consider biofilms and especially extracellular matrix in more details, describe their emergence and development. In this chapter we also present most popular mathematical model for bacterial growth and for mechanics of biofilm highlighting the approaches of Trejo et al. (2013); Espeso et al. (2015), and Zhang et al. (2016) which we use as a basis for our model. In these approaches the biofilm is considered as a thin elastic film bonded to a viscoelastic stubstratum therefore in chapter 2 we provide a short background about plate bending theory and especially about wrinkling phenomena. Wrinkles emerge not only in *Bacillus subtilis* biofilms but also in crumpling paper Ben Amar and Pomeau (1997), bilayer structures used particularly in fabrication of micro- and nano-scaled devices Huang (2005), and in another biological tissues such as plant leafs Dervaux et al. (2009), human skin Kücken and Newell (2005), and brain cortex Budday et al (2014). The main challenge in mathematical simulation of wrinkles consists in that this problem stays on the interface between mechanics and geometry and therefore should be considered from different points of view.

After review of previous works and progress in research of biofilm we formulate our mathematical model in chapter 3 following Dervaux et al. (2009); Espeso et al. (2015); Iakunin and Bonilla (2018). This model is based on Föppl-von Kármán equations (FvKEs) widely used for simulation of thin plate bending which we modify including internal growth and interaction with agar substratum below the biofilm. Obtained equations are quite complex and it is not possible to solve them analytically in general case. However, we can perform an asymptotic analysis in a simple case of radial symmetry. The chapter 4 is devoted to this purpose. To find approximation of FvKEs solution we use connection between geometry of surfaces and bending of thin

plate described in Ben Amar and Pomeau (1997); Cerda and Mahadevan (2003). The final shape in this case is given by a pure geometrical infinitely thin surface obtained due to growth and refined by taking into account that the biofilm has finite thickness. Existence of solution in general case is studied in chapter 5. There we use weak formulation to reduce number of unknown functions. We apply ideas of Lions (1969); Ciarlet and Gratie (2004) and consider operator form of the equations to prove existence of solution of modified FvKEs in a simple case.

In chapter 6, we develop a numerical method to solve equations derived before, which cannot be solved analytically. The numerical method is finite element method based on weak form presented in chapter 5. Chapter 7 is devoted to verification of developed solver. Chapter 8 contains a bifurcation study of the emergence of wrinkles from flat solution in two interesting cases: (i) switch from linear to non-linear plate theory due to increment of growth and (ii) bifurcation due to increment of stiffness of agar substratum. The bifurcation study is necessarily numerical because we cannot resolve the linear stability problem for the flat solution. Finally in chapter 9 we present our conclusions. We also formulate some unresolved problems that may lead to further research.

Chapter 1

Biofilms

Biofilms are aggregations of bacteria on a surface embedded to a self-produced matrix, Costerton and Lewandowski (1995). Even though these structures are composed by microbes, biofilms can be quite large and easily seen with the naked eye. Curiously that bacteria theirselves were discovered by Antonie von Leeuwenhoek in the end of XVII during studying one of such biofilms, a dental plaque, Costerton et al (1999). Nevertheless until the XX century most of researches about bacteria dealt with pure culture of planktonic cells instead of biofilms. Obtained results finally composed a new scientific branch – microbiology where a lot of advances were done in the edge between XIX and XX centuries, particularly thanks to works of Robert Koch and Louis Pasteur. To that time scientists had understood a lot about bacterial metabolic and genetic activity, Costerton et al. (1987), and nature of infection diseases such as cholera or tuberculosis, Høiby et al (2015). However almost all bacteria on Earth live in biofilms, Bjarnsholt et al (2013), and their behavior dramatically differs from the one of planktonic cells. Bacterial colonies were studied for the first time in the beginning of XX century in relation to submerged parts of ships and other constructions. Later in the second half of XX century these structures we considered in relation to lung infection. Finally in 80th the term "biofilm" was established by Costerton et al. (1987) for all types of bacterial colonies. For last few decades studying of biofilms is one of the most important directions in microbiology.

In this chapter we provide the most common knowledge about formation and development of biofilms. We also describe different mathematical models used for simulation of these aggregates.

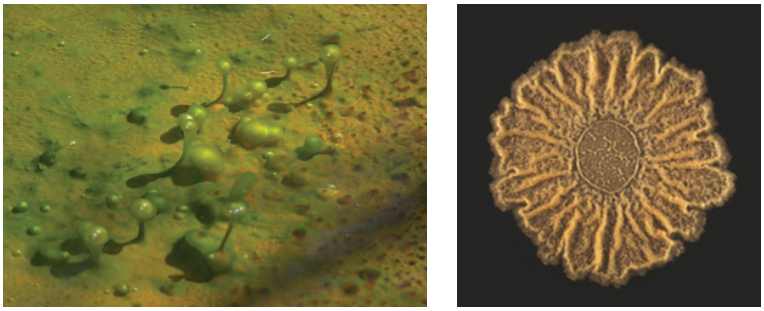

(a) (b)

Figure 1.1: Photos of bacterial biofilms: (a) mushroom-like colonies in a stream in Yellowstone National Park, picture from Klapper and Dockery (2010); (b) *Bacillus subtilis* biofilm in a Petry's dish, photo from Chai et al (2011).

1.1 Extracellular matrix

Prokaryotes such as archaea and bacteria represent the majority of the genetic variety of species hence the genetic difference between two distinct types of bacteria can be bigger than between humans and mushrooms. As a consequence biofilms can take a lot of different shape depending on bacteria specie, conditions of growth, surfaces the colony is attached to, and supply of nutrients. A couple of biofilm photos are presented in Figure 1.1. However life cycle of biofilms mostly follows general idea depicted in Figure 1.2. The formation starts when a few planktonic bacterial cells moving in a bulk fluid adhere to a surface. After attachment bacteria start to consume nutrients from substrates dissolved in bulk fluid or from agar substratum below. Besides, bacteria's phenotype changes allowing them to utilize resources to produce extracellular matrix (ECM). The choice of the source of nutrients influences to their distribution and transport in the colony and consequently to the shape of biofilm which can be flat, Flemming and Wingender (2010), mushroom or finger like structures, Bjarnsholt et al (2013), or wrinkles and channels, Trejo et al. (2013); Seminara et al. (2012). When the biofilm is large enough spore cells release and colonize other surfaces (Figure 1.2). Bacterial colonies usually contain many different species of bacteria. However even if the biofilm is organized by only one specie, bacterial cells may have different phenotypes, separate their functions, and cooperate. Therefore in some sense bacterial biofilms may be considered as a first predecessor of multicellular organisms.

What makes biofilms so different from solitary cells? The answer is ex-

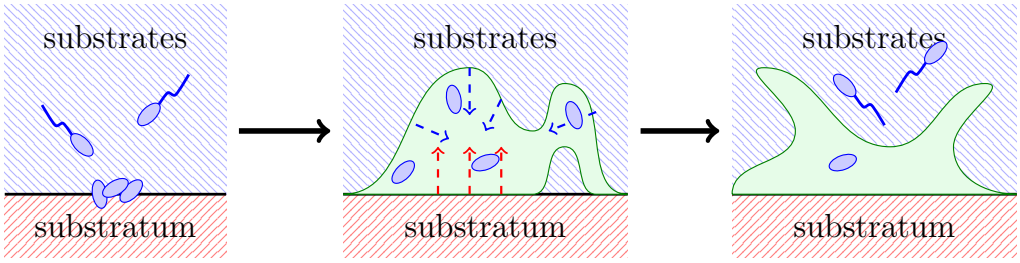

Figure 1.2: Schematic picture of the biofilm formation on surface-fluid interface. Firstly planktonic cells attach to agar substratum. Next bacteria start to divide and produce ECM consuming nutrients from substrates in bulk fluid and agar below. Finally spores are relized from mature biofilm to colonize new surfaces.

tracellular matrix (ECM) – a mixture of proteins, exopolymeric substances (EPS), extracellular DNA, and water, which covers all the colony and sticks cells together. The matrix may represent up to 90 % of total mass of biofilm, Flemming and Wingender (2010), and is crucial for many cellular activity taking place in the colony. Firstly the ECM holds large amount of bacteria together facilitating and enhancing cell-to-cell communications and horizontal gen transfer, Hall and Mah (2017). Besides ECM maintains enzymes close to bacteria and plays role of external digestive system, Flemming and Wingender (2010). Production of ECM also provides osmotic pressure which pushes bacterial cells and enhances spreading of the colony, Seminara et al. (2012).

Secondly ECM prevents penetration of antibiotics inside the colony and protects bacterial cells. Particularly, experiments show that wild type of *Pseudomonas aeruginosa* biofilms is more tolerant to antibiotics than mutant which lacks EPS production, Hentzer et al (2001). However the matrix slows diffusion of nutrients and oxygen together with diffusion of toxic substances therefore bacteria in the center of biofilm lack resource and have to modulate their metabolic activity. On the one hand this phenomena may seem a disadvantage of biofilm mode of bacterial life however changes in metabolism makes bacteria more tolerate to antibiotics, Martínez and Rojo (2011). Furthermore, in some bacterial species cells in the center of biofilm pass to anaerobic way of life hence they should be proceed with a different antibiotics than aerobic bacteria.

Finally production of ECM turns biofilm into a complex 3D structure with channels, wrinkles, or pores. The shape of bacterial colony is quite important because it defines the infrastructure and as consequence the way how

resources will be distributed along the colony. For example, some biofilms have mushroom like shapes with large surface hence they can absorb more nutrients from the substrate. Another bacterial species organize rugose biofilms with a network of channels used for transport of nutrients to the center of the colony, Wilking et al. (2013). Thus the stability of 3D shapes of biofilms is crucial for survive-ability of the colony therefore the explanation of the morphogenesis of biofilms is a subject of great interest. Shape of biofilm depends on mechanical properties of ECM which still are not well determined. Troubles in experimental measurement consist in high heterogeneity of biofilms, alteration of their properties in time, and high variation of ECM components for different species and even for the same one under different growth conditions. Young modulus of ECM is not very large and may vary from a few 100 Pa (for *Pseudomonas aeruginosa*, Böl et al (2012)) to 25 kPa (for *Bacillus subtilis*, Asally et al. (2012)) that represents another trouble due to the necessity to use of sensitive equipment.

Experimental researches provide a lot of data about development of biofilms, their response to different external factors, chemical reactions and processes inside the colony. Nevertheless in order to understand formation of biofilms and extract the main factors responsible for their growth and shaping we have to use methods of mathematical simulation, Horn and Lackner (2014). Due to the great variety of patterns in bioflms, properties of ECM, and nature of processes taking place inside the colony there are a lot of approaches to model these structures. Mathematical model can consider bacterial colonies as solids, fluids, or systems of rigid cells. They can also focus on different time scales simulating fast mechanical processes or slow cellular behavior. In the next section we provide a review of most common mathematical model describing development of biofilms.

1.2 Mathematical models for bacterial biofilms

We can divide most of mathematical models used for simulation of biofilms into a few groups. One classification can be done due to modeling goals: models used for slow processes related to growth of bacterial biomass and models for fast mechanical processes. In the first group the domain occupied by biofilm usually changes in time that represents the main challenge. In the second group the domain is fixed but equations can have more complex shape. Recently a new class of hybrid models emerged. These models try to simulate all variety of biofilm behavior by coupling different approaches for different processes. However due to complexity of the hybrid models a lot of initial parameters have to be determined from experiment that sometimes is

not possible to do, Horn and Lackner (2014).

Inside each of considered groups following Mattei et al. (2017) we can do another division: models can be discrete or continuum. First ones represent biofilms as a set of agents, i.e. cellular automaton or individual-based model. These models can naturally catch the heterogeneity of bacterial colony, variety of cellular behavior, and can be relatively easy generalized to multidimensional case. However discrete approach is usually stochastic and are not very suitable for description of mechanical effects. In continuum models we deal with scalar, vector, or tensor fields which alter in time and space governed by differential equations. Thus the behavior of bacterial cells is not taken into account as individuals but only in averaged way. This approach provides deterministic solution and is useful for calculation of some general properties of biofilms e.g. thickness of colony or presence of wrinkles. It also allows to use well studied framework of differential equations for reaction-diffusion, hydrodynamic, and mechanic of solids. However mathematical models in continuum approach are quite complicated due to heterogeneity of biofilm properties, alteration of the domain occupied by bacteria, and large number of used equations.

In this section we give a review for most common approaches for simulation of biofilm. Firstly we will consider models related to simulation of biomass growth and spreading. These models are well studied from mathematical and numerical points of view and can be used in practice for example for estimation of bioreactor efficiency. However there is a lack of description of mechanical effects which have a huge impact to biofilm morphogenesis, their resistance to external forces, and detachment from the substratum. Simulation of mechanical behavior of biofilm is the issue the second subsection is devoted to. In that subsection we will consider simulation of mechanical response of biofilm to external flow and wrinkling in *Bacillus subtillis* colonies.

1.2.1 Simulation of biomass growth

First models for growth of biomass were proposed in 1980s almost in the same time when biofilms becomes the subject of interest of biologists. Wanner and Gujer (1986) considered multispecies biofilm formed by adhesion of planktonic cells suspended in a mixture of substrates. Even though their model is 1D it can be eficiently used to estimate eficiency of bioreactors, Mattei et al. (2017), since it predicts spatial distribution of bacteria, thickness of biofilm, and consumption of nutrients. Furthermore this model provides a good basis for many following models. The authors distinguish four main components of the biofilm growth: (i) bacterial growth due to utilization of

substrates; (ii) expansion of biomass; (iii) diffusion of substrates; (iv) attachment and detachment of planktonic cells. For n bacterial species in mixture of m substrates the equations proposed in Wanner and Gujer (1986) have the following shape:

$$\frac{\partial f_i(t,z)}{\partial t} + u(t,z)\frac{\partial f_i(t,z)}{\partial z} = (\mu_i(t,z) - \bar{\mu}(t,z))\, f_i(t,z),\ i = 1,\dots,n; \quad (1.1)$$

$$\frac{\partial S_j(t,z)}{\partial t} = r_j(t,z) + \frac{\partial}{\partial z}\left(D_j \frac{\partial S_j}{\partial z}\right),\ j = 1,\dots,m; \quad (1.2)$$

$$\frac{dL(t)}{dt} = u(t,L) + \sigma_a(t) - \sigma_d(t), \quad u(t,z) = \int_0^z \bar{\mu}(t,z')dz'; \quad (1.3)$$

where f_i is volume fraction of i-th bacteria ($\sum_{i=1}^n f_i = 1$), S_j is concentration of j-th substrate, L is the thickness of biofilm, μ_i and $\bar{\mu}(t,z) = \sum_{i=0}^n \mu_i(t,z) f_i(t,z)$ are observed growth rate of i-th bacteria and of all biomass respectively, u is velocity of biomass expansion, and σ_a and σ_d are attachment and detachment rates. The domain occupied by the biofilm is given by an interval $z \in (0; L(t))$ where $z = 0$ corresponds to a wall of container whereas $z = L(t)$ is biofilm-fluid interface. The system (1.1)-(1.3) should be equipped by $n + m + 1$ initial conditions for each unknown and $n + 2m$ boundary conditions: n at $z = 0$ for volume fractions f_i and $2m$ for substrate concentrations S_j at both sides of the domain.

Proposed equations are coupled through growth and utilization rates $\mu_i(t,z)$ and $r_j(t,z)$ which are nonlinear functions of unknown volume fractions and substrate concentrations (e.g. growth rates can be given by Monod law). Additional challenge consists in conditions at $z = L(t)$ since this boundary moves. This trouble appears in most of problem related to simulation of biomass growth.

Apart of distribution of bacterial cells and biomass the final shape of biofilm is also a subjet of a interest. The model of Wanner and Gujer (1986) is 1D and hence cannot be used for this end. However it can be generalized for multidimensional cases. One of generalizations was proposed by Eberl et al. (2001). This model consider biofilm of only one specie which utilizes nutrients from only one substrate. Let us call the initial domain Ω and its part occupied by fluid and biofilm we call Ω_1 and Ω_2 respectively ($\Omega_1 \cup \Omega_2 = \Omega,\ \Omega_1 \cap \Omega_2 = \emptyset$).

Then the equations proposed in Eberl et al. (2001) are:

$$\begin{aligned} \nabla \cdot \mathbf{u} = 0, \quad \frac{\partial \mathbf{u}}{\partial t} + \mathbf{u} \cdot \nabla \mathbf{u} = -\frac{1}{\rho} \nabla p + \nu \Delta \mathbf{u}, \quad & \mathbf{x} \in \Omega_1 \\ \mathbf{u} = \mathbf{0}, \quad & \mathbf{x} \in \Omega_2 \end{aligned} \tag{1.4}$$

$$\frac{\partial c}{\partial t} + \mathbf{u} \cdot \nabla c = \nabla \cdot (d_1(m) \nabla c) - f(c, m), \tag{1.5}$$

$$\frac{\partial m}{\partial t} = \nabla \cdot (d_2(m) \nabla m) + g(c, m). \tag{1.6}$$

Here $\mathbf{u}$ is velocity of the flow, p is pressure, ν is viscosity, c is concentration of the substrate, and m is biomass density: $m(t, \mathbf{x}) = 0$ if $\mathbf{x} \in \Omega_1$ and $m(t, \mathbf{x}) > 0$ if $\mathbf{x} \in \Omega_2$. Functions $f(c, m)$ and $g(c, m)$ defining substrate utilization and biomass growth respectively are given by Monod law as follows:

$$f(c, m) = \frac{k_1 c m}{k_2 + c}, \quad g(c, m) = k_3 (f(c, m) - k_4 m), \tag{1.7}$$

where k_i, $i = 1, \ldots, 4$, are nonegative constants. Diffusion coefficient $d_1(m)$ and $d_2(m)$ depend on quantity of biomass for a number of reasons. Firstly, diffusion of substrate inside the biofilm differs from diffusion in the flow therefore $d_1(m)$ may even have discontinuity on the interface between Ω_1 and Ω_2. Secondly it is known that biomass spreading is significant only in zones with high density and besides the density cannot exceed a threshold m_{max}. These condition can be satisfied by the following diffusion coefficient:

$$d_2(m) = \left(\frac{\epsilon}{m_{max} - m} \right)^a m^b. \tag{1.8}$$

Easy to see that if $m = 0$ there is no diffusion that is biofilm spreads only from zones occupied by bacteria. Note that the diffusion coefficient $d_2(m)$ has two types of singularity: when biomass vanishes and when it achieves the threshold m_{max}, Sonner et al. (2015). This effect is one of important peculiarities in simulation of biomass growth in biofilms.

The system (1.4) – (1.6) is hard to solve in general case but in Eberl et al. (2001) an analyses of simplest cases was done. For example on the one hand in absence of biomass ($m = 0$) the system turns into usual convection-diffusion equation with flow $\mathbf{u}$ satisfied Navier-Stokes equations. On the other hand, if the flow is stationary we have predator-prey model for biomass and substrate. Numerical solution in 3D predicts mushroom-like patterns for large growth which are merging in a solid film when the growth decreases. One of disadvantage of the Eberl et al. (2001) model is that it does not take into account death of cells. The generalization was done in Eberl et al.

(2010) where the biofilm is considered as multispecies culture (one of specie represents dead cells) which develops in a mixture of different substrates.

In papers of Eberl et al. (2001, 2010) the biomass spreads due to diffusion but there is another approach proposed by Dockery and Klapper (2002). In this paper Darcy's law is used to describe biomass spreading. According to this model the biofilm is supposed to be incompressible viscous fluid which is pushed by internal pressure:

$$\mathbf{u}_b = -\lambda \nabla p, \quad \nabla \cdot \mathbf{u}_b = g, \quad -\lambda \Delta p = g, \tag{1.9}$$

where $\mathbf{u}_b$ is velocity of biomass, λ is positive constant, p is pressure, and g is growth function, which can be obtained from equation (1.7). Coupling (1.9) with (1.5) gives us another model for biomass spreading in a steady flow. Using this model Dockery and Klapper (2002) studied instability of bacterial colony which leads to formation of finger-like structure. There also is variation of this approach proposed by Cogan and Keener (2004). They take into account that ECM is sum of different polymers and use Flory-Huggins theory of gel-like materials to simulate it. Polymers are composed from quite large chain molecules therefore their elastic response can be estimated using averaging of molecular behavior. The pressure in this case can be calculate as follows:

$$p = -\frac{k_b T}{v_1} \left(\log(1-\theta) + \theta + \chi_1 \theta^2 \right), \tag{1.10}$$

where θ is volume fraction of polymeric chains in ECM, v_1 is their volume, k_b is Boltzmann's constant, T is temperature, χ_1 is the Flory interaction parameter.

All models considered above are continuum so solving them we face the problem of a spreading interface between the biofilm and the fluid. Discrete approach can be useful to get rid of this trouble. In paper Piciorenau et al (1998) a hybrid model of cellular automaton (CA) with reaction-diffusion equation is presented. The idea of CA consists in a discretization of the domain into small blocks and approximation of physical, chemical, or biological law by a system of simple rules. In the model of Piciorenau et al (1998) CA is used to simulate spreading of biomass. The idea for one substrate and one species of bacteria is the following. We create a grid which represents the CA discretization and in each cell we define three values: $S_{x,y,z}$ is substrate concentration, $C_{x,y,z}$ is biomass concentration, and $c_{x,y,z}$ is occupation state (1 if cell is occupied by biofilm and 0 otherwise). Substrate and biomass

concentration are given by PDEs:

$$\frac{\partial S}{\partial t} = D_S \Delta S - \rho_S(C, S),$$
$$\frac{\partial C}{\partial t} = \rho_C(C, S),$$

which we discretize and solve using the defined grid. The occupation state we update using simple rules of CA:

1. If biomass concentration $C_{x,y,z}$ achieves its maximum value C_{max} we have to put half of biomass in a neighboring cell;

2. From all free ($c_{x,y,z} = 0$) neighbors we randomly pick one and put the excess of biomass there;

3. If there are no free cell around we randomly pick one and displace with the new piece of biomass;

4. The displaced cell repeats this algorithm.

Later the model of Piciorenau et al (1998) was generalized in Lapsidou and Rittman (2004) and called unified multi-component cellular automaton model (UCCMA). In this approach one considers not only concentration of biomass and substrate but also concentrations of oxygen, active and dead cells. The model proposed by Lapsidou and Rittman (2004) can efficiently catch the heterogeneity of bacterial colonies.

1.2.2 Simulation of mechanical effects

In previous section the biofilms were considered as viscous fluids but these structure also have elastic properties. Elasticity of biofilms not only influences on their response to surrounding fluid and detachment of biomass, but also to general shape of the colony even in the absence of external forces. For example *Bacillus subtilis* colonies growing on agar substratum can buckle into complex wrinkling patterns, Trejo et al. (2013). This effect is similar to the buckling happened in industrial application and is due to mechanical instability. Nevertheless mechanical deformation of biofilms is more complex than deformation of industrial constructions: the properties of biofilm are heterogeneous, they alter in time, and there are a huge variety of different shapes and applied forces. Even though there is a consensus that biofilms are viscoelastic the measurement of their viscosity and elastic modulus is quite challenging, Guelon et al. (2011). Furthermore, stiffness of biofilm may vary

for young and mature colonies as well as for colonies embedded in fluid and ones growing on air-agar interface.

Global mechanical response of biofilm undergoing impact of surrounding fluid is studied in papers Hammond et al. (2014) and Stotsky et al. (2016). The authors use immersed boundary method which is a variation of idividual-based method where biofilm is considered as a framework of bacterial cells connected by elastic springs and embedded in a viscous fluid. The viscosity of fluid varies a lot because far from cells it is bulk-luiqud whereas close to them it is ECM.

Immersed boundary method allows to catch viscous and elastic behavior of biofilm at the same time. To apply this method in the paper Hammond et al. (2014) Eulerian $\mathbf{x}$ and Lagrangian $\mathbf{q}$ coordinate systems were introduced. The first system is used to calculate flow using Navier-Stokes equations and in the second coordinate system we define nodes where bacterial cells are located. Thus the Eulerian velocity of fluid $\mathbf{u}(t,\mathbf{x})$ is given by Navier-Stokes equations:

$$\rho(t,\mathbf{x})\left(\frac{\partial \mathbf{u}}{\partial t}+\mathbf{u}\cdot\nabla\mathbf{u}\right) = -\nabla p+\nabla\cdot\big(\mu(t,\mathbf{x})\big(\nabla\mathbf{u}+(\nabla\mathbf{u})^T\big)\big)+\mathbf{f}(t,\mathbf{x}), \quad (1.11)$$

$$\nabla\cdot\mathbf{u} = 0, \quad (1.12)$$

where $\rho(t,\mathbf{x})$ and $\mu(t,\mathbf{x})$ are density and viscosity respectively, and external force $\mathbf{f}(t,\mathbf{x})$ is given from bacterial cells located in nodes $\mathbf{X}(t,\mathbf{q})$:

$$\frac{\partial \mathbf{X}}{\partial t} = \int_\Omega \mathbf{u}(t,\mathbf{x})\delta(\mathbf{x}-\mathbf{X}(t,\mathbf{q}))d\mathbf{x}, \quad (1.13)$$

$$\mathbf{f}(t,\mathbf{x}) = \int_{\Omega_b} \mathbf{F}(t,\mathbf{q})\delta(\mathbf{x}-\mathbf{X}(t,\mathbf{q}))d\mathbf{q}, \quad (1.14)$$

$$\rho(t,\mathbf{x}) = \rho_0+\int_{\Omega_b}\rho_b\delta(\mathbf{x}-\mathbf{X}(t,\mathbf{q}))d\mathbf{q}. \quad (1.15)$$

Here Ω is flow domain, $\Omega_b\subset\Omega$ is domain occupied by biofilm, $\mathbf{F}(t,\mathbf{q})$ is force density in Lagrangian coordinates, ρ_0 is density of fluid, ρ_b is addition density of ECM from that of the surrounding fluid, δ is Dirac delta-function. Equation (1.11) – (1.15) almost complete the model, we only have to add elastic connections between bacterial cells and variation of viscosity. Assume we have n cells, then forces can be found as follows:

$$\mathbf{F}(t,\mathbf{X}_s)=\sum_{k=1}^{n} I_{s,k}\frac{\mathbf{X}_k-\mathbf{X}_s}{|\mathbf{X}_k-\mathbf{X}_s|}F_{max}\frac{|\mathbf{X}_k-\mathbf{X}_s|-r_{s,k}}{r_{s,k}}, \quad (1.16)$$

where $I_{s,k}=1$ if cells s and k are connected and 0 otherwise, $r_{s,k}$ is rest length of spring connecting cells i and k, and F_{max} is the force requite to

break the spring. We assume that the maximum viscosity μ_{max} is achieved in the position of cells and the minimal viscosity μ_{out} corresponds to external fluid. Then we can calculate viscosity in each point as

$$\mu(\mathbf{x}) = \max_{s\in 1,\dots,n} \left((2\omega)^D (\mu_{max} - \mu_{out}) \tilde{\delta}(\mathbf{x} - \mathbf{X}_s, \omega) + \mu_{out} \right), \tag{1.17}$$

where ω is radius of cell, D is dimension, and $\tilde{\delta}(\mathbf{x}, \omega)$ is approximation of Dirac-delta function with a support of radius ω.

Coupling the system (1.11) – (1.17) with corresponding boundary conditions we obtain the description of mechanical deformation of biofilms in terms of immersed boundary model. Using this model Hammond et al. (2014) calculated detachment force in mushroom-shape biofilms which coincides with experimental value. Later in Stotsky et al. (2016) this model was modified to estimate another material properties of biofilms.

A different approach to simulate mechanical response of biofilm in fluid is proposed in paper Lapsidou et al. (2014). In this paper the authors use UMCCA method coupled with finite element simulation of elastic deformation of biomass which is considered as a four-composite material. Four different components are represented by solid biomass, extrapolymeric substance, inert biomass, and void space with zero stiffness. Numerical simulation in 2D using ABAQUS software showed that for relatively small deformation average behavior of biofilm can be described using linear elasticity. However when the deformation is large the mechanical response is nonlinear because biofilm is a porous structure.

In models considered above the geometry of biofilm is already given however in reality even morphogenesis of the colony is governed by mechanical properties as it happens for *Bacillus subtilis*. First attempt to describe wrinkling of *Bacillus subtilis* biofilms using mechanics of thin plates was done by Trejo et al. (2013). The authors use Föppl-von Kármán equations describing large bending of elastic plates which they reduce to 1D case and study simple buckling. The deformation is caused by internal growth and frequency of wrinkles increases due to interaction with agar substratum:

$$\frac{Eh^3}{12(1-\nu^2)} \frac{d^4\zeta}{dx^4} - h\sigma \frac{d^2\zeta}{dx^2} = K\zeta \tag{1.18}$$

$$h\frac{d\sigma}{dx} = 0, \tag{1.19}$$

$$\sigma = \frac{E}{1-\nu^2} \left(\frac{du}{dx} + \frac{1}{2} \left(\frac{d\zeta}{dx} \right)^2 - (1+\nu)g \right), \tag{1.20}$$

where E, ν and h are Young modulus, Poisson ratio and thickness of biofilm,

$K = \rho g$ stiffness of substratum (in this case deformation energy of the substratum is just gravitational potential of liquid), g internal growth of biofilm, σ and ζ stress and vertical deflection of the film. Even though this model is 1D in can be used to estimate frequency and amplitude of wrinkles.

In paper Espeso et al. (2015) a hybrid model was proposed. This model includes cell-to-cell communication modeled by cellular automaton, diffusion and consumption of nutrients modeled by reaction-diffusion equations, and mechanical deformation part modeled by Föppl-von Kármán equations coupled with viscoelastic substratum:

$$\frac{\partial \zeta}{\partial t} = \frac{1-2\nu}{2(1-\nu)} \frac{H}{\eta} \left[\frac{Eh^3}{9} \left(-\Delta^2 \zeta + \Delta C_M \right) + h \nabla \cdot (\boldsymbol{\sigma} \cdot \nabla \zeta) \right] - \frac{\mu}{\eta} \zeta, \quad (1.21)$$

$$\frac{\partial \mathbf{u}}{\partial t} = \frac{Hh}{\eta} \nabla \cdot \boldsymbol{\sigma} - \frac{\mu}{\eta} \mathbf{u}, \quad (1.22)$$

where ζ is vertical deflection of central surface, $\mathbf{u}$ its horizontal displacements, h and H are thickness of biofilm and substratum respectively, E is Young modulus of the biofilm, μ, η, and ν are rubbery modules, viscosity, and Poison ration of the substratum, $\boldsymbol{\sigma}$ is stretching stress of the colony, and C_M is Gaussian curvature provided by growth.

In the model of Espeso et al. (2015) internal growth was obtain by averaging of cellular behavior obtained from another part of hybrid model, and as a result was very heterogeneous. Nevertheless Föppl-von Kármán equations of film bending on a substratum allow solution with wrinkling patterns even for quite simple growth. It was shown in paper Zhang et al. (2016) where a similar model based on equations (1.21) – (1.22) is considered. The difference is that in Zhang et al. (2016) the growth is given by arbitrary function (it can be radial growth, radial shrinkage, or heterogeneous growth) and a more complex model for agar-biofilm interaction supposing delamination is used. The authors show that by changing of biofilm stiffness and type of growth it is possible to obtain numerically almost all wrinkling patterns seen in the experiment.

In our work we consider wrinkling of *Bacillus subtilis* biofilm growing on agar substratum. We will follow ideas of Espeso et al. (2015) and consider bacterial colony as a thin hyperelastic film bonded to a viscoelastic layer. We imporve the model (1.21) – (1.22) by including heterogeneity of ECM material. We assume that there is no delamination since experiments show that this effect takes place only for mature biofilms. Following Zhang et al. (2016) we consider wrinkling under effect of a few different types of growth given by arbitrary functions and provide a rigorous mathematical analysis of this phenomena using asymptotic approach for simple case of radial growth and

weak formulation for general case. Finally we develop a numerical method based on finite elements which can be applicable to simulation of *Bacillus subtilis* growth in different configuration of growth, stiffness, and occupied domain.

Chapter 2

Wrinkling phenomena in thin films

Wrinkling patterns occur not only in biofilms but also in many problems related to deformation of thin plates or shells: from crumpling of a napkin, Audoly and Pomeau (2010), to deflection of Earth's crust, Turcotte and Schubert (1982). Wrinkles are not the unique shape which thin plates can take, it can be almost any figure as it happens in origami. This peculiarity of thin films differs them from other structure and requires explanation from mechanical point of view and also from geometrical considerations, Audoly and Pomeau (2010).

We can demonstrate why do we have to keep in mind both mechanical and geometrical effects on a quite habitual but not very simple example of crumpling of paper studied in Ben Amar and Pomeau (1997). M. Ben Amar and Y. Pomeau considered a sheet of paper which bends because of displacements applied on its boundary. We know that during crumpling a sheet of paper turns into a polygonal shape that is the sheet is flat on all faces but bends on ridges. This shape is a result of geometrical transformation, more precisely, of Gauss's *"theorema egregium"*. This theorem says that if we continuously transform a surface without stretching then it will maintain its curvature. Particularly if a sheet of paper was flat it will be flat almost everywhere. In reality this theorem is satisfied only in approximate way. For example if we double a sheet of paper then both sides can be considered as flat surfaces however in the fold itself we will see a smoothed zone. Furthermore, the scar left by the fold will be seen even when we unwrap the sheet, and if we double it at the same line more times then finally it will break there. It happens because in difference with geometrical surface, the paper sheet has finite thickness hence in zones where bend is very sharp (first derivative of deflection has a jump) the material undergoes large stresses and can collapse.

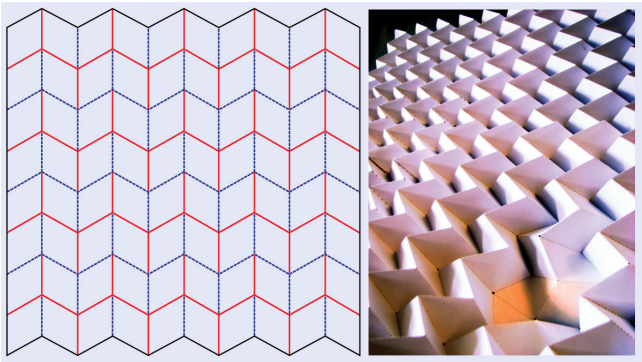

Figure 2.1: Miura tessellation.
Source: http://live.iop-pp01.agh.sleek.net/2015/11/18/flat-pack-physics/

The concentration of deformation energy in very small zones such as ridges and vertices instead of its uniform spreading is according to Witten (2007) the most fascinating effect in wrinkling of thin films. Despite that this behavior seems quite counterintuitive it allows thin films to convert in-plane deformation to vertical deflection and thereby to turn stretching energy into the bending one which tends to be much smaller. Interesting example of how folding can change properties of the material is Miura tessellation (Figure 2.1). This figure is not only a toy, it can be used in metamaterials and in solar plants of satellites. Miura tessellation allows to initially inextensible paper sheet to stretch or compress. Furthermore it provides a negative Poisson ratio that is compression in one direction leads to compression in the orthogonal one. Note that the paper almost does not undergo any stretching stresses. The condition of absence of such kind of stresses is used in various works in order to calculate the deformed shapes of thin films and estimate frequency and amplitude of wrinkles.

2.1 Wrinkles as a result of cancellation of stretching strains

In paper Cerda and Mahadevan (2003) a folding of a polyethylene sheet is studied. The polyethylene is stretched in one direction and wrinkles in its center as it happends with plastic bags (Figure 2.2). Due to Poisson effect enlargement of the sheet along x leads to its squeezing along y. Wrinkles emerge when compressing strain in y-direction achieves a critical value ε_c. At this moment the sheet buckles canceling in-plane stresses and changing

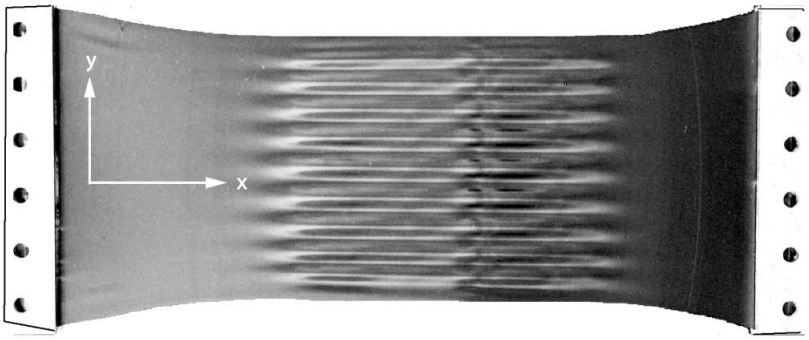

Figure 2.2: Experiment with stretching of polyethylene sheet presented in Cerda and Mahadevan (2003)

them to bending ones similarly to Miura tessellation. In other words the deformation energy accumulated in compressed sheet is balanced by bending energy of the simplest wrinkling pattern.

Let the polyethylene sheet from Figure 2.2 has length L in x direction and width W in y direction. In order to find frequency and amplitude of wrinkles Cerda and Mahadevan (2003) use a quite simple model based of minimization of augmented energy functional subject to absence of y-direction strains. The augmented energy functional contains 3 terms: bending energy $\mathcal{W}_{bend}$, stretching energy $\mathcal{W}_{stretch}$, and constrain $\mathcal{L}$. In this simple case Cerda and Mahadevan (2003) take into account that all bending happens in y direction and all stretching happens in x direction thus first two terms of the functional have the following shape

$$\mathcal{W}_{bend}=\int_{\Omega}\frac{Eh^3}{12(1-\nu^2)}\left(\frac{\partial^2\zeta}{\partial y^2}\right)^2 dxdy,\quad \mathcal{W}_{stretch}=\int_{\Omega}T(x)\left(\frac{\partial\zeta}{\partial x}\right)^2 dxdy, \quad (2.1)$$

where E, h, ν are Young modulus, thickness, and Poisson ratio, $\zeta(x,y)$ is vertical displacement, $T(x)$ is stretching stress, and Ω is the domain occupied by the sheet. The absence of stretching strains in y-direction means that for any x the width of the sheet maintain the same:

$$\int_0^{W-\Delta(x)}\sqrt{1+\left(\frac{\partial\zeta}{\partial y}\right)^2}dy=W\Rightarrow\int_0^{W-\Delta(x)}\left(1+\frac{1}{2}\left(\frac{\partial\zeta}{\partial y}\right)^2\right)dy\approx W, \quad (2.2)$$

where $\Delta(x)$ is imposed compressive displacement. In paper Cerda and Mahadevan (2003) equation (2.2) is used in simplified form under assumption that $\Delta(x)$ is small:

$$\int_0^{W}\left(\frac{1}{2}\left(\frac{\partial\zeta}{\partial y}\right)^2-\frac{\Delta(x)}{W}\right)dy=0. \quad (2.3)$$

Augmented energy function can be obtained directly from formulas (2.1) and (2.3):

$$\mathcal{W} = \mathcal{W}_{bend} + \mathcal{W}_{stretch} - \mathcal{L} = \int_\Omega \left(\frac{Eh^3}{12(1-\nu^2)} \left(\frac{\partial^2 \zeta}{\partial y^2} \right)^2 + T(x) \left(\frac{\partial \zeta}{\partial x} \right)^2 \right) dxdy - \int_\Omega b(x) \left(\frac{1}{2} \left(\frac{\partial \zeta}{\partial y} \right)^2 - \frac{\Delta(x)}{W} \right) dxdy, \quad (2.4)$$

where $b(x)$ is Lagrange multiplier. In the center region we can say that T and b are constant thus variation of the augmented energy functional leads to equation:

$$\frac{Eh^3}{12(1-\nu^2)} \frac{\partial^4 \zeta(x,y)}{\partial y^4} - T \frac{\partial^2 \zeta(x,y)}{\partial x^2} + b \frac{\partial \zeta^2}{\partial y^2} = 0, \quad (2.5)$$

with periodic boundary conditions respect to x. From equation (2.5) Cerda and Mahadevan (2003) assuming that stretching stress $T = Eh\varepsilon_c$ achieves critical value found wavelength $\lambda = (2\pi Lh)^{1/2} \left(3(1-\nu^2)\varepsilon_c\right)^{-1/4}$ and amplitude $A = (\nu Lh)^{1/2} \left(\frac{16\varepsilon_c}{3\pi^2(1-\nu)^2} \right)^{1/4}$ of corresponding wrinkling patterns. Easy to see that if Poisson ratio ν goes to 0 that the amplitude will also go to 0. It represents the fact that wrinkles appear due to Poisson effect which produces compressing strains in y-direction.

The equation (2.5) with constrain (2.3) represent a simplified version of Föppl-von Kármán equations (FvKEs):

$$\frac{Eh^3}{12(1-\nu^2)} \Delta^2 \zeta - [\chi, \zeta] = p, \quad (2.6)$$

$$\frac{1}{Eh} \Delta^2 \chi + [\zeta, \zeta] = 0, \quad (2.7)$$

$$\frac{\partial^2 \chi}{\partial y^2} = h\sigma_{xx}, \quad \frac{\partial^2 \chi}{\partial x^2} = h\sigma_{yy}, \quad \frac{\partial^2 \chi}{\partial x \partial y} = -h\sigma_{xy}, \quad (2.8)$$

where p is the vertical forces, χ is Airy potential of stretching stress $\boldsymbol{\sigma}$, and $[\cdot, \cdot]$ is given by

$$[a, b] = \frac{\partial^2 a}{\partial x^2} \frac{\partial^2 b}{\partial y^2} + \frac{\partial^2 a}{\partial y^2} \frac{\partial^2 b}{\partial x^2} - 2 \frac{\partial^2 a}{\partial x \partial y} \frac{\partial^2 b}{\partial x \partial y}. \quad (2.9)$$

The mechanism of wrinkling due to cancellation of stretching strains is strongly related to geometry. In the case of absence of stretching stress that is $\chi = 0$ the second equation turns into Monge-Ampère equation (MAE) which gives

as a solution a surface with zero Gaussian curvature. These surfaces called developable surfaces. They play quite imporntant role in simulation of thin plate deformation since developable surfaces can be obtained from flat plate without any stretching. These surfaces are used by Ben Amar and Pomeau (1997) to study crumpling of paper and by Cerda et al. (1997) to study formation of conical shape due to inserting of a paper sheet in a cylindrical glass. The main problem consists in that the developable surfaces obtained as a solution of MAE may not correspond to any physical solution since there can be intersections and sharp bends where bending energy goes to infinity. This effect leads to emergence of specific core and ridge layers where we have to use another approaches to find the solution.

In biological systems a quite similar mechanism of wrinkling related to geometry works. The difference consists in that organic tissues deforms due to internal growth which provides a non-zero curvature hence the solution is not an approximation of developable surface. However we can find the surface provided by growth and smooth it in zones of sharp bend. This approach is used in Dervaux and Ben Amar (2008) in order to model morphogenesis of mushroom hat and in Dervaux et al. (2009) applied to wrinkling of plant leaves. In both these papers modified FvKEs are derived using Rodriguez et al. (1994)'s hypothesis of growth, that includes biological growth as a residual stress or strain:

$$\frac{Eh^3}{9}\Delta^2\zeta-[\chi,\zeta]=0, \tag{2.10}$$

$$\frac{1}{Eh}\Delta^2\chi+[\zeta,\zeta]=\Psi=\frac{\partial^2}{\partial x\partial y}\left(g_{12}+g_{21}\right)-\frac{\partial^2 g_{11}}{\partial y^2}-\frac{\partial^2 g_{22}}{\partial x^2}, \tag{2.11}$$

where g_{ij} are components of growth tensor. Right part of (2.3) is Gaussian curvature Ψ produced by growth tensor $\mathbf{g}$, that is if we assume that distances between any two points change according to a metric tensor $\mathbf{G}=\mathbf{I}+\mathbf{g}$ where $\mathbf{I}$ is identity tensor, then flat film turns into a surface with curvature Ψ. Similarly to the case of developable surface if there is no stretching stress (2.3) becomes MAE which solution gives a surfaces of defined curvature Ψ. However this surface still may contain intersections or discontinuities of first derivatives of ζ and hence may not be physically possible. Thus in order to find solution of system (2.2) - (2.3) from Monge-Ampère approximation we have to insert specific layers in zones of ridges. We will study this technique in more details in chapter 4 applied to a quite simple example.

2.2 Influence of a substratum to formation of wrinkles

Another mechanism of wrinkle emergence is interaction with a viscoelastic substratum. In paper Cerda et al. (1997) authors note that geometrical nonlinearity ties frequency and amplitude of wrinkles. High frequency patterns have large bending energy therefore a free film usually does not wrinkle in a complex network but just folds few times. However if the film is fixed somewhere or bonded to a substratum the picture changes dramatically. Indeed, for a film bonded to a viscoelastic layer large amplitude of wrinkles leads to large deformation of the substratum. As a result we have a competition between the bending energy of the film (which is minimal for high amplitude) and the energy of the layer (which, on the contrary, achieves its minimum for high frequency).

A quite simple case of a film-substratum interaction is considered in the paper Huang et al. (2010) where wrinkling of a polymeric sheet lies on a fluid layer is studied. Similarly to the simplest case of previous subsection we can write augmented energy function as a sum of three parts: bending energy, deformation energy of the substrate, and condition of absence of stretching stress:

$$\mathcal{W}=\int_0^L \left(\frac{Eh^3}{12(1-\nu^2)} \left(\frac{d^2\zeta}{dy^2}\right)^2 + \rho g \zeta^2 - b(x) \left(\frac{1}{2} \left(\frac{d\zeta}{dy}\right)^2 - \frac{\Delta(x)}{L} \right) \right) dx, \quad (2.12)$$

where ρ is density of the substrate and g is gravity acceleration. Note that in the previous subsection wrinkles emerge due to Poisson effect and we had to consider 2D problem whereas the substratum allows to get wrinkles even in 1D problem. Using variational principle Huang et al. (2010) obtain that wavenumber is proportional to $(\rho g/(Eh^3))^{1/4}$. This result represents the fact that the energy of the substratum (in this case gravitational) and film bending energy compete: the stiffer is the layer the higher is frequency of wrinkles and the smaller is the amplitude and on the contrary the stiffer is the film the smaller is frequency and the higher is the amplitude.

Bilayer structures similar to considered above are quite common in biology and also in many industrial applications. The substratum presence leads to more complex and interesting wrinkle patterns than ones we have seen in folding of an polyethylene sheet or in crumpling of paper. One of such new shapes is herringbones patterns studied by Chen and Hutchinson (2004) (Figure 2.3). These patterns are quite similar to Miura tessellation, Audoly and Boudaoud (2010), however presnece of elasomer substratum allows to obtain these shapes thereby thermal enlargement of a thin metal film in-

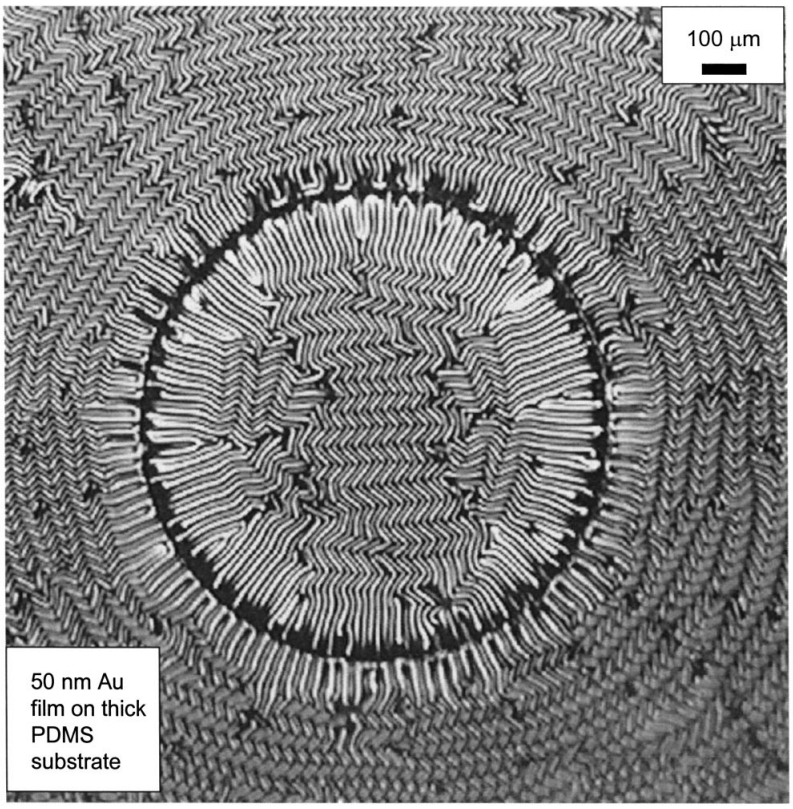

Figure 2.3: Example of a herringbone pattern from Chen and Hutchinson (2004)

stead of a complex folding algorithm used in origami. The ideas of Chen and Hutchinson (2004) were improved by Huang et al. (2005) who have found a more rigorous theory and developed a spectral numerical method to obtain this shapes on a computer.

For biological application wrinkling of film bonded to a substratum was used by Trejo et al. (2013); Zhang et al. (2016) to simulate biofilm development, by Budday et al (2014) to study wrinkling of mammalian brain cortex, and by Kücken and Newell (2005) to model formation of fingerprints. In some cases a more complex potential of the viscoelastic layer energy is used. For example in Kücken and Newell (2005) energy of the substratum is given by:

$$\mathcal{W}_{subsratum} = \int_{\Omega} V(\zeta) dxdy = \int_{\Omega} \left(p\zeta + \frac{\rho g}{2}\zeta^2 + \frac{a}{3}\zeta^3 + \frac{b}{4}\zeta^4 \right) dxdy, \quad (2.13)$$

where p is vertical force and ρg is "stiffness" of the substratum from Huang et al. (2010). Formula (2.13) allows to obtain more complex wrinkling patterns however more parameters should be determined from the experiment.

Another modification was done by Zhang et al. (2016) who added delamination effect to simulation of wrinkling of *Bacillus subtilis* biofilm. In this paper force with which the substratum affects on the film is proportional to ζ for small deflection and goes to zero exponentially when the deflection is large. To impose this exponential decay mathematically a Gaussian function $\exp(-\zeta^2)$ is used.

In our work we will follow ideas proposed by R. Huang and collaborators in a series of papers. They simulate the substratum as a linear viscoelastic material and tie all three components of displacements on the film-substratum interface. Then they solve equations for the layer that gives the necessary corrections for FvKEs. In the series of papers written by R. Huang and collaborators the first one Huang and Suo (2002b) uses lubrication theory however in later works Huang and Suo (2002a); Huang (2005) Kelvin model for viscoelastic material is applied. We will consider these models in more details in the chapter 3. We will also simplify the derivation done by R. Huang *et al* by using scaling method instead of quite complex analytical solution.

2.3 Wrinkles due to material heterogeneity

All previous analyses deal with homogeneous films. However, the properties of biofilms change along their surface. The heterogeneity of ECM stiffness, variation of internal growth and thickness can be an additional source of wrinkles. Let us consider the example of a growing heterogeneous material studied by Mora and Boudaoud (2006). These authors have considered growth of a disk comprising different gels at its central region and at its outer rim. In the core zone the gel is very stiff (Young modulus is 3.2×10^5 Pa) and almost does not grow, whereas the boundary region is much softer ($E = 5 \times 10^3$ Pa) and swells. This heterogeneity of material properties produces a corona-shape instability of the disk observed in experiments, Mora and Boudaoud (2006). In mathematical model Mora and Boudaoud (2006) consider only deformation of outer stripe assuming that the center region is rigid and static. This approach can not be used for biofilms because the variation of stiffness and thickness is smoother and besides it is not possible to divide the colony into regions of different properties. In order to include heterogeneous of material properties, we will modify the FvKEs by considering that all properties of the film and growth can vary along the film plane. We will neglect the variation of these properties along the vertical direction because biofilms are very thin.

Chapter 3

Mathematical model

In chapter 1 we have seen that biofilms are very complex structures where a lot of processes of nature take place. However it is possible to separate these phenomenae by taking into account time scales. According to Goriely and Ben Amar (2007) the fastest process is the mechanical deformation. In our work we will focus on wrinkling of *Bacillus subtilis* biofilm considering it from mechanical point of view and not taking into account biological effects which stay behind. This formulation leads us for the theory of thin plates considered in chapter 2. There are three sources of wrinkles: internal growth, interaction with the agar substratum, and heterogeneity of ECM properties. In this chapter we repeat our derivation published in Iakunin and Bonilla (2018) and present the mathematical models which includes all mentioned reasons.

We assume that ECM is hyperelastic and incompressible. Thus we consider the biofilm as a thin heterogeneous film bonded to a viscoelastic layer, as in Espeso et al. (2015). In that paper, a cellular automaton yields internal growth that is averaged and coupled with FvKEs according to Dervaux et al. (2009). We do not have any model for cellular behavior therefore we will define growth as an arbitrary function as it is done in Zhang et al. (2016). The interaction with a viscoelastic substratum we will include following the paper Huang and Im (2006) where Kelvin-Voigt model is used. During the derivation we will assume that all properties such as growth, Young modulus, and thickness are not constant but depend on coordinates.

Let the biofilm initial occupy the domain Ω_{3D} depicted in Figure 3.1. Let $\mathbf{X}$ be coordinates in this domain. The displacement vector is

$$\mathbf{U} = \mathbf{x} - \mathbf{X} = (U(X,Y,Z), V(X,Y,Z), W(X,Y,Z) + \zeta(X,Y)), \qquad (3.1)$$

where $\zeta(X,Y)$ is the displacement of the plate mid surface. Initial deflection of mid surface from the flat state has order of thickness h and therefore is

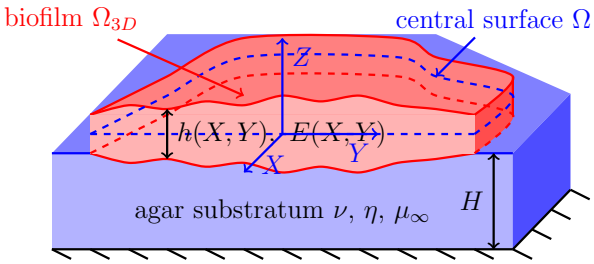

Figure 3.1: Initial domain occupied by the biofilm

very small. In this case there is no need in shell theory (Landau and Lifshitz (1986)) and we can assume that the central surface is flat.

3.1 Deformation under effect of internal growth

The biofilm undergoes deformation under effect of microscopical processes such as cell division, movement, and death. On a macroscopic layer we can detect two actions: the material growth or the material shrinking (that can be also considered as a "negative growth"). The usual approach for simulation of materials growing due to biological, chemical, or thermal processes is to split the deformation process into two parts: deformation due to growth and elastic deformation. In particular this idea was applied in Rodriguez et al. (1994) to biological tissues. For the classic mechanical deformation we have a reference configuration corresponding to the initial position of a body and a current configuration where the body has come during the deformation. The geometric deformation tensor $\mathbf{F}$ describes this transformation (Figure 3.2a). This value is a gradient of new coordinates respect to old ones $\mathbf{F} = \mathbf{I} + \nabla\mathbf{U}$. Geometric deformation tensor is used later to determine the energy of hyperelastic material and consequently all necessary values like stress and strain. For growing material there is a new configuration called virtual (Figure 3.2b). There may be no displacement field corresponding to the virtual configuration because the transformation was inducted by growth tensor $\mathbf{G}$ and has pure geometrical sense (one domain just turns into another one). Of course during this process discontinuities and overlapping may occur however in the final configuration they are impossible. This is the reason why the growth tensor should be followed by elastic deformation tensor $\mathbf{A}$ which purpose is to get rid of violations appeared at the previous step. Thus

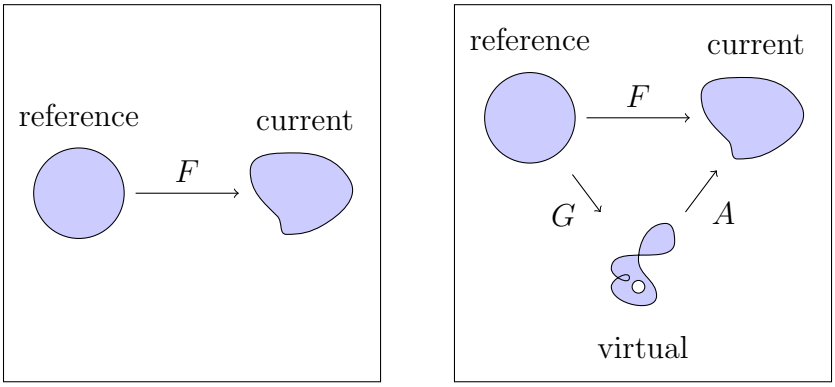

(a) (b)

Figure 3.2: Scheme of deformation of a body

the total deformation gradient is a composition of two tensors:

$$\mathbf{F} = \mathbf{I} + \nabla\mathbf{U}, \quad \mathbf{F} = \mathbf{AG},$$
$$F_{ij} = \delta_{ij} + U_{i,j} = \delta_{ij} + \frac{\partial U_i}{\partial X_j},\ A_{ij} = G^{-1}_{ij} + U_{i,k}G^{-1}_{kj}. \tag{3.2}$$

Sum over repeated indices is understood.

It is clear that growth tensor can lead to complete reorganization of the body, however we will bound ourselves in cases of small growth that is $\mathbf{G} = \mathbf{I} + \mathbf{g}$, where $\mathbf{g}$ is small. We will distinguish two types of growth: compatible and incompatible. The first one corresponds to some displacement field $\mathbf{U}^*$ or in other words $\mathbf{G} = \mathbf{I} + \nabla\mathbf{U}^*$. In this case the virtual configuration coincides with the current one and elastic deformation tensor $\mathbf{A}$ is identical so there are no elastic stresses. For compatible growth it is very simple to find the solution: it will be nothing but $\mathbf{U}^*$. For incompatible growth there is no displacement fields corresponding to the virtual configuration. This case is more interesting due to the biofilm undergoes elastic stresses and can bend from the flat state.

Despite that further we will deal with incompatible growths let us have a look on a compatible one and figure out what the components of $\mathbf{g}$ mean from physical point of view.

- g_{11}, g_{12}, g_{21} and g_{22} represent growth in in-plane direction. If they do not compose gradient of some vector-function they can produce breaks and overlapping. For example if we have azimuthal shrinking we will obtain a break between $\theta = 0$ and $\theta = 2\pi$. The elastic deformation tensor $\mathbf{A}$ has to get rid of this break and the simplest way to solve it is to glue it, what leads to conical shape of the film.

- g_{31} and g_{32} represent vertical growth or in other word changing of the biofilm thickness.
- g_{13} and g_{23} appears when different layers of the film grow in distinct directions or (and) with distinct rates.
- g_{33} represent changing of vertical growth rate in the vertical direction itself. It can produce gaps inside the film in virtual configuration.

3.2 Derivation of FvKEs for growing heterogeneous material

Firstly, we choose appropriate scales from natural assumptions about biofilms. Let L and $h = \gamma L$ (with $\gamma \ll 1$) be parameters representative of the biofilm diameter and thickness, respectively. Let the deflection ζ be of order κh with $\kappa > 1$ and $\kappa\gamma \ll 1$ so that $\zeta \ll L$. For biofilms, κ varies from 1 to 3, Asally et al. (2012). The order of magnitude of the basic space variables is listed in Table 3.1, whose entries have been obtained as follows:

(i) Assuming that the in-plane elastic strains are small and defections large, we only keep the gradients of ζ in the nonlinear part of the elastic strain tensor, Landau and Lifshitz (1986), so that their orders of magnitude satisfy $[U] = [V] = [\zeta]^2/L = \kappa^2 h^2/L$.

(ii) The biofilm is nearly incompressible and we set its Poisson ratio to 0.5. Therefore the variations of volume are zero: $0 = [Uyz]+[Vxz]+[Wxy]$. This implies $[W] = [U]h/L = \gamma[U] = \kappa^2\gamma^3 L$.

(iii) To determine $[g_{ij}]$, we consider an example of compatible growth for which the virtual configuration coincides with the current one in Figure 3.2b. In this case, $\mathbf{g}$ should equal the gradient of some displacement field $\mathbf{U}^*$ with zero deflection $\zeta = 0$. This implies $[g_{ij}] = [U]/L = \kappa^2\gamma^2$ for $i, j \in \{1, 2\}$, $[g_{i3}] = [U]/h = \kappa^2\gamma$ for $i \in \{1, 2\}$, $[g_{3j}] = [W]/L = \kappa^2\gamma^3$ for $j \in \{1, 2\}$, and $[g_{33}] = [W]/h = \kappa^2\gamma^2$. Note that $g_{ij}g_{jl} = O(\gamma^3)$.

These orders of magnitude complete Table 3.1. In the table $u_i(X, Y)$, $\zeta(X, Y)$, $g_{ij}(X, Y)$, $E(X, Y)$ and $h(X, Y)$ are in-plane displacements and deflection of the biofilm central surface from the flat state, components of the growth tensor, Young modulus and thickness of the biofilm, respectively.

Even though we have nondimensionalized all film properties, such as thickness, Young modulus and growth still depend on X and Y, but not on Z.

X, Y	Z, $h(X,Y)$	ζ	u_i	g_{ij}, g_{33}	g_{i3}	g_{3i}	$E(X,Y)$
L	$h=\gamma L$	κh	$\kappa^2\gamma^2 L$	$\kappa^2\gamma^2$	$\kappa^2\gamma$	$\kappa^2\gamma^3$	E

Table 3.1: Scales for the main properties and dimensions of growing biofilm($i,j \in \{1,2\}$)

3.2.1 3D Elastic strain tensor

We can get the elastic tensor $\mathbf{A}$ from (3.2) following Dervaux et al. (2009). We assume $\mathbf{G} = \mathbf{I} + \mathbf{g}$, with $\|\mathbf{g}\| \ll 1$. Expressing the elastic deformation tensor up to order γ^3 we obtian:

$$\mathbf{A} = \big(\mathbf{I} + \nabla\mathbf{U})(\mathbf{I} - \mathbf{g} + O(\gamma^3)\big) = \mathbf{I} + (\nabla\mathbf{U} - \mathbf{g}) - \nabla\mathbf{U}\mathbf{g} + O(\gamma^3). \quad (3.3)$$

Then the elastic strain tensor is

$$\varepsilon = \frac{1}{2}(\mathbf{A}^T\mathbf{A} - \mathbf{I}), \quad (3.4)$$

$$\varepsilon_{ij} = \frac{1}{2}(U_{i,j}+U_{j,i}+U_{k,i}U_{k,j}-g_{ij}-g_{ji})-(U_{i,k}g_{kj}+U_{j,k}g_{ki}) + O(\gamma^3). \quad (3.5)$$

This expression can be further simplified. According to Table 3.1, the dominant nonlinear component is $U_{k,i}U_{k,j} = \zeta_{,i}\zeta_{,j} + O(\gamma^3)$. Moreover, the last term on the right hand side of (3.5) is $O(\gamma^2)$ only it contains products involving g_{33}. Then (3.5) becomes

$$\varepsilon_{ij} = \frac{1}{2}(U_{i,j} + U_{j,i} + \zeta_{,i}\zeta_{,j} - g_{ij} - g_{ji}) - (\zeta_{,1}g_{13} + \zeta_{,2}g_{23})\delta_{i3}\delta_{j3} + O(\gamma^3). \quad (3.6)$$

3.2.2 Strain energy and 2D elastic strain tensor

The total energy of an incompressible biofilm made out of a Mooney-Rivlin material is

$$\mathcal{W} = \int_{\Omega_{3D}} [c_{10}(I_1-3) + c_{01}(I_2-3) - p(\det\mathbf{A}-1)]\det\mathbf{F}\, dXdYdZ, \quad (3.7)$$

$$I_1 = \mathrm{Tr}(\mathbf{A}^T\mathbf{A}), \quad I_2 = \frac{1}{2}[\mathrm{Tr}(\mathbf{A}^T\mathbf{A})]^2 - \frac{1}{2}\mathrm{Tr}[(\mathbf{A}^T\mathbf{A})^2]. \quad (3.8)$$

The term $p(\det\mathbf{A}-1)$ enforces the incompressibility condition $\det\mathbf{A} = 1$, and then the Jacobian $\det\mathbf{F} = \det\mathbf{G}$ is the local change of volume due to growth. From the energy (3.7), we obtain the stress tensor

$$\boldsymbol{\sigma} = 2c_{10}\mathbf{A}\mathbf{A}^T + 2c_{01}(I_1\mathbf{A}\mathbf{A}^T - \mathbf{A}\mathbf{A}^T\mathbf{A}\mathbf{A}^T) - p\mathbf{I}. \quad (3.9)$$

In plate theory we consider 3D object as 2D so there are different approaches to get rid of one dimension. Following Reddy (2003) we can distinguish three most common approaches: classical of Kirchhoff plate theory, first order or Reissner-Mindlin theory, and third order theory. The main difference between these theories consists in the way how they approximate vertical deformation inside the plate. The simplest one is Kirchhoff theory which is suitable for very thin films. In this theory every line initially orthogonal to the central surface maintain to be orthogonal after deformation. This condition leads to vanishing of vertical components of stress tensor on both surfaces of the plate (membrane assumption) and everywhere since the plate is thin. The main disadvantage of Kirchhoff theory is that it requires vertical displacement to be twice differentiable that leads to certain difficulties in numerical methods.

Another theory, developed for thicker plates is Reissner-Mindlin theory. In this approach we assume that vertical cross-section of the plate can rotate by angles θ_x and θ_y which are unknown and should be determined from equations. Thus the number of unknown function increase comparing with Kirchhoff theory but all unknown should be only once differentiable. The main problem of Reissner-Mindlin theory is that it predicts constant shear stress inside the plate but it is known that this stress should have parabolic profile. To resolve this issues a shear correction factor is used, Reddy (2003).

The most complex theory is third-order theory. This approach is generalization of Reissner-Mindlin theory which allows to plate cross-section not only rotate but also bend. It requires four more unknown functions but we obtain quite accurate approximation which can be used efficiently for thick composite plates, Reddy (2003). Another advantage is that first-order theory predicts parabolic profile of shear stress and therefore does not need shear correction factor.

Since biofilms are very thin the best choice for our problem is Kirchhoff theory. Thus we assume that on the top and bottom boundaries of the film, $\sigma_{13} = \sigma_{23} = \sigma_{33} = 0$, and these relations hold everywhere because the film is very thin. From the conditions $\sigma_{13} = \sigma_{23} = 0$, we find that $U_{i,3} + U_{3,i} - (g_{i3} - g_{3i}) = O(\gamma^2)$, $i \in \{1, 2\}$, Dervaux et al. (2009). In the absence of growth, these conditions are the usual ones in plate theory, equivalent to $\varepsilon_{13} = \varepsilon_{23} = 0$, Landau and Lifshitz (1986). The in-plane displacements become

$$\begin{aligned} U(X, Y, Z) &= u(X, Y) - Z\left(\frac{\partial \zeta(X, Y)}{\partial X} - g_{13}\right), \\ V(X, Y, Z) &= v(X, Y) - Z\left(\frac{\partial \zeta(X, Y)}{\partial Y} - g_{23}\right). \end{aligned} \tag{3.10}$$

Here $u(X,Y)$ and $v(X,Y)$ are the horizontal displacements of the central surface. The incompressibility condition, $\det\mathbf{A}=1$, can be used to write the invariants (3.8) of the tensor $\mathbf{A}^T\mathbf{A}$ in terms of invariants of the elastic strain. We have $0=\ln\det\left(\mathbf{A}^T\mathbf{A}\right)=2\,\mathrm{Tr}\,\boldsymbol{\varepsilon}-2\,\mathrm{Tr}\,\boldsymbol{\varepsilon}^2+O(\gamma^6)$ from which,

$$\mathrm{Tr}\,\boldsymbol{\varepsilon}=\mathrm{Tr}\,\boldsymbol{\varepsilon}^2+O(\gamma^6). \tag{3.11}$$

As $\varepsilon_{ij}=O(\gamma^2)$ and $\varepsilon_{ij}^2=O(\gamma^4)$, we get

$$\varepsilon_{33}=-(\varepsilon_{11}+\varepsilon_{22})+O(\gamma^4). \tag{3.12}$$

According to the membrane assumption, $\sigma_{33}=0$, which, together with (3.11), provides the hydrostatic pressure,

$$p=2c_{10}+4c_{01}+4(c_{10}+c_{01})\varepsilon_{33}+O(\gamma^3). \tag{3.13}$$

We now use (3.11)-(3.13) to rewrite the strain energy (3.7) in terms of the in-plane elastic strains:

$$\begin{aligned}\mathcal{W}&=\int_{\Omega_{3D}}[2(c_{10}+c_{01})\,\mathrm{Tr}\,\boldsymbol{\varepsilon}^2]\det\mathbf{F}\,dXdYdZ\\&=\int_{\Omega_{3D}}\frac{2E}{3}\left(\varepsilon_{11}^2+\varepsilon_{22}^2+\varepsilon_{11}\varepsilon_{22}+\varepsilon_{12}^2\right)dXdYdZ,\end{aligned} \tag{3.14}$$

up to $O(\gamma^5)$ terms. Here E is the Young modulus,

$$E=6\,(c_{10}+c_{01}). \tag{3.15}$$

According to (3.6) and (3.10), the 2D in-plane elastic strains are

$$\varepsilon_{ij}^{2D}=\frac{1}{2}\,(u_{i,j}+u_{j,i}-g_{ij}-g_{ji}+\zeta_{,i}\zeta_{,j})-Z\left(\zeta_{,ij}-\frac{1}{2}(g_{i3,j}+g_{j3,i})\right), \tag{3.16}$$

where $i,j\in\{1,2\}$. Then the energy (3.14) can be written as

$$\mathcal{W}=\frac{1}{2}\int_{\Omega_{3D}}\boldsymbol{\varepsilon}^{2D}:\boldsymbol{\sigma}^{2D}dXdYdZ. \tag{3.17}$$

where the in-plane stresses producing (3.14) are

$$\sigma_{ij}^{2D}=\frac{2E}{3}\left(\varepsilon_{ij}^{2D}+\delta_{ij}\varepsilon_{kk}^{2D}\right),\ i,j\in\{1,2\}. \tag{3.18}$$

3.2.3 FvKEs

We now expand the strain energy density (3.17) in powers of Z and integrate over Z from $-h(X,Y)/2$ to $h(X,Y)/2$, where $h(X,Y)$ is the variable biofilm thickness. Due to symmetry of the film respect to central surface, only terms independent of Z and quadratic in Z contribute to the integral. The terms independent of Z produce the stretching energy and the quadratic terms produce the bending energy. If we add a contribution corresponding to external forces, the resulting energy is

$$\mathcal{W} = \mathcal{W}_{bend} + \mathcal{W}_{stretch} - \int_\Omega h\mathbf{f}\cdot\mathbf{U}\,dXdY, \tag{3.19}$$

where

$$\mathcal{W}_{bend} = \int_\Omega \frac{D(X,Y)}{2}\Bigg[\left(\Delta\zeta - g_{13,x} - g_{23,y}\right)^2 + \left(\zeta_{,xy} - \frac{g_{13,y}+g_{23,x}}{2}\right)^2 - \left(\zeta_{,xx} - g_{13,x}\right)\left(\zeta_{,yy} - g_{23,y}\right)\Bigg] dXdY, \tag{3.20}$$

$$D(X,Y) = \frac{E(X,Y)h^3(X,Y)}{9}, \tag{3.21}$$

$$\mathcal{W}_{stretch} = \frac{1}{2}\int_\Omega h(X,Y)\boldsymbol{\varepsilon}^{(0)} : \boldsymbol{\sigma}^{(0)}\,dXdY, \tag{3.22}$$

$$\boldsymbol{\varepsilon}^{(0)} = \boldsymbol{\varepsilon}^{2D}|_{Z=0}, \quad \boldsymbol{\sigma}^{(0)} = \boldsymbol{\sigma}^{2D}|_{Z=0}, \tag{3.23}$$

and $\mathbf{f}$ is external force. Formulas (3.20) - (3.23) together with definitions of stress and elastic strain, (3.16) and (3.18), provide a complete description of the biofilm deformation process due to growth. Variation of energy with respect to ζ and with respect to the in-plane elastic strains produce the equations:

$$\Delta\left(D\left(\Delta\zeta - C_M\right)\right) - [D,\zeta] - \nabla\cdot\left(h\boldsymbol{\sigma}^{(0)}\cdot\nabla\zeta\right) = P - \frac{1}{2}\nabla\nabla : \left(D\begin{pmatrix} g_{23,y} & -\frac{g_{13,y}+g_{23,x}}{2} \\ -\frac{g_{13,y}+g_{23,x}}{2} & g_{13,x}\end{pmatrix}\right), \tag{3.24}$$

$$\nabla\cdot\left(h\boldsymbol{\sigma}^{(0)}\right) = h\begin{pmatrix} f_1 \\ f_2\end{pmatrix}, \tag{3.25}$$

$$[a,b] = \frac{1}{2}(a_{,xx}b_{,yy} + a_{,yy}b_{,xx} - 2a_{,xy}b_{,yx}), \tag{3.26}$$

$$C_M = g_{13,x} + g_{23,y}. \tag{3.27}$$

Here P is the vertical component of the force per unit area. Third derivatives of growth tensor components g_{13} and g_{23} in equation (3.24) disappear after

expansion of brackets. Equations (3.24)-(3.25) are FvKEs modified by heterogeneous biofilm growth. For compatible growth, the term $\Delta(DC_M)$, also obtained by Dervaux et al. (2009), represents the curvature induced by the different horizontal growing rate of distinct film layers. As C_M does not always correspond to a physical surface, it can produce bending stresses due to growth incompatibility. The term $[D, \zeta]$ stands for the influence of material heterogeneity on deflection. The last term in (3.24) takes into account the additional source of deformation caused by material properties and growth that are not constant along the horizontal direction.

For a film expanding freely on a surface, (3.24)-(3.25) should be accompanied by the following boundary conditions:

$$\begin{cases} 2(\Delta\zeta - g_{i3,i}) - (\zeta_{,ij} - g_{i3,j})l_i l_j = 0, \\ 2\mathbf{n}\cdot\nabla[D(\Delta\zeta - g_{i3,i})] + \mathbf{l}\cdot\nabla\left[D\left(\zeta_{,ij} - \dfrac{g_{i3,j} + g_{j3,i}}{2}\right)l_i n_j\right] = 0, \\ \boldsymbol{\sigma}^{(0)}\cdot\mathbf{n} = \mathbf{0}. \end{cases} \tag{3.28}$$

Here $\mathbf{l}$ and $\mathbf{n}$ are tangential and normal unit vectors, respectively.

In the next section we will include in our model the interaction with the substratum. As the film is very thin, there are no loads applied to its top and bottom surfaces (the membrane assumption implies that the corresponding stresses are zero). Thus the external forces will be body forces f_1 and f_2 in the in-plane directions, and the pressure P in the vertical direction.

3.3 Viscoelastic layer

Bacillus subtilis biofilms may grow on a substratum from which the bacteria take resources to survive. The substratum influences the shape of the colony and can change the geometry and wave number of wrinkle patterns. Following Huang (2005), we consider a compressible, viscoelastic and homogeneous substratum that is much thicker than the biofilm ($H \gg h$). A sketch is depicted in Figure 3.3. In this section, $z = 0$ and $z = -H$ are the top and the bottom of the viscoelastic layer, respectively.

The viscoelastic material strain $\mathcal{E}$ and stress Σ are:

$$\begin{aligned} \mathcal{E}_{ij} &= \frac{1}{2}\left(\frac{\partial U_i}{\partial x_j} + \frac{\partial U_j}{\partial x_i}\right), \\ \Sigma_{ij} &= \int_{-\infty}^{t}\left[2\mu(t-\tau)\frac{\partial \mathcal{E}_{ij}}{\partial \tau} + \delta_{ij}\lambda(t-\tau)\,\mathrm{Tr}\left(\frac{\partial \mathcal{E}}{\partial \tau}\right)\right]d\tau. \end{aligned} \tag{3.29}$$

Here $\mathbf{U}$ is the displacement vector, and μ with λ are Lamé coefficients which are functions of time. Many viscoelastic materials can be described by the

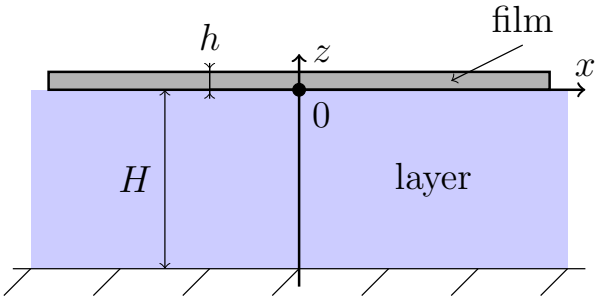

Figure 3.3: A film on a viscoelastic substratum.

following values of these functions:

$$\mu(t) = \mu_\infty + \eta\,\delta(t), \quad \lambda(t) = \mu(t)\frac{2\nu}{1-2\nu}, \tag{3.30}$$

in which μ_∞ is the rubbery modulus, η is the viscosity, and ν is the Poison ratio, $\delta(t)$ is Dirac δ-function. This model is equivalent to Kelvin-Voigt material which can be represented as parallel connection of a spring with stiffness μ_∞ and damper with viscocity η. The behavior of the layer during the deformation is given by balance of momentum:

$$\Sigma_{ij,j} = 0 \text{ everywhere in the layer.} \tag{3.31}$$

The displacements at the top of the substratum are the same as the displacements at the bottom of the biofilm, thereby producing the adherence condition:

$$\begin{aligned} &U_1 = u, \quad U_2 = v,\ U_3 = \zeta,\ \text{at } z = 0, \\ &U_i = 0,\ i \in \{1,2,3\} \text{ at } z = -H. \end{aligned} \tag{3.32}$$

In addition, the condition of mechanical equilibrium at the interface is:

$$\Sigma_{33} = -P,\ \Sigma_{3i} = hf_i,\ i \in \{1,2\} \text{ at } z = 0. \tag{3.33}$$

In paper Huang and Suo (2002b) equations (3.31) are solved analytically in 2D using Laplace transform to get rid of integral, Airy potential to reduce number of unknowns, and separation of variables to resolve obtained spacial PDEs. This method is quite complex and cannot be generalized in 3D case therefore we will use another approach based on scales. Our method is much simpler, can be written for 3D substratum, and leads to the same results as one of R. Huang with coauthors. As $x, y = O(L)$, $z = O(H)$ and, from the boundary condition (3.32), we have $[U_i] = O(\gamma h)$ $(i \in \{1,2\})$,

$U_3 = O(h) \ll H$. Then the largest terms in the momentum balance equation (3.31) are

$$0 = \int_{-\infty}^{t} \mu(t-\tau)\frac{\partial U_{i,33}}{\partial \tau}\, d\tau, \quad i \neq 3,$$
$$0 = 2\int_{-\infty}^{t} \mu(t-\tau)\left(\frac{\nu}{1-2\nu} + \frac{\partial}{\partial \tau}\right) U_{3,33}\, d\tau. \tag{3.34}$$

We have neglected terms that are a factor H/L smaller than those kept in (3.34) and used (3.30). From (3.34) and the conditions (3.32), we obtain

$$\frac{\partial^2 U_i}{\partial z^2} = 0 \Longrightarrow U_i(x,y,z,t) = u_i(x,y,t)\Big(1 + \frac{z}{H}\Big),$$
$$u_1 = u,\ u_2 = v, \text{ and } U_3(x,y,z,t) = \zeta(x,y,t)\Big(1 + \frac{z}{H}\Big).$$

Insertion in (3.29) produces

$$\Sigma_{3i} = \mu_\infty \frac{u_i}{H} + \frac{\eta}{H}\frac{\partial u_i}{\partial t}\left[1 + O\left(\frac{H}{L}\right)\right] \quad (i \neq 3),$$
$$\Sigma_{33} = \frac{2}{H}\frac{1-\nu}{1-2\nu}\left(\mu_\infty \zeta + \eta\frac{\partial \zeta}{\partial t}\right)\left[1 + O\left(\frac{H}{L}\right)\right],$$

and therefore the conditions (3.33) yield

$$\mu_\infty u_i + \eta\frac{\partial u_i}{\partial t} = hHf_i, \quad i \in \{1,2\},$$
$$2\mu_\infty \zeta + 2\eta\frac{\partial \zeta}{\partial t} = -H\frac{1-2\nu}{1-\nu}P. \tag{3.35}$$

3.4 Full system of equations

Putting together (3.35) and (3.24), we get the system:

$$\frac{\partial \zeta}{\partial t} = -\frac{\mu_\infty}{\eta}\zeta - \frac{H(1-2\nu)}{2\eta(1-\nu)}P, \tag{3.36}$$
$$\frac{\partial \mathbf{u}}{\partial t} = -\frac{\mu_\infty}{\eta}\mathbf{u} + \frac{H}{\eta}\nabla\cdot(h\boldsymbol{\sigma}^{(0)}), \tag{3.37}$$

where P is given by (3.24). For constant $h(X,Y)$ and $D(X,Y)$, these equations are the same used in Espeso et al. (2015). We now nondimensionalize

these equations using the units listed in Table 3.2, thereby obtaining

$$\frac{\partial \zeta}{\partial t} = -\beta\zeta - \frac{(1-2\nu)\kappa^2}{2(1-\nu)}\tilde{P} \tag{3.38}$$

$$\nabla\cdot(h\boldsymbol{\sigma}^{(0)}) = \gamma^2\left(\frac{\partial \mathbf{u}}{\partial t} + \beta\mathbf{u}\right), \quad \beta = \frac{\mu_\infty L^4}{EHh^3}. \tag{3.39}$$

Here $\tilde{P}$ is the pressure given by (3.24) and scaled according the Table 3.2. Analysis of time scaling shows that mechanical relaxation of the biofilm in the horizontal direction is much faster than that in the vertical direction. Thus transient derivative of $\mathbf{u}$ can be neglected that gives the final model describing deformation of heterogeneous biofilm growing on agar substratum:

$$\begin{aligned}\frac{\partial \zeta}{\partial t} = -\beta\zeta - \frac{(1-2\nu)\kappa^2}{2(1-\nu)}\Bigg\{ &\frac{1}{\kappa^2}\Delta\left(D\left(\Delta\zeta - g_{13,x} - g_{23,y}\right)\right) - \nabla\cdot\left(h\boldsymbol{\sigma}^{(0)}\cdot\nabla\zeta\right) \\ &+\frac{1}{2\kappa^2}\left(\nabla\nabla : \left(D\begin{pmatrix} g_{23,y} & -\frac{g_{13,y}+g_{23,x}}{2} \\ -\frac{g_{13,y}+g_{23,x}}{2} & g_{13,x}\end{pmatrix}\right) + \frac{1}{\kappa^2}\left[D,\zeta\right]\right)\Bigg\}\end{aligned} \tag{3.40}$$

$$\nabla\cdot(h\boldsymbol{\sigma}^{(0)}) = \gamma^2\beta\mathbf{u}. \tag{3.41}$$

This equation should be equipped with boundary conditions (3.28). There are three main parameters which describe behavior of the system:

(i) $\kappa > 1$ is ratio between the deflection and thickness of biofilm and corresponds to geometrical nonlinearity: the bigger κ is the higher is influence of nonlinear effects;

(ii) β is proportional to the ratio between the stiffness of the agar layer and that of the biofilm and represents influence of the substratum;

(iii) $\gamma = h/L$ is the ratio between thickness and in-plane size of the biofilm.

The parameter β can be small for mature thick biofilms on a soft substratum with high concentration of water or large for thin films and stiff agar layer. The particular case when we can neglect β will be considered in the next subsection.

3.4.1 Particular case of absence of horizontal stretching stress

When the substratum is soft enough it is possible to neglect horizontal stretching forces. Even though in most experiments agar is much stiffer

x, y	z	ζ, U_3	U_1, U_2, $\mathbf{u}$	$\boldsymbol{\sigma}^{(0)}$	P	t
L	H	κh	$\kappa^2\gamma h$	$E\kappa^2\gamma^2$	$E\kappa^3\gamma^4$	$\frac{\eta h}{E\gamma^4 H}$

Table 3.2: Scales characterizing deformation of a film on a substratum. Here E is Young modulus scale from Table 3.1, $h \ll H \ll L$.

than the biofilm we will consider this case because it leads to interesting theoretical results and can be used to understand general idea of pattern formation.

If β is small equation (3.41) turns into

$$\nabla\cdot(h\boldsymbol{\sigma}^{(0)}) = 0,$$

and since the stress tensor $\boldsymbol{\sigma}^{(0)}$ is 2-dimensional it can be solved using the Airy potential χ:

$$h\sigma_{11}^{(0)} = \chi_{,yy}, \quad h\sigma_{22}^{(0)} = \chi_{,xx}, \quad h\sigma_{12}^{(0)} = -\chi_{,xy}. \tag{3.42}$$

After straightforward algebra, we can eliminate in-plane displacements, and the system (3.40)-(3.41) becomes

$$\frac{\partial\zeta}{\partial t} = -\beta\zeta - \frac{(1-2\nu)\kappa^2}{2(1-\nu)}\left\{\frac{1}{\kappa^2}\Delta\left(D\left(\Delta\zeta - g_{13,x} - g_{23,y}\right)\right) - 2\left[\chi,\zeta\right]\right.$$
$$\left. + \frac{1}{2\kappa^2}\left(\nabla\nabla\colon\left(D\begin{pmatrix} g_{23,y} & -\frac{g_{13,y}+g_{23,x}}{2} \\ -\frac{g_{13,y}+g_{23,x}}{2} & g_{13,x}\end{pmatrix}\right) + \frac{1}{\kappa^2}\left[D,\zeta\right]\right)\right\}, \tag{3.43}$$

$$\Delta\left(\frac{1}{Eh}\Delta\chi\right) - 3\left[\chi,\frac{1}{Eh}\right] + [\zeta,\zeta] - \Psi = 0, \tag{3.44}$$

$$\Psi = g_{12,xy} + g_{21,xy} - g_{11,yy} - g_{22,xx}. \tag{3.45}$$

Here Ψ represents the Gaussian curvature of the biofilm central surface which is due only to the growth tensor to the order of approximation considered here. The boundary is free and the normal stress vanishes there, so that the boundary conditions are

$$\begin{cases} 2(\Delta\zeta - g_{i3,i}) - (\zeta_{,ij} - g_{i3,j})l_i l_j = 0, \\ 2\mathbf{n}\cdot\nabla[D(\Delta\zeta - g_{i3,i})] + \mathbf{l}\cdot\nabla\left[D\left(\zeta_{,ij} - \dfrac{g_{i3,j}+g_{j3,i}}{2}\right)l_i n_j\right] = 0, \\ \chi = \dfrac{\partial\chi}{\partial n} = 0, \end{cases} \tag{3.46}$$

where $\mathbf{l}$ and $\mathbf{n}$ are the tangential and normal unit vectors, respectively. For homogeneous D, h, time independent ζ and $\beta = 0$, equations (3.43) and (3.44) become those deduced by Dervaux et al. (2009).

It is important to note that even though equations (3.43) and (3.44) are quite similar, the system is linear with respect to the Airy potential but nonlinear with respect to the deflection. One of the consequences of this feature is that, for any fixed ζ, the Airy potential exists and is unique, whereas the same fixed χ can be generated by different displacement fields. It is remarkable that these equations do not contain time derivatives of χ, which is quite beneficial for designing a numerical solver.

Chapter 4

Homogeneous radial and azimuthal growth of a round film

An analytical solution of modified FvKEs cannot be found in the general case. Even in the simplified case of equations (3.43)-(3.44) we can only carry out an asymptotic analysis. In this chapter we will do it for a case of homogeneous anisotropic growth in polar coordinates as it was done in our publication Iakunin and Bonilla (2018). Even in this simple case, biofilm behavior can be complex. Let us consider example indicated in Dervaux and Ben Amar (2008): a circular homogeneous film of nondimensional radius 1, the interaction with the agar substratum is ignored. The biofilm deforms under the combination of two types of spatially uniform growth: radial g_r and azimuthal g_θ. The growth tensors in polar ($\mathbf{g}^{(p)}$) and Cartesian ($\mathbf{g}^{(c)}$) coordinates are

$$\mathbf{g}^{(p)} = \begin{pmatrix} g_r & 0 & 0 \\ 0 & g_\theta & 0 \\ 0 & 0 & 0 \end{pmatrix} \Rightarrow \mathbf{g}^{(c)} = \frac{1}{x^2+y^2} \begin{pmatrix} g_r x^2 + g_\theta y^2 & (g_r - g_\theta)xy & 0 \\ (g_r - g_\theta)xy & g_r y^2 + g_\theta x^2 & 0 \\ 0 & 0 & 0 \end{pmatrix}, \quad (4.1)$$

respectively. For example, in the case of pure azimuthal shrinking ($g_r = 0$ and $g_\theta < 0$) depicted in Figure 4.1, the growth tensor transforms the circular film in a sector with discontinuity (virtual configuration). However, the film should be continuous in the final current configuration, and therefore stresses emerge to close the gap and the film bends into a cone. Nevertheless if the virtual configuration is possible, i.e., it does not contain discontinuities and overlaps, then it will coincide with the current configuration, and no stresses emerge. As was mentioned in chapter 3, these growths are called compatible and they do not provoke deflection of the film, other growth

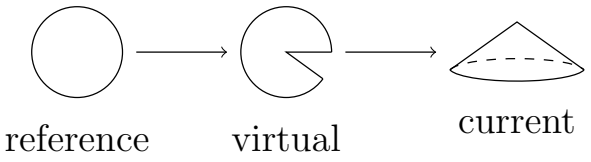

Figure 4.1: Azimuthal shrinking of a round film.

types are incompatible.

A straightforward calculation shows that the Gaussian curvature Ψ induced by (4.1) is given by:

$$\Psi(r,\theta) = \frac{k\,\delta(r)}{r}, \quad k = g_r - g_\theta, \tag{4.2}$$

where $\delta(r)$ is the Dirac delta-function. For a homogeneous film, time-independent ζ and $\beta = 0$, the system (3.43)-(3.44) becomes

$$\begin{cases} \dfrac{1}{18\kappa^2}\Delta^2\zeta - [\chi,\zeta] = 0, \\ \qquad \Delta^2\chi + [\zeta,\zeta] = \dfrac{k\,\delta(r)}{r}. \end{cases} \tag{4.3}$$

Note that for isotropic growth, $g_r = g_\theta$, the Gaussian curvature vanishes and $\chi = \zeta = 0$ solves (4.3). This is an example of the compatible growth hence there are no stresses or deflection. In the remaining cases, the delta-function makes the solution less smooth and designing appropriate numerical methods is quite challenging. It is interesting to note that solution depends only on the difference between radial and azimuthal growths. Particularly there is no difference between pure radial growth, $g_r > 0$, and pure azimuthal shrinking, $g_\theta < 0$.

In this chapter we will perform asymptotic analysis of the system (4.3) respect to parameter κ. For simplicity we will consider only positive k when we expect that the deformed film has a conical shape (see Figure 4.1). Firstly we will consider another particular case of developable surfaces which is quite well studied and allow to distinguish main peculiarity of film wrinkling and buckling phenomena.

4.1 Developable surfaces

Developable surface is a surface with zero Gaussian curvature. It can be constructed by picking a straight line or an interval and moving it continuously

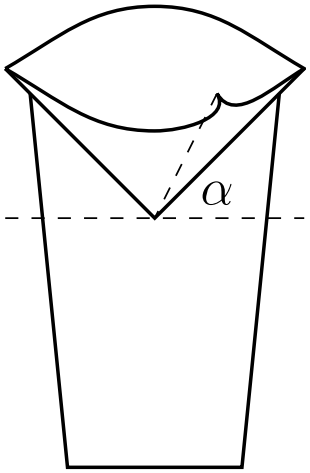

Figure 4.2: Formation of d-cone.

without bending. Particularly a cylinder with a base given by a curve γ is developable because it is a result of moving a vertical interval along that curve. Analogously a cone is developable everywhere far from its tip. Developable surfaces are quite important for plate bending problem. The main reason can be seen from Gaussian *"theorema egregium"* which says that a surface maintain its Guassian curvature in any point if it is transformed without stretching or enlargement, e.g. it is impossible to draw a map of the world which maintains areas because sphere of radius R has curvature $1/R^2$ whereas flat surface has zero curvature. If we apply *"theorema egregium"* to developable surfaces we get that they can be obtained from flat plate only by its bending. Since for thin films bending energy is much smaller than stretching one developable surfaces are good candidates for minimizers of total mechanical energy.

In paper of Cerda et al. (1997) a bending of flat circular film into asymmetric cone is studied. This transformation can be done thereby penetration of the film into a cylindrical glass (Figure 4.2). There are two most interesting regions: the fold where the symmetry is broken and cone's tip where the surface is not developable.

In Cerda et al. (1997) the solution is sought in shape:

$$\zeta(r,\theta) = rq(\theta), \quad q(\theta) \geq \alpha, \tag{4.4}$$

where α is opening angle induced by the contact with glass. According to definition of developable surface any stretching strain should vanish everywhere

that is

$$\varepsilon_{rr} = u_{r,r} + \frac{1}{2}\zeta_{,r}^2 = 0, \tag{4.5}$$

$$\varepsilon_{\theta\theta} = \frac{1}{r}u_{\theta,\theta} + \frac{u_r}{r} + \frac{1}{2r^2}\zeta_{,\theta}^2 = 0, \tag{4.6}$$

$$\varepsilon_{r\theta} = \frac{1}{2}\left(\frac{1}{r}u_{r,\theta} + u_{\theta,r} - \frac{1}{r}u_\theta + \frac{1}{r}\zeta_{,\theta}\zeta_r\right) = 0. \tag{4.7}$$

From equations (4.5) - (4.7) we can express displacements u_r and u_θ in terms of function $q(\theta)$:

$$u_r = -\frac{r}{2}q^2(\theta), \tag{4.8}$$

$$u_\theta = \frac{r}{2}\int_0^\theta \left(q^2(\phi) - \left(\frac{dq(\phi)}{d\phi}\right)^2\right) d\phi, . \tag{4.9}$$

From boundary condition $u_\theta(r,0) = u_\theta(r,2\pi)$ we obtain a constrain for $q(\theta)$ which repeats Gauss-Bonnet theorem:

$$\int_0^{2\pi} \left(q^2(\theta) - \left(\frac{dq(\theta)}{d\theta}\right)^2\right) d\theta = 0.. \tag{4.10}$$

Now the only one unknown function is $q(\theta)$ which can be found from minimization of augmented energy functional:

$$\mathcal{L} = \frac{1}{2}\int_0^{2\pi} \left(q(\theta) + \frac{d^2q(\theta)}{d\theta^2}\right)^2 d\theta + \frac{\lambda}{2}\int_0^{2\pi} \left(q^2(\theta) - \left(\frac{dq(\theta)}{d\theta}\right)^2\right) d\theta + \int_0^{2\pi} b(\theta)(\alpha - q(\theta))d\theta, \tag{4.11}$$

where first term corresponds to bending energy, second term represents Gauss-Bonnet theorem constrain (4.10) with Lagrange multiplier $\lambda \in \mathbb{R}$, and the last term is contact constrain $\alpha \leq q(\theta)$ with Lagrange multiplier $b(\theta) \geq 0$ for all $\theta \in [0; 2\pi]$. Setting the function (4.11) to its minimum Cerda et al. (1997) find expression for $q(\theta)$ and analyze buckling conditions and formation of the fold. However the solution (4.4) does not hold true in zone near the tip and to study behavior in this area another approach is required. For general case of asymmetric cone it is not possible to find the solution near tip or even estimate size of this area, Audoly and Pomeau (2010). It happens because asymmetry leads to crescent form of the inner zone. However if angle α is

small enough it is possible estimate the size of smoothed zone near tip. In paper Cerda et al. (1997) it is done by balancing bending and stretching energy. The radius of center zone in this case is proportional to h/α where h is thickness of the sheet and α is the cone's opening angle.

In our case the solution is not given by a developable surface because we have curvature Ψ induced by growth. However the similar idea will work out. The difference is that in order to find the surfaces of given curvature which will be approximation of solution we have to solve Monge-Ampère equation (MAE). Similarly to developable surface case we may have intersection of sharp bends where we have to insert specific layers. In the case of cone emergent due to growth the regions where the solution of FvKEs diverges from MAE are cone tip and the boundary. For the core region we will provide an estimation of radius which coincides with one obtained by Cerda et al. (1997) and expand the solution in terms of radius r. For the boundary layer it is possible to simplify the problem.

4.2 Monge-Ampère equation (MAE)

The system (4.3) cannot be solved analytically. However, in the limit of thin films, the deflection-to-thickness ratio κ goes to infinity, and the bending coefficient $1/(18\kappa^2) \to 0$. Neglecting it yields $\chi = 0$ and (4.3) becomes the MAE

$$[\zeta, \zeta] = \frac{\zeta_{,r}\zeta_{,rr}}{r} + \frac{1}{r^2}\left[\zeta_{,rr}\zeta_{,\theta\theta} - \left(\zeta_{,r\theta} - \frac{1}{r}\zeta_{,\theta}\right)^2\right] = k\frac{\delta(r)}{r}. \tag{4.12}$$

For $k > 0$, (4.12) has the radial solution

$$\zeta(r, \theta) = \pm\sqrt{2k}r, \quad \chi = 0, \tag{4.13}$$

representing two cones. For negative k, we can seek a solution

$$\zeta(r, \theta) = \pm\alpha r \sin(\omega\theta), \tag{4.14}$$

that, inserted into (4.12) and integrating over the domain, yields

$$\frac{\alpha^2}{4}(1 - \omega^2) = k. \tag{4.15}$$

The deflection should be continuous, that is $\zeta(r, \theta) = \zeta(r, \theta + 2\pi)$, so ω should be a natural number. Thus from (4.15) we obtain an infinite number of solutions representing a set of coronas:

$$\zeta_n(r, \theta) = \pm 2\sqrt{\frac{|k|}{n^2 - 1}} r \sin(n\theta), n \in \mathbb{N} \setminus \{1\}. \tag{4.16}$$

The solution with $n = 2$ is a saddle with smaller maximum deflection than that of the cone (4.13). For larger values of n, we have more complex corona patterns of decreasing amplitude.

There are two problems with the approximate solutions (4.13) and (4.16). Firstly, they do not have second derivatives at the origin, and therefore their bending strains (3.16) cannot be determined. This happens because (4.13) and (4.16) represent the transformation of an infinitely thin surface due to growth but the real biofilm has a finite thickness. Secondly, (4.13) and (4.16) do not satisfy the boundary conditions at $r = 1$. To fix these shortcomings, we need to insert a corner layer at $r = 0$ and a boundary layer at $r = 1$.

4.3 Cone solution emergent due to growth

For simplicity, consider a radially symmetric solution approximated by the cone (4.13). In this case, the system (4.3) contains only radial derivatives of ζ and χ. Then we can substitute

$$\zeta_{,r} = \sqrt{2k}\phi(r), \quad \chi_{,r} = 2k\psi(r), \quad \epsilon = \frac{1}{18k\kappa^2}, \tag{4.17}$$

in the system (4.3), which becomes

$$\begin{cases} \dfrac{1}{r}\dfrac{d}{dr}\left[\epsilon r \dfrac{d}{dr}\left(\phi' + \dfrac{\phi}{r}\right) - \psi\phi\right] = 0, \\ \dfrac{1}{r}\dfrac{d}{dr}\left[r\dfrac{d}{dr}\left(\psi' + \dfrac{\psi}{r}\right) + \dfrac{1}{2}\phi^2\right] = \dfrac{\delta(r)}{2r}. \end{cases} \tag{4.18}$$

Using Dirichlet boundary conditions due to (3.46) and symmetry, we solve the second equation in (4.18) for ψ:

$$\psi = \frac{r}{4}\left[\int_r^1 \frac{\phi^2 - 1}{s} ds - \int_0^1 s(\phi^2 - 1)\, ds\right] + \frac{1}{4r}\int_0^r s(\phi^2 - 1) ds. \tag{4.19}$$

Integrating once (4.18) from r to 1 and using the boundary conditions at $r = 1$ and (4.19), we obtain

$$\begin{cases} \epsilon r \dfrac{d}{dr}\left(\phi' + \dfrac{\phi}{r}\right) - \psi\phi = 0, \\ r\dfrac{d}{dr}\left(\psi' + \dfrac{\psi}{r}\right) + \dfrac{\phi^2}{2} = \dfrac{1}{2}\eta(r). \end{cases} \tag{4.20}$$

Now we can consider more precisely the layers and derive reduced equations in both cases.

4.3.1 Boundary layer at $r = 1$

Let $r = 1 - \delta_r \rho$, $\psi = \delta_\psi \Psi(\rho)$, $\phi = \Phi(\rho)$. Then (4.20) produces the dominant balances,

$$\frac{\epsilon}{\delta_r^2}\Phi'' = \delta_\psi \Psi\Phi, \quad \frac{\delta_\psi}{\delta_r^2}\Psi'' = \frac{1-\Phi^2}{2},$$

from which

$$\delta_r = \epsilon^{1/4}, \quad \delta_\psi = \sqrt{\epsilon}.$$

If we take into account scaling given in the Table 3.1 we obtain that the layer size $\delta_r \sim h^{1/2}$, where h is film thickness. Inserting

$$\psi = \sqrt{\epsilon}\Psi(\rho),\ \phi = \Phi(\rho),\ \rho = \frac{1-r}{\epsilon^{1/4}},$$

in (4.20), and setting $\epsilon \to 0+$, we obtain the reduced equations

$$\begin{cases} \Phi'' = \Psi\Phi, \\ \Psi'' = \dfrac{1-\Phi^2}{2}. \end{cases} \tag{4.21}$$

It is immediate to check that $E = \Psi'^2 - \Phi'^2 - (1-\Phi^2)\Psi$ is an integral of motion of this Hamiltonian system. Both equilibrium points $\Phi = \pm 1$, $\Phi' = 0$, $\Psi = \Psi' = 0$ have $E = 0$ and are saddle-spirals. Equations (4.21) are invariant under the transformation $\rho \to -\rho$, $\Phi \to -\Phi$. The boundary layer corresponds to half of a heteroclinic connection between the equilibrium points that starts at $\rho = 0$ (the boundary point $r = 1$). To capture numerically this trajectory, we have to solve the linearized version of (4.21) about the equilibrium point $\Phi = 1$ keeping $E = 0$, pick an initial point from this linearized solution and solve (4.21) for negative times. We stop the solver when the trajectory is sufficiently close to satisfying $\Psi = 0$ ($\chi_{,r} = 0$) and $\Phi' = \frac{1}{2}\epsilon^{1/4}\Phi$ ($2\Delta\zeta = \zeta_{,r}$). Of course these conditions are not satisfied in the same time for an arbitrary initial point but we can solve the problem numerically for a few points and choose the best one.

Figure 4.3 depicts the profiles of $\phi(r)$ and $\psi(r)$ at the boundary layer for three different values of $k = 0.1/\gamma^2$ what corresponds to 10% radial growth of biofilms with different thickness. The derivative of ζ exhibits a small fold (local maximum) near $\rho = 0$ ($r = 1$) and it matches that of the cone as $\rho \to \infty$. The boundary layer approximation works better for thin films and fails for thick ones.

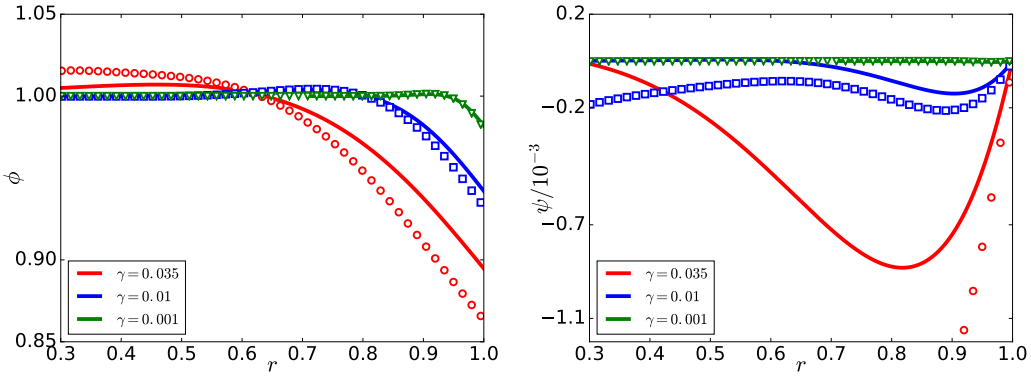

(a) (b)

Figure 4.3: Profiles of (a) ϕ, and (b) ψ at the $r = 1$ boundary layer for different values of γ. Markers correspond to numerical solution of full 1D problem (4.20) and solid lines correspond to the boundary layer approximation obtained by solving the reduced problem (4.21) with $\psi = 0$, $\phi' = \epsilon^{1/4}\phi$ at the initial point.

4.3.2 Corner layer at $r = 0$.

The corner layer should resolve the singularity at the origin and match the outer solution (4.17) with $\phi = 1$ and $\chi = 0$. Let $R = r/\delta_1(\epsilon)$, $\phi = R + \Phi$, $\psi = \delta_1\Psi$. Equations (4.20) become

$$\frac{\epsilon}{\delta_1} R \frac{d}{dR}\left(\Phi' + \frac{\Phi}{R}\right) - \delta_1\Psi(R + \Phi) = 0, \tag{4.22}$$

$$R\frac{d}{dR}\left(\Psi' + \frac{\Psi}{R}\right) = \frac{1 - R^2}{2} + R\Phi + \frac{1}{2}\Phi^2. \tag{4.23}$$

Matching the solution of this problem with the outer solution is complicated. Instead, we have been able to patch the solution so that $\Delta\zeta$ and $\Delta\chi$ coincide with their values calculated using (4.17) at $r = \delta_1$. Let us consider $\Phi \ll R$. Ignoring Φ on the right hand side of (4.23), we find

$$\Psi = \frac{R}{4}\ln R - \frac{R^3}{16}, \quad \text{satisfying } \left(\Psi' + \frac{\Psi}{R}\right)\Big|_{R=1} = 0. \tag{4.24}$$

Similarly, ignoring Φ on the right hand side of (4.22), we find

$$\Phi = \frac{R}{8}\left[R^2\ln R - R^2 - \frac{R^4}{3} + 1\right], \text{ satisfying } \left(\Phi' + \frac{\Phi}{R}\right)\Big|_{R=1} = -1, \tag{4.25}$$

from the outer solution, provided

$$\delta_1 = 4\sqrt{\epsilon} = \frac{4}{3\kappa\sqrt{2k}}. \tag{4.26}$$

Using scaling Table 3.1 we can conclude that $\delta_1 \sim h$. Thus the radius of the smooth solution near the cone tip is proportional to thickness, similar to the case of crumpling paper, as noted in Audoly and Pomeau (2010). As the thickness h is small, the corner layer at the tip of the cone is thinner than the boundary layer at its outer rim, whose size is proportional to $h^{1/2}$. The approximate values of $\Delta\zeta$ and $\Delta\chi$ for the corner layer are

$$\begin{aligned} \Delta\zeta &= \sqrt{2k}\left(\phi' + \frac{\phi}{r}\right) \approx \frac{3k\kappa}{2}\left(1 + R^2 \ln R - \frac{R^2}{2} + \frac{1-R^4}{8}\right), \\ \Delta\chi &= 2k\left(\psi' + \frac{\psi}{r}\right) \approx k\left(\ln R + \frac{1-R^2}{2}\right). \end{aligned} \tag{4.27}$$

We have plotted these expressions with $R = r/\delta_1 < 1$, where δ_1 given by (4.26), patched with the cone solution (4.17) for different γ in Figure 4.4. Despite our rough patching, the approximation captures the behavior of the numerical solution.

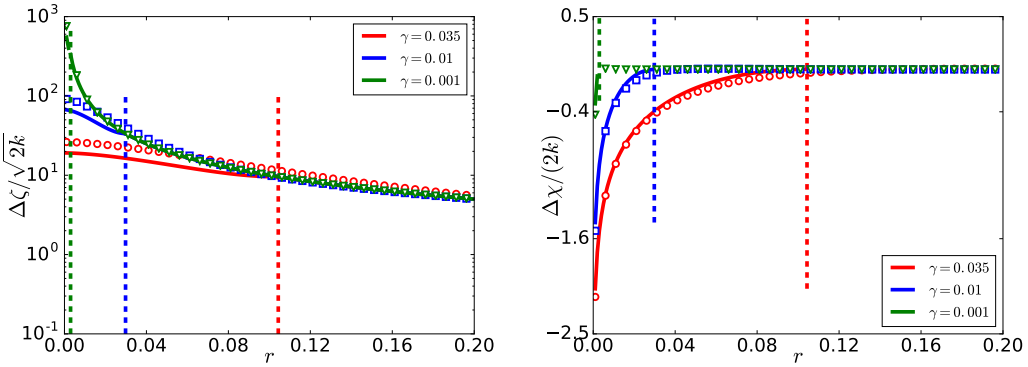

(a) (b)

Figure 4.4: Profiles of (a) scaled $\Delta\zeta/\sqrt{2k} = \phi_{,r} + \phi/r$, and (b) scaled $\Delta\chi/(2k) = \psi_{,r} + \psi/r$ in the corner layer for different values of γ. Markers correspond to numerical solution of the full 1D problem (4.20), dashed vertical lines mark the value of δ_1 given by (4.26). Solid lines correspond to the approximation obtaining by patching (4.17) and (4.27) at the radius δ_1.

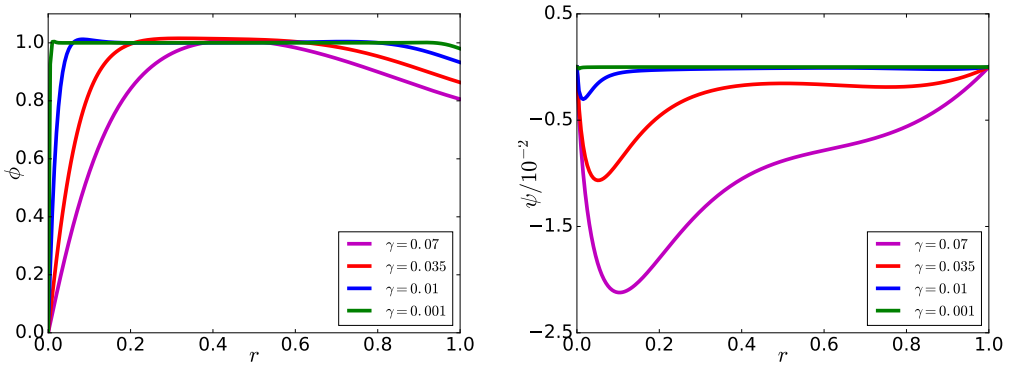

(a) (b)

Figure 4.5: Profiles of (a) ϕ, and (b) ψ for 10% radial growth and different values of $\gamma = h/L$.

4.3.3 Numerical solution

For specified values, we solve the system (4.20) numerically by a second order finite-difference scheme and the Newton-Raphson method to deal with nonlinearity. The boundary conditions are $\Delta\zeta = 0$, $\chi_{,r} = 0$ at $r = 1$, and $\chi_{,r} = \zeta_{,r} = 0$ (symmetry condition) at $r = 0$. For 10% radial growth and $\kappa = 1$, we have $k = 0.1/\gamma^2$. Figure 4.5 shows numerical results for different values of γ. For extremely thin films ($\gamma = 0.001$), ϕ coincides with the cone (4.13) on a quite large interval and the corner layer is very narrow. As γ increases, the plateau shrinks and it disappears for $\gamma > 0.01$. The corner layer and the boundary layer become larger and merge without forming a plateau. The behavior of the Airy potential is similar: for thin films ($\gamma \leq 0.01$) the potential and consequently the stress is zero on a quite large interval but for $\gamma > 0.01$ there are non-zero stresses. It is also interesting to note that, according to (4.24), the stretching stress $\sigma_{rr} = \chi_{,r}/r \propto \psi/r$ goes to infinity at $r = 0$ although the deformation energy is always bounded.

Chapter 5

Weak formulation

The previous chapter shows that solving equations (3.40)-(3.41) can be quite challenging even in a simple case. Troubles arise due to high order of equations, their nonlinearity with respect to ζ and the Gaussian curvature Ψ, which is a combination of second derivatives of the growth tensor components. The last point is crucial for numerical methods: if the growth tensor is not smooth, it will be hard to approximate function Ψ numerically (in our example we had a Dirac delta-function). However the Gaussian curvature contains plenty of information about final wrinkle patterns and therefore should be approximated well. In order to avoid errors related to numerical differentiation, we will reformulate the problem (3.40)-(3.41) with boundary conditions (3.28) in weak form. For simple case of equations (3.43)-(3.44) we provided weak form in paper Iakunin and Bonilla (2018). Here we repeat that derivation and generalized it for equations (3.40)-(3.41).

Before considering weak formulations we introduce a few definition to specify the notation, following by Brezis (2010).

Definition 1. *We will call $L^p(\Omega)$, $1 \leq p < \infty$, $\Omega \subset \mathbb{R}^2$ a vector space of measurable functions $u(x, y)$ such that Lebesgue integral $\int_\Omega |u(x, y)|^p dxdy < \infty$. The norm in this space we can define as*

$$\|u\|_{L^p(\Omega)} = \left(\int_\Omega |u(x, y)|^p \; dx \; dy \right)^{1/p}.$$

Note that strictly speaking $u \in L^p(\Omega)$ are not functions but classes of functions equal almost everywhere.

Definition 2. *The Sobolev space $W^{1,p}(\Omega)$ is a vector space of functions $u \in L^p(\Omega)$ for which functions $g_1 \in L^p(\Omega)$ and $g_2 \in L^p(\Omega)$ exist*

such that

$$\int_\Omega \frac{\partial \varphi}{\partial x} u \; dx \; dy = -\int_\Omega \varphi g_1 \; dx \; dy,$$
$$\int_\Omega \frac{\partial \varphi}{\partial y} u \; dx \; dy = -\int_\Omega \varphi g_2 \; dx \; dy,$$

for any smooth function with compact support $\varphi \in C_c^1(\Omega)$. *These* g_1 *and* g_2 *called* ***generalized partial derivative*** *of* u *respect to* x *and* y *respectively.*

Definition 3. *The Sobolev space* $W^{k,p}(\Omega)$ *where* $k \geq 2$ *and* $k \in \mathbb{N}$ *is a vector space of functions* $u \in W^{k-1,p}(\Omega)$ *which have all generalized derivatives* $\frac{\partial u}{\partial x}$ *and* $\frac{\partial u}{\partial y}$ *belonged to* $W^{k-1,p}(\Omega)$. *Norm in this space is given by the formula:*

$$\|u\|_{W^{k,p}(\Omega)} = \|u\|_{k,p,\Omega} = \left(\sum_{0 \leq |\alpha| \leq k} \|\partial^\alpha u\|^p_{L^p(\Omega,\mathbb{R}^n)} \right)^{1/p},$$

where $\alpha = (\alpha_1, \alpha_2)$ *with* $\alpha_i \geq 0$ *is a multi-index,* $|\alpha| = \sum_{i=1}^2 \alpha_i$ *and* $\partial^\alpha = \frac{\partial^{\alpha_1}}{\partial x^{\alpha_1}} \frac{\partial^{\alpha_n}}{\partial y^{\alpha_n}}$. *We will also use the seminorm of the* l*-th derivatives:*

$$|u|_{W^{l,p}(\Omega)} = |u|_{l,p,\Omega} = \left(\sum_{|\alpha|=l} \|\partial_\alpha u\|^p_{L^p(\Omega)} \right)^{1/p}.$$

Definition 4. *We will call* $W_0^{k,p}(\Omega)$ *the closure by the norm of* $W^{k,p}(\Omega)$ *of infinitely smooth functions with compact supports* $C_c^\infty(\Omega)$. *This space is a subspace of* $W^{k,p}(\Omega)$. *If* $k = 1$, *the seminorm of the first derivatives in* $W^{1,p}(\Omega)$ *will be a norm in* $W_0^{1,p}(\Omega)$ *according to Poincaré inequality.*

The deformation of the film can be described in terms of different variables such as deflection, in-plane displacements, Airy potential, curvatures, etc. Thus the FvKEs system has a few different weak formulations. Here we discuss most common formulation for the simplest case of growth of homogeneous plate in absence of vertical growth that is $g_{13} = g_{23} = 0$. We assume that the film is free on the boundary therefore we have natural boundary conditions (3.28). In this case the stationary equations for scaled variables are:

$$\frac{1}{18\kappa^2}\Delta^2 \zeta - \nabla \cdot \left(\boldsymbol{\sigma}^{(0)} \cdot \nabla \zeta \right) + \frac{2(1-\nu)}{\kappa^2(1-2\nu)} \beta \zeta = 0 \text{ in } \Omega, \tag{5.1}$$
$$\nabla \cdot \boldsymbol{\sigma}^{(0)} + \gamma^2 \beta \mathbf{u} = 0 \text{ in } \Omega. \tag{5.2}$$

The most basic and classical weak form can be found in paper of Lewicka et al. (2011). The formulation is respect to three unknown functions: 2D vector of in-plane displacements $\mathbf{u}$ belonging to $[W^{1,2}(\Omega)]^2$ and vertical deflection ζ which belongs to $W^{2,2}(\Omega)$. In order to obtain weak form we multiply first equation by test function η from $W^{2,2}(\Omega)$ and second by vector function $\mathbf{v}$ from $[W^{1,2}(\Omega)]^2$ and integrate over the domain Ω:

$$\int_\Omega \Bigg(\frac{1}{18\kappa^2} \Big(\Delta\zeta\Delta\eta + \frac{1}{2}[\zeta,\eta] \Big) + \boldsymbol{\sigma}^{(0)} : \frac{\nabla\zeta\otimes\nabla\eta + \nabla\eta\otimes\nabla\zeta}{2} + \frac{2(1-\nu)}{(1-2\nu)\kappa^2}\beta\zeta\eta \Bigg) dxdy = 0, \quad (5.3)$$

$$\int_\Omega \left(\boldsymbol{\sigma}^0 : \frac{\nabla\mathbf{v} + (\nabla\mathbf{v})^T}{2} + \beta\gamma^2 \mathbf{u}\cdot\mathbf{v} \right) dxdy = 0. \quad (5.4)$$

Weak formulation reads find $\zeta \in W^{2,2}(\Omega)$ and $\mathbf{u} \in [W^{1,2}(\Omega)]^2$ such that equation (5.3) - (5.4) holds true for any $\eta \in W^{2,2}(\Omega)$ and $\mathbf{v} \in [W^{1,2}(\Omega)]^2$. If we suppose that $\beta = 0$ than this weak form can be obtained from variation of total mechanical energy:

$$\int_\Omega \Bigg(\frac{1}{18\kappa^2} \Big((\Delta\zeta)^2 + \frac{1}{2}[\zeta,\zeta] \Big) + \boldsymbol{\sigma}^{(0)} : (\nabla\mathbf{v} + \nabla\zeta\otimes\nabla\zeta - \mathbf{g})_S \Bigg) dxdy \to \min, \quad (5.5)$$

where A_S is symmetric part of tensor A that is $A_S = \frac{1}{2}(A + A^T)$. Since the weak formulation (5.3)-(5.4) is naturally derived from minimization of mechanical energy it can be easily generalized for cases of external forces or interaction with the substratum. However this weak form explicitly requires the deflection to be twice differentiable that leads to difficulties in numerical methods.

If we can neglect stretching forces from substratum then the equation (5.2) turns into $\nabla\cdot\boldsymbol{\sigma}^{(0)} = 0$ and can be solved using Airy potential χ. Thus the system (5.1)-(5.2) can be written as

$$\frac{1}{18\kappa^2}\Delta^2\zeta - [\chi,\zeta] + \frac{2(1-\nu)}{(1-2\nu)\kappa^2}\beta\zeta = 0, \quad (5.6)$$

$$\Delta^2\chi + [\zeta,\zeta] - \Psi = 0. \quad (5.7)$$

Weak formulation for this case can be found in paper of Kücken and Newell (2005). We suppose that both unknown functions: deflection $\zeta \in W^{2,2}(\Omega)$

and Airy potential $\chi \in W_0^{2,2}(\Omega) = \{\chi \in W^{2,2}(\Omega) \mid \chi = \frac{\partial \chi}{\partial n} = 0 \text{ on } \partial\Omega\}$ are twice differentiable in general sense. Thus we multiply by test functions η and Φ and integrate to obtain the integral equations:

$$\int_\Omega \left(\frac{1}{18\kappa^2} \left(\Delta\zeta\Delta\eta + \frac{1}{2}[\zeta,\eta] \right) + \frac{2(1-\nu)}{(1-2\nu)\kappa^2}\beta\zeta\eta \right.$$
$$\left. + \chi_{,yy}\zeta_{,x}\eta_{,x} - \chi_{,xy}\frac{\zeta_{,x}\eta_{,y} + \zeta_{,y}\eta_{,x}}{2} + \chi_{,xx}\zeta_{,y}\eta_{,y} \right) dxdy = 0, \tag{5.8}$$

$$\int_\Omega \left(\Delta\chi\Delta\Phi - \frac{3}{2}[\chi,\Phi] + \Phi_{,yy}\left(\frac{\zeta_{,x}^2}{2} - g_{11}\right) \right.$$
$$\left. - \Phi_{,xy}\frac{\zeta_{,x}\zeta_{,y} - g_{12} - g_{21}}{2} + \Phi_{,xx}\left(\frac{\zeta_{,y}^2}{2} - g_{22}\right) \right) dxdy = 0. \tag{5.9}$$

The weak form reads: find $\zeta \in W^{2,2}(\Omega)$ and $\chi \in W^{2,2}(\Omega)$ such that (5.8)-(5.9) holds true for any $\eta \in W^{2,2}(\Omega)$ and $\Phi \in W_0^{2,2}(\Omega)$. Using Airy potential we reduce number of unknown to only 2 but both of them, should be smooth. Furthermore the weak formulation (5.8)-(5.9) comes from minimax variational problem

$$\min_{\zeta \in W^{2,2}(\Omega)} \max_{\chi \in W_0^{2,2}(\Omega)} J(\zeta,\chi),$$
$$J(\zeta,\chi) = \int_\Omega \left[\frac{1}{18\kappa^2}\left((\Delta\zeta)^2 + \frac{1}{2}[\zeta,\zeta] \right) - \left((\Delta\chi)^2 - \frac{3}{2}[\chi,\chi] \right) + \frac{2(1-\nu)}{(1-2\nu)\kappa^2}\beta\zeta^2 \right.$$
$$\left. + \chi_{,yy}\left(\frac{\zeta_{,x}^2}{2} - g_{11}\right) - \chi_{,xy}\frac{\zeta_{,x}\zeta_{,y} - g_{12} - g_{21}}{2} + \chi_{,xx}\left(\frac{\zeta_{,y}^2}{2} - g_{22}\right) \right] dxdy,$$

which is harder to solve numerically.

In this chapter we will use Airy potential weak formulation following Kücken and Newell (2005) when stretching forces are neglectable, as we did in paper Iakunin and Bonilla (2018), and usual weak formulation from Lewicka et al. (2011) in general case. We will show that in both cases we can reduce number of variables to vertical deflection only and rewrite variational form as pure minimization. Particularly it is highly beneficial for Airy potential form since minimization problem is much simpler than minimax.

5.1 Weak formulation for Airy potential case

We start the derivation of weak formulation from a particular case when the second equation in system (3.43)-(3.44) can be solved using Airy potential.

In this case equations have similar form and the derivation is much simpler. Furthermore from final result it is easier to see the mechanism of wrinkles formation. The weak from for general case we be derived afterwards.

We will consider a minimax problem:

$$\min_{\zeta\in V}\max_{\chi\in H} J(\zeta,\chi). \tag{5.10}$$

Here ζ and χ are the vertical deflection and the Airy potential, respectively, V and H are functional spaces for ζ and χ, respectively, and $J(\zeta,\chi)$ is the target functional. In the optimal point, $J(\zeta,\chi)$ equals the energy of the system. We will show that the maximum problem $\max_{\chi\in H} J(\zeta,\chi)$ has a unique solution $\chi_0(\zeta)$ that, inserted into (5.10), transforms it into a minimum problem: $\min_{\zeta\in V} J(\zeta,\chi_0(\zeta))$. After this transformation, we have a simpler minimization problem.

Let us figure out to which spaces V and H and which norms should we choose.

- The points at the biofilm edge are free and, provided it is smooth enough, ζ satisfies the boundary conditions (3.46). To obtain the elastic strain tensor (3.16), ζ has to be twice differentiable. Therefore we choose V as a Sobolev space $W^{2,2}(\Omega)$ endowed with the seminorm related to the bending energy.

- The Airy potential χ is fixed on the boundary and has to be twice differentiable to produce the stress given by (3.42). We will say that

  $$H=\left\{\Phi\in W_0^{2,2}(\Omega)\mid \Phi_x,\ \Phi_y\in W_0^{1,2}(\Omega)\right\}. \tag{5.11}$$

  This space is endowed with the norm related to the stretching energy. The seminorm related to derivatives of order two,

  $$|\Phi|_{2,2,\Omega}=\left(\sum_{\alpha\in\{x,y\}}\sum_{\beta\in\{x,y\}}\|\Phi_{\alpha\beta}\|^2_{L^2(\Omega)}\right)^{1/2}, \tag{5.12}$$

  is also a norm of this space.

To obtain the weak formulation we multiply (3.43) by any test deflection $\eta\in V$ and (3.44) by any test potential $\Phi\in H$. Integrating both equations gives:

$$\int_\Omega\left[\frac{1}{\kappa^2}\left(\Delta(D\Delta\zeta)-[D,\zeta]\right)-2[\chi,\zeta]+\frac{2(1-\nu)\beta}{(1-2\nu)\kappa^2}\zeta\right]\eta dxdy=0, \tag{5.13}$$

$$\int_\Omega\left[\Delta\left(\frac{1}{Eh}\Delta\chi\right)-3\left[\frac{1}{Eh},\chi\right]+[\zeta,\zeta]-\Psi\right]\Phi dxdy=0. \tag{5.14}$$

Let us now consider different terms in these equations thereby finding the functional $J(\zeta,\chi)$ whose variation yields the weak formulation:

- The first two terms in (5.13) come from the variation of the bending energy:

$$\int_\Omega (\Delta(D\Delta\zeta)-[D,\zeta])\eta\ dxdy$$
$$=\int_\Omega \frac{D}{2}\begin{pmatrix}2\zeta_{,xx}+\zeta_{,yy} & \zeta_{,xy}\\ \zeta_{,xy} & 2\zeta_{,yy}+\zeta_{,xx}\end{pmatrix}:\begin{pmatrix}\eta_{,xx} & \eta_{,xy}\\ \eta_{,xy} & \eta_{,yy}\end{pmatrix}dxdy$$
$$=\int_\Omega \sigma^{(1)}(\zeta):\varepsilon^{(1)}(\eta)dxdy=a_{bend}(\zeta,\eta). \quad (5.15)$$

  The bilinear form $a_{bend}(\zeta,\eta)$ provides the second derivative seminorm for V (seminorm because ζ is free on the boundary):

$$|\zeta|_V^2 = a_{bend}(\zeta,\zeta). \quad (5.16)$$

- Analogously the first term in (5.14) comes from the variation of stretching energy:

$$\int_\Omega \left(\Delta\left(\frac{1}{Eh}\Delta\chi\right)-3\left[\frac{1}{Eh},\chi\right]\right)\Phi\ dxdy$$
$$=\int_\Omega \frac{1}{hE}\begin{pmatrix}\chi_{,yy} & -\chi_{,xy}\\ -\chi_{,xy} & \chi_{,xx}\end{pmatrix}:\begin{pmatrix}\Phi_{,yy}-\frac{\Phi_{,xx}}{2} & -\frac{3}{2}\Phi_{,xy}\\ -\frac{3}{2}\Phi_{,xy} & \Phi_{,xx}-\frac{\Phi_{,yy}}{2}\end{pmatrix}dxdy$$
$$=\int_\Omega \sigma^{(0)}(\chi):\varepsilon^{(0)}(\Phi)=a_{stretch}(\chi,\Phi)\ dx\ dy. \quad (5.17)$$

  The bilinear form $a_{stretch}(\chi,\Phi)$ provides the energy norm for the space H (it is a norm because χ and its first derivatives are fixed on the boundary):

$$\|\chi\|_H^2 = a_{stretch}(\chi,\chi). \quad (5.18)$$

- Let us consider the brackets $[\cdot,\cdot]$ defined in (3.26). We note the following property:

$$\int_\Omega [\zeta,\chi]\,v\ dx\ dy=\frac{1}{2}\int_\Omega \nabla\cdot\left[\begin{pmatrix}\chi_{,yy} & -\chi_{,xy}\\ -\chi_{,xy} & \chi_{,xx}\end{pmatrix}\nabla\zeta\right]v\ dxdy$$
$$=-\frac{1}{2}\int_\Omega \nabla\zeta\cdot\begin{pmatrix}\chi_{,yy} & -\chi_{,xy}\\ -\chi_{,xy} & \chi_{,xx}\end{pmatrix}\cdot\nabla v\ dx\ dy$$
$$=\frac{1}{2}\int_\Omega \nabla\cdot\left[\begin{pmatrix}\chi_{,yy} & -\chi_{,xy}\\ -\chi_{,xy} & \chi_{,xx}\end{pmatrix}\nabla v\right]\zeta\ dxdy=\int_\Omega [v,\chi]\,\zeta\ dxdy. \quad (5.19)$$

In the same way we obtain

$$\int_\Omega [\zeta,\chi]v dxdy = \int_\Omega [\chi,v]\zeta dxdy = \int_\Omega [v,\zeta]\chi dxdy = \int_\Omega [\zeta,v]\chi dxdy. \quad (5.20)$$

This property allows us to conclude that terms $[\chi,\zeta]$ and $[\zeta,\zeta]$ in (5.13) and (5.14) come from a variation of the same term in the functional $J(\zeta,\chi)$:

$$\frac{1}{2}\int_\Omega \nabla\zeta\cdot\begin{pmatrix}\chi_{,yy} & -\chi_{,xy}\\ -\chi_{,xy} & \chi_{,xx}\end{pmatrix}\cdot\nabla\zeta dxdy = \frac{1}{2}\int_\Omega \begin{pmatrix}\zeta_{,x}^2 & \zeta_{,x}\zeta_{,y}\\ \zeta_{,x}\zeta_{,y} & \zeta_{,y}^2\end{pmatrix} : \sigma^{(0)} dxdy. \quad (5.21)$$

This is the nonlinear part of the stretching strain in the absence of growth.

- The last term in (5.13) corresponds to the L^2-norm of ζ.
- The last term in (5.14) comes from a linear functional. However $\Phi \in H$ is completely described by its second derivatives and, after two integration by parts, we obtain:

$$\int_\Omega \Psi\Phi \; dx \; dy = \int_\Omega \begin{pmatrix} g_{11}\\ g_{22}\\ g_{12}+g_{21}\end{pmatrix}^T \begin{pmatrix}\Phi_{yy}\\ \Phi_{xx}\\ -\Phi_{xy}\end{pmatrix} dx \; dy. \quad (5.22)$$

Thus we do not need derivatives of growth anymore. Combining (5.21) and (5.22), we almost get the stretching energy:

$$L(\zeta)\chi = \int_\Omega \begin{pmatrix} \zeta_{,x}^2/2 - g_{11}\\ \zeta_{,y}^2/2 - g_{22}\\ \zeta_{,x}\zeta_y - g_{12} - g_{21}\end{pmatrix}^T \begin{pmatrix}\chi_{,yy}\\ \chi_{,xx}\\ -\chi_{,xy}\end{pmatrix} dx \; dy. \quad (5.23)$$

Adding all the contributions listed above, we obtain the target functional $J(\zeta,\chi)$:

$$J(\zeta,\chi) = \frac{1}{2\kappa^2}|\zeta|_V^2 - \frac{1}{2}\|\chi\|_H^2 + L(\zeta)\chi + \frac{\beta(1-\nu)}{(1-2\nu)\kappa^2}\|\zeta\|_{L^2(\Omega)}^2. \quad (5.24)$$

Here the seminorm $|\zeta|_V$ is given by (5.16) and the norm $\|\chi\|_H$ by (5.18). The functional $L(\zeta)\chi$ comes from (5.23) and is linear respect to the potential χ

but nonlinear respect to the deflection ζ. Sum of the first and the last terms for $\beta > 0$ gives us a norm for the space V:

$$\|\zeta\|^2_{V,\beta,2} = |\zeta|^2_V + \frac{2\beta(1-\nu)}{(1-2\nu)} \|\zeta\|^2_{L^2(\Omega)}. \tag{5.25}$$

The functional $J(\zeta, \chi)$ should be maximized respect to χ and minimized respect to ζ so we have the following variational problem:

$$\min_{\zeta \in V} \max_{\chi \in H} J(\zeta, \chi). \tag{5.26}$$

The weak form of (3.43)-(3.44) follows from (5.13)-(5.14): Find $\zeta \in V$ and $\chi \in H$ satisfying

$$\begin{aligned} &\frac{1}{\kappa^2} a_{bend}(\zeta, v) + 2\frac{\beta(1-\nu)}{(1-2\nu)\kappa^2}(\zeta, v)_{L^2(\Omega)} \\ &\quad + \int_\Omega \nabla\zeta \cdot \begin{pmatrix} \chi_{,yy} & -\chi_{,xy} \\ -\chi_{,xy} & \chi_{,xx} \end{pmatrix} \cdot \nabla v dxdy = 0, \forall v \in V; \qquad (5.27) \\ &-\frac{1}{Eh} a_{stretch}(\chi, \Phi) + L(\zeta)\Phi = 0, \forall \Phi \in H; \qquad (5.28) \end{aligned}$$

where $(\zeta, v)_{L^2(\Omega)}$ denotes scalar multiplication in $L^2(\Omega)$.

5.1.1 Reduction to weak form depending only of vertical displacements

The minimax problem (5.26) where J is given by (5.24) is quite hard to solve. However we note that the maximum of $J(\zeta, \chi)$ with respect to χ for fixed ζ can be found easily. Let us first analyze the linear functional $L(\zeta)\chi$. It is not only linear but it is also bounded in H. This can be proven by applying Hölder and triangle inequalities multiple times:

$$\begin{aligned} \|L(\zeta)\|^2_{H^*} &\leq c \left(\int_\Omega \left\| \begin{pmatrix} \zeta^2_{,x}/2 - g_{11} \\ \zeta^2_{,y}/2 - g_{22} \\ \zeta_{,x}\zeta_{,y} - g_{12} - g_{21} \end{pmatrix} \right\|^2 dxdy \right) \\ &\leq C \left(|\zeta|^2_{1,4,\Omega} + \sum_{1 \leq i,j \leq 2} \|g_{ij}\|^2_{L^2(\Omega)} \right). \end{aligned} \tag{5.29}$$

Here H^* represents the dual space for H, the L^4-norm of the first derivatives of ζ exists due to the Rellich-Kondrashov embedding theorem (see Brezis (2010)). Formula (5.29) gives just an upper bound for the norm but not a

good estimation. For example if film is flat ($\zeta = 0$) and growth is isotropic and homogeneous ($\mathbf{g} = g\mathbf{I}$) the functional $L(0)$ is zero:

$$L(0)\chi = -g \int_{\Omega} \Delta\chi dxdy = 0, \forall\chi \in H,$$

whereas (5.29) gives upper boundary $\sqrt{C}\|\mathbf{g}\|_{L^2(\Omega)}$ which of course is correct by quite far from the exact value.

We can note that the space H becomes a Hilbert space if we endow it with a scalar product given the by stretching energy bilinear form (5.17):

$$(\chi, \Phi)_H = a_{stretch}(\chi, \Phi). \tag{5.30}$$

For these functional spaces Riesz's theorem holds:

Theorem 5.1.1. *Every bounded linear functional L on a Hilbert space H can be represented in terms of scalar multiplication, namely,*

$$(\chi_L, \Phi)_H = L\Phi \quad \forall\ \Phi \in H, \tag{5.31}$$

where χ_L depends on L, is uniquely determined by L and has norm

$$\|\chi_L\|_H \ = \ \|L\|_{H^*}.$$

See Kreyszig (1978) for the proof.

Now let us consider the maximization part of the problem (5.26):

$$\max_{\chi \in H} \left\{ J_{max}(\chi) = -\frac{1}{2}\|\chi\|_H^2 + L(\zeta)\chi \right\}. \tag{5.32}$$

Here we have included only terms that depend on χ because only they influence the maximization. Assume that χ_0 provides the maximum of the functional in (5.32). Then for any $\Phi \in H$ we have:

$$J_{max}(\chi_0) - J_{max}(\chi_0 + \Phi) \geq 0 \implies (\chi_0, \Phi)_H + L(\zeta)\Phi + \frac{1}{2}\|\Phi\|_H^2 \geq 0. \tag{5.33}$$

The last term is always positive but the first two can change their sign depending on Φ. Thus the sum of the first two terms in (5.33) must be zero in order to satisfy the optimum condition (5.33) for all Φ:

$$(\chi_0, \Phi)_H = L(\zeta)\Phi \ \forall\Phi \in H. \tag{5.34}$$

We can see that the formula (5.34) looks very similar to the formula (5.31). Then we can apply the Riesz theorem thereby getting:

1. The optimum point χ_0 exists and is unique;

2. $\|\chi_0\|_H = \|L(\zeta)\|_{H^*} = L(\zeta)\chi_0$.

Using these results, we conclude that

$$J_{max}(\chi_0) = \frac{1}{2}\|L(\zeta)\|^2_{H^*}. \tag{5.35}$$

After substituting (5.35) into (5.26), we obtain a pure minimization problem:

$$\min_{\zeta \in V} \left\{ J_{min}(\zeta) = \frac{1}{2\kappa^2}|\zeta|^2_V + \frac{1}{2}\|L(\zeta)\|^2_{H^*} + \frac{\beta(1-\nu)}{\kappa^2(1-2\nu)}\|\zeta\|^2_{L^2(\Omega)} \right\} \tag{5.36}$$

The functional in (5.36) contains three parts:

1. Seminorm of second derivatives of the deflection. This part corresponds to the bending energy and is small if the film is thin.

2. Norm of the functional $L(\zeta)$, which corresponds to geometrical transformation.

3. The last term is the effect of the viscoelastic layer that is supposed to cancel large deflections (since they lead to large deformations of the layer).

After all these simplifications, the weak form (5.27)-(5.28) becomes: Find ζ from V which satisfies

$$\frac{1}{\kappa^2}a_{bend}(\zeta, v) + 2\frac{\beta(1-\nu)}{(1-2\nu)\kappa^2}(\zeta, v)_{L^2(\Omega)} + \int_\Omega \nabla\zeta \cdot \begin{pmatrix} \chi_{0,yy}(\zeta) & -\chi_{0,xy}(\zeta) \\ -\chi_{0,xy}(\zeta) & \chi_{0,xx}(\zeta) \end{pmatrix} \cdot \nabla v dxdy = 0, \forall v \in V, \tag{5.37}$$

where $\chi_0(\zeta)$ is solution of problem (5.32) for a fixed ζ.

5.1.2 Analysis of the cone solution using the weak formulation

The derived weak formulation can be used to perform a different analysis of the problem from that in chapter 4. As we neglect the interaction with the viscoelastic layer, the functional (5.24) becomes

$$J(\zeta, \chi) = \frac{1}{2\kappa^2}|\zeta|^2_V + \frac{1}{2}\|L(\zeta)\|^2_{H^*}. \tag{5.38}$$

Here the second term corresponds to the geometrical transformation and the first one representing bending energy can be neglected for a sufficiently thin film.

Provided the components of the growth tensor are twice differentiable, the linear functional $L(\zeta)\chi$ can be rewritten as:

$$L(\zeta)\chi = \int_\Omega \left(\frac{1}{2}[\zeta,\zeta] - \Psi\right) \chi \; dx \; dy = \int_\Omega \left(\zeta_{,xx}\zeta_{,yy} - \zeta_{,xy}^2 - \Psi\right) \chi \; dx \; dy, \quad (5.39)$$

where Ψ is given by formula (3.45). Thus, if ζ satisfies the MAE

$$\zeta_{,xx}\zeta_{,yy} - \zeta_{,xy}^2 - \Psi = 0$$

almost everywhere, the functional $L(\zeta)$ is zero. For thin films, this implies that $J(\zeta,\chi)$ is very small. Now the MAE should be satisfied almost everywhere, which allows us to consider new shapes such as, for example, a broken cone representing a wrinkle:

$$\zeta(r,\theta) = \begin{cases} -\sqrt{g_r}(r-0.5), r < 0.5, \\ \sqrt{g_r}(r-0.5), r \geq 0.5 \end{cases} \quad (5.40)$$

It is easy to see that the cone can be broken any number of times. Therefore the problem of pure geometrical transformation (minimization of norm of functional $L(\zeta)$) is ill-posed and has infinitely many solutions. Fortunately the other term in (5.38), $|\zeta|_V^2$, regularizes the problem. Indeed, each break given by (5.40) leads to a discontinuity of the first derivatives and, consequently, to large values of the second derivatives of ζ, which have an immediate effect on $|\zeta|_V^2$. In other words, due to the regularizing bending energy, we should choose the smoothest solution among all the geometrical solutions. Nevertheless the smaller the first term of (5.38) is (κ is large), the more likely it is that a solution with large number of wrinkles can become a local minimum of energy.

What will happen if we add an agar layer? In our functional the interaction with the substratum is represented as L^2 norm of the deflection. Thus solutions with large ζ will be penalized in the presence of agar. Solutions like the cone will be penalized by large values whereas solutions with wrinkles (broken cones) will have smaller deflections and need relatively small corrections to their energy. Thus for films on agar substrata, we can expect that the frequency of wrinkles increases and their amplitude decreases.

To conclude this section, we summarize how the weak formulation produces a solution:

1. The general shape of the solution is generated by the problem of minimization of $\|L(\zeta)\|$. It represents a pure geometrical transformation and it may be satisfied by an infinite number of possible shapes. The frequency and amplitude of wrinkles in these shapes are related due to the geometrical nonlinearity of the process.

2. The regularization terms that come from the bending energy and the interaction with the viscoelastic layer influence the resulting solution. The norm of the second derivatives of ζ tries to decrease the number of wrinkles and folds whereas the interaction with the viscoelastic layer tries to decrease the amplitude.

3. The final solution results from the balance of all these terms.

5.2 Existence of solution

Even though existence, uniqueness, and regularity of solution of FvKEs are quite well studied there is no results for modified FvKEs including internal growth. The main challenge consists in Gaussian curvature Ψ which enforces nonlinearity and makes the system closer to MAE than to biharmonic equation. For the system (3.43)-(3.44) there always is a trivial solution $\zeta = 0$ and $\Delta\left(\frac{1}{Eh}\Delta\chi\right) - 3\left[\chi, \frac{1}{Eh}\right] = \Psi$ which is not stable for large growth and thin films. In order to get rid of this trivial solution we will modify the equation by introducing a right part f:

$$\frac{1}{18\kappa^2}\Delta^2\zeta - [\zeta, \chi] = f, \tag{5.41}$$

$$\Delta^2\chi = -[\zeta, \zeta] + \Psi. \tag{5.42}$$

For $\Psi = 0$ and homogeneous Dirichlet boundary conditions this equations are studied in book of Lions (1969). In that book authors show a basic way to prove existence of solution of FvKEs using operator theory and fixed point theorem. Later this result was generalized to heterogeneous Dirichlet boundary conditions by Ciarlet et al (2001) and to Neumann boundary conditions by Naumann (1974). However in both these papers Ψ is still supposed to be zero. A more general result was obtained by Ciarlet and Gratie (2004) for Marguerre-von Kármán equations which follows from (5.41)-(5.42) if there is a sufficiently smooth deflection θ such that $[\theta, \theta] = \Psi$. In our case it is not always true as it was shown in chapter 4.

In this section we will assume that equation (5.41)-(5.42) holds true in a

bounded domain $\Omega \subset \mathbb{R}^2$ and we suppose the following boundary conditions:

$$2\Delta\zeta - \zeta_{,ij}\tau_i\tau_j = 0, \quad 2\frac{\partial}{\partial n}\Delta\zeta + \frac{\partial}{\partial \tau}\left(\zeta_{,ij}\tau_i n_j\right) = 0, \tag{5.43}$$

$$\chi = \frac{\partial \chi}{\partial n} = 0, \tag{5.44}$$

on $\partial\Omega$. Here τ_i and n_i represent components of tangential and normal vectors to the boundary. In our prove we will follow ideas of Lions (1969); Naumann (1974); Ciarlet and Gratie (2004).

Firstly let us define functional space for which we will prove existence of solution. For Airy potential we will use the similar space

$$H = \left\{ \chi \in W^{2,2}(\Omega) \mid \chi = \frac{\partial \chi}{\partial n} = 0 \text{ on } \partial\Omega \right\}$$

with norm given by (5.18). This space is a Hilbert space with scalar multiplication $(\chi, \Phi)_H = a_{stretch}(\chi, \Phi)$. For deflection we will use a factor space W of V respect to subspace of linear functions $P_1 = \{f(x, y) = ax + by + c\}$. Strictly speaking elements W are not functions but classes ζ of functions η such that $\eta_1, \eta_2 \in \zeta \Leftrightarrow \eta_1 - \eta_2 \in P_1$. For W we can define norm the following way:

$$\|\zeta\|_W = \inf_{\eta \in \zeta} \|\eta\|_V,$$

however it is also possible to prove that the second derivative seminorm given by (5.16) defines a norm in W. Thus the space W equipped with norm (5.16) is also a Hilbert space with scalar multiplication $(\zeta, \eta)_W = a_{bend}(\zeta, \eta)$.

Theorem 5.2.1. *The system* (5.41)-(5.42) *where* $f, \Psi \in W^{-2,2}(\Omega)$ *with boundary conditions* (5.43)-(5.44) *has a weak solution* $(\zeta, \chi) \in W \times H$ *if the norm* $\|\Psi\|_{W^{-2,2}(\Omega)}$ *is small enough.*

1. We define bilinear form $B : W \times W \to H$:

$$\Delta^2 B(\zeta, \eta) = [\zeta, \eta]. \tag{5.45}$$

   Since the equation (5.45) has a unique solution in H (see the previous section) we can conclude that B is well defined. Furthermore this operator is bounded and compact (see Ciarlet (1997) for details):

$$\|B(\zeta, \eta)\|_H \leq C|\zeta|_{1,4}|\eta|_{1,4} \leq c_1\|\zeta\|_W\|\eta\|_W, \tag{5.46}$$

   where $|\cdot|_{1,4}$ is $L^4(\Omega)$ first derivative seminorm.

2. Analogously we can define function χ_0 such that

$$\Delta^2\chi_0 = \Psi, \quad \|\chi_0\|_H \le \|\Psi\|_{W^{-2,2}(\Omega)} \le \|\mathbf{g}\|_{L^2(\Omega)}. \tag{5.47}$$

3. Now we can rewrite system (3.41)-(3.42) in operator form. We define operator $F : W \to W$ by the following way

$$\frac{1}{18\kappa^2}\Delta^2 v = [\zeta, \chi_0 - B(\zeta,\zeta)] + f \Leftrightarrow v = F(\zeta). \tag{5.48}$$

Easy to see that for any fixed $\zeta \in W$ there is only one $v \in W$ (it can be proved from Riesz's theorem similarly to the case of Airy potential in previous section). Operator F is bounded and compact. The first fact can be obtained by multiplication of (5.48) by a test function $w \in W$ and integrating

$$\frac{1}{18\kappa^2}(v,w)_W = (B(\zeta,w),\chi_0)_H - (B(\zeta,w),B(\zeta,\zeta)) + \int_\Omega f w dxdy. \tag{5.49}$$

If we choose $w = v$ then (5.49) turns into

$$\frac{1}{18\kappa^2}\|v\|_W \le C|\zeta|_{1,4}\|\chi_0\|_H + C|\zeta|^3_{1,4} + \|f\|_{W^{-2,2}(\Omega)}, \tag{5.50}$$

that gives an upper bound for the norm of $v = F(\zeta)$. Similarly we can prove compactness of F. Let us choose a sequence $\{\zeta_k\}_{k=1}^\infty \subset W$ which converges weakly to ζ. Since $V = W^{2,2}(\Omega)$ embeds compactly into $W^{1,4}(\Omega)$ (result of Rellich-Kondrachov theorem, see Brezis (2010)) we have that the sequence $\{\zeta_k\}_{k=1}^\infty$ converges strongly to ζ in $W^{1,4}(\Omega)$ that is $|\zeta_k - \zeta|_{1,4} \to 0$ when $k \to \infty$. We can write

$$\frac{1}{18\kappa^2}\Delta^2 v_k = [\zeta_k, \chi_0 - B(\zeta_k,\zeta_k)] + f,$$
$$\frac{1}{18\kappa^2}\Delta^2 v = [\zeta, \chi_0 - B(\zeta,\zeta)] + f,$$

and by substructing second from first we obtain

$$\frac{1}{18\kappa^2}\Delta^2 (v_k - v) = [\zeta_k, \chi_0 - B(\zeta_k,\zeta_k)] - [\zeta, \chi_0 - B(\zeta,\zeta)]. \tag{5.51}$$

If we multiply (5.51) by $v_k - v$ and integrate we obtain an estimation

$$\frac{1}{18\kappa^2}\|v_k - v\|_W \le C \underbrace{|\zeta_k - \zeta|_{1,4}}_{\to 0} \left(\|\chi_0\|_H + |\zeta_k|^2_{1,4} + |\zeta|_{1,4}|\zeta + \zeta_k|_{1,4}\right). \tag{5.52}$$

Formula (5.52) means that v_k goes to v when k goes to infinity that means that $F(\zeta_k) \to F(\zeta)$ strongly in W. *Q.E.D.*

4. Now we consider operator $\zeta - F(\zeta)$ and prove that if $\|\chi_0\|_H$ is small enough we always can choose sphere with radius ρ such that $(\zeta,F(\zeta))_W \leq 0$ on this sphere. Indeed

$$(\zeta, F(\zeta))_W = \|\zeta\|^2_W + 18\kappa^2 \left(-(B(\zeta,\zeta),\chi_0)_H + \|B(\zeta,\zeta)\|^2_H - \int_\Omega f\zeta dxdy \right) \geq \|\zeta\|^2_W (1 - 18\kappa^2 c_1 \|\chi_0\|_H) - 18\kappa^2 \|f\|_{W^{-2,2}(\Omega)} \|\zeta\|_W, \quad (5.53)$$

which is nonnegative if $\|\chi_0\| \leq \frac{1}{18\kappa^2 c_1}$ and $\|\zeta\|_W = \rho \geq 18\kappa^2 \|f\|_{W^{-2,2}(\Omega)}$.

5. We can reduce the operator $\zeta - F(\zeta)$ to finite-dimensional subspaces of W. Let us select a basis $\{w_1, \ldots, w_n\}$ in a subspace $W_n \subset W$ so any function from this subspace can be written $v(x,y) = \sum_{k=1}^n v_k w_k(x,y)$. Then components of the reduction $v = G_n(\zeta)$ of the operator $\zeta - F(\zeta)$ can be calculated as

$$v_k = (\zeta - F(\zeta), w_k)_W, \ k = 1, \ldots, n$$

For finite dimensional operators holds true a variation of Brouwer fixed point theorem given in the book of Lions (1969):

Theorem 5.2.2. *Let $G : \mathbb{R}^n \to \mathbb{R}^n$ such that*

$$(G(x), x) \geq 0,$$

for all x belonging to a sphere with radius ρ, that is $\|x\| = \rho$. Then a point x^* exists such that $\|x^*\| \leq \rho$ and $G(x^*) = 0$.

We can apply this theorem to operator $\zeta - F_n(\zeta)$ defined in space W_n for which holds true (5.53). We obtain thus that for any finite dimensional subspace W_n there is a solution $\zeta_n \in W_n$ of the problem $\zeta = F_n(\zeta)$. We will call this solution finite dimensional approximation.

6. Let us consider a sequence of finite dimensional approximations $\{\zeta_n\}_{n=1}^\infty \subset W$. According to theorem 5.2.2 this sequence is bounded by value ρ and since W is a Hilbert space we can extract a subsequence $\{\zeta_{n_k}\}_{k=1}^\infty$ which converges weakly to ζ. Using the definition of reduced operator we obtain that

$$(\zeta_{n_k} - F(\zeta_{n_k}), \eta)_W = 0, \forall \eta \in W_{n_k}. \quad (5.54)$$

Let us choose arbitrary function $\eta \in W$ and a sequence $\{\eta_k\}_{k=1}^{\infty} \subset W$ which converges to η and $\eta_k \in W_{n_k}$. Now we can rewrite formula (5.54) as

$$(\zeta_{n_k}, \eta_k)_W = (F(\zeta_{n_k}), \eta_k)_W, \forall k \in \mathbb{N}. \tag{5.55}$$

Passing to the limit in (5.55) and using compactness of operator F we obtain that

$$(\zeta, \eta)_W = (F(\zeta), \eta), \forall \eta \in W,$$

since we choose and arbitrary function η. Using compactness of operator $B(\zeta, \eta)$ we can conclude that $\chi = -B(\zeta, \zeta) + \chi_0$ also exists. It means that the pair (ζ, χ) is the solution the system (5.41) -(5.42). *Q.E.D.*

This theorem has a serious disadvantage: it requires Gaussian curvature Ψ to be small. Perhaps one way to get rid of this constrain is to seek a solution in a neighborhood of MAE's solution $[\zeta, \zeta] = \Psi$. The main challenge here consists in that the MAE does not always resolvable in W and that for general Ψ it is not convex.

5.3 Weak form for general case

For general case we cannot use Airy potential to resolve the equation (3.41) and the reduction to only one variable is more complicated however the same idea works out. The deflection should belong to the same space V endowed with the second derivatives seminorm (5.16) and usual L^2 norm. Since the divergence of stress is not zero anymore we have to resolve the second equation in terms of in-plane displacements $\mathbf{u}$ whose components, following to Lewicka et al. (2011), should belong to $W^{1,2}(\Omega)$, so we say $\mathbf{u} \in U = W^{1,2}(\Omega) \times W^{1,2}(\Omega)$. In this new space U we define a first-derivatives seminorm related to stretching energy:

$$a_{disp}(\mathbf{u}, \mathbf{v}) = \int_\Omega \begin{pmatrix} u_{1,x} \\ u_{2,y} \\ (u_{1,y}+u_{2,x})/2 \end{pmatrix}^T K \begin{pmatrix} v_{1,x} \\ v_{2,y} \\ (v_{1,y}+v_{2,x})/2 \end{pmatrix} dxdy, \tag{5.56}$$

$$|\mathbf{u}|_{2,U} = \sqrt{a_{disp}(\mathbf{u}, \mathbf{u})}, \tag{5.57}$$

where K is stiffness matrix:

$$K = \frac{2Eh}{3} \begin{pmatrix} 2 & 1 & 0 \\ 1 & 2 & 0 \\ 0 & 0 & 2 \end{pmatrix}.$$

Functional L^2-norm and L^2 inner product for space U we will write in vector from:

$$(\mathbf{u},\mathbf{v})_{L^2(\Omega)} = (u_1,v_1)_{L^2(\Omega)} + (u_2,v_2)_{L^2(\Omega)}, \quad \|\mathbf{u}\|_{L^2(\Omega)} = \sqrt{(\mathbf{u},\mathbf{u})_{L^2(\Omega)}}.$$

Now we write the variational form of minimization of energy functional:

$$\begin{aligned}
&\min_{\zeta\in V,\mathbf{u}\in U} \mathcal{W}(\zeta,\mathbf{u}) \\
&\mathcal{W} = \beta\left(\frac{2(1-\nu)}{(1-2\nu)\kappa^2}\|\zeta\|^2_{L^2(\Omega)} + \gamma^2\|\mathbf{u}\|^2_{L^2(\Omega)}\right) + \\
&\qquad \frac{1}{\kappa^2}|\zeta|^2_V + \int_\Omega \boldsymbol{\sigma}^{(0)} : \boldsymbol{\varepsilon}^{(0)} dxdy,
\end{aligned} \tag{5.58}$$

where strains and stresses are given by (3.16) and (3.17) respectively. We can note, the the last integral can be divided into bilinear form $a_{disp}(\mathbf{u},\mathbf{u})$, linear functional $L(\zeta)\mathbf{u}$ and nonlinear residual $r(\zeta)$ dependent only on deflection:

$$\int_\Omega \boldsymbol{\sigma}^{(0)} : \boldsymbol{\varepsilon}^{(0)} dxdy = a_{disp}(\mathbf{u},\mathbf{u}) + 2L(\zeta)\mathbf{u} + r(\zeta),$$

$$L(\zeta)\mathbf{u} = \int_\Omega \begin{pmatrix} \zeta_{,x}^2/2 - g_{11} \\ \zeta_{,y}^2/2 - g_{22} \\ \frac{\zeta_{,x}\zeta_{,y} - g_{12} - g_{21}}{2} \end{pmatrix}^T K \begin{pmatrix} u_{1,x} \\ u_{2,y} \\ \frac{u_{1,y}+u_{2,x}}{2} \end{pmatrix} dxdy, \tag{5.59}$$

$$r(\zeta) = \int_\Omega \begin{pmatrix} \zeta_{,x}^2/2 - g_{11} \\ \zeta_{,y}^2/2 - g_{22} \\ \frac{\zeta_{,x}\zeta_{,y} - g_{12} - g_{21}}{2} \end{pmatrix}^T K \begin{pmatrix} \zeta_{,x}^2/2 - g_{11} \\ \zeta_{,y}^2/2 - g_{22} \\ \frac{\zeta_{,x}\zeta_{,y} - g_{12} - g_{21}}{2} \end{pmatrix} dxdy. \tag{5.60}$$

Variation of mechanical energy (5.58) yields the weak form:

$$\begin{aligned}
&\frac{2(1-\nu)\beta}{\kappa^2(1-2\nu)}(\zeta,\eta)_{L^2(\Omega)} + \frac{1}{\kappa^2}a_{bend}(\zeta,\eta) + \\
&\qquad \int_\Omega \boldsymbol{\sigma}^{(0)} : (\nabla\zeta \otimes \nabla\eta)_S \, dxdy = 0, \forall\eta \in V,
\end{aligned} \tag{5.61}$$

$$\beta\gamma^2(\mathbf{u},\mathbf{v})_{L^2(\Omega)} + a_{disp}(\mathbf{u},\mathbf{v}) = -L(\zeta)\mathbf{v}, \forall\mathbf{v} \in U. \tag{5.62}$$

We can solve second equation the same way as we did in previous section. Now functions from space U are not fixed at the boundary and we have to use their values to define norm and scalar multiplication. It can be done the following way:

$$(\mathbf{u},\mathbf{v})_U = \beta\gamma^2(\mathbf{u},\mathbf{v})_{L^2(\Omega)} + a_{disp}(\mathbf{u},\mathbf{v}), \quad \|\mathbf{u}\|_U = \sqrt{(\mathbf{u},\mathbf{u})_U}, \tag{5.63}$$

where $a_{disp}(\mathbf{u}, \mathbf{v})$ is given by (5.56). We can prove that functional $L(\zeta)$ is bounded in U by applying triangle and Hölder inequalities multiple times almost as we did for the case of Airy potential:

$$|L(\zeta)\mathbf{v}| \leq (c_1|\zeta|_{1,4}^4 + c_2\|\mathbf{g}\|_{L^2(\Omega)}^2)\sqrt{a_{disp}(\mathbf{v},\mathbf{v})} \leq (c_1|\zeta|_{1,4}^4 + c_2\|\mathbf{g}\|_{L^2(\Omega)}^2)\|\mathbf{v}\|_U,$$

that implies

$$\|L(\zeta)\|_{U^*} \leq C\left(|\zeta|_{1,4}^2 + \|\mathbf{g}\|_{L^2(\Omega)}^2\right), \tag{5.64}$$

where $|\zeta|_{1,4}$ is L^4-norm of first derivatives of ζ. Even though we have the same estimation as in previous case the behavior of functional alters. It happens due to boundary conditions: in the previous case Airy potential was fixed on the boundary, but now the displacements are free. For example for compatible isotropic homogeneous growth $\mathbf{g} = g\mathbf{I}$, flat film $\zeta = 0$ and homogeneous material instead of zero functional we have

$$L(0)\mathbf{v} = -2g\int_\Omega (v_{1,x} + v_{2,y})\,dxdy = -2g\int_{\partial\Omega} \mathbf{v}\cdot\mathbf{n}\,dxdy. \tag{5.65}$$

It means that now even compatible growth can cause wrinkles.

Using Riesz's theorem we can conclude that equation (5.52) has exactly one weak solution $\mathbf{u}^*$ and $\|\mathbf{u}^*\|_U = -L(\zeta)\mathbf{u}^* = \|L(\zeta)\|_{U^*}$ at that. Adding all contribution into the energy functional (5.58) we obtain a reduced function which depends only in deflection ζ:

$$\begin{aligned}&\min_{\zeta\in V} \mathcal{W}_r(\zeta)\\ &\mathcal{W}_r = \frac{2(1-\nu)\beta}{\kappa^2(1-2\nu)}\|\zeta\|_{L^2(\Omega)}^2 + \frac{1}{\kappa^2}|\zeta|_V^2 - \|L(\zeta)\|_{U^*}^2 + r(\zeta).\end{aligned} \tag{5.66}$$

The obtained functional is not convex however it is always positive since $r(\zeta)$ is upper bound for the norm of functional $L(\zeta)$.

Chapter 6

Numerical method

As we cannot solve the problem (5.36) analytically, we will use a numerical method. Since we deal with a minimization of a functional over a Sobolev space, it is natural to use finite element method (FEM). The idea of FEM is instead of solving variational problem on infinitely dimensional functional space V do it on some finite dimensional subspace V_h. Since all finite dimensional spaces are isomorphic to $\mathbb{R}^n$ the initial problem turns into algebraic one which can be very efficiently solved on a computer. How do we construct the subspace V_h? In FEM we divide Ω into a finite set of small compact subdomains, called elements, and define functions, called shape functions, which are not zero only on a few neigbouring elements. Subspace V_h is nothing but linear space of these function, index h here refers to average size of elements. The fact that shape functions are non zero only in a small region makes basis in V_h almost orthogonal. A rigorous definition of element and shape function can be found in Brenner and Scott (2008). One of advantages of FEM is that it can be applied to any kind of domains Ω. It is quite beneficial for us because biofilms may have very complex shape but we always can approximate them with triangular elements. Another advantage is possibility to use polynomial shape functions which can be easily integrated using Gaussian quadrature.

6.1 Finite element simulation of plate bending

Even though bending of plates is one of the first problems FEM was applied to, solution of this problem still contains various difficulties. The main challenge consists in high regularity of deflection which belongs to $W^{2,2}(\Omega)$ and as a consequence requirement for shape function to be smooth. The simplest

triangular, continuous, smooth, and polynomial element is Argyris element, Braess (2007). This element has 21 degrees of freedom, inside the triangle shape functions define complete space P_5 of polynomials of degree 5, so the full approximation is given by piece-wise 5th order polynomials. In practice usage of Argyrys element leads to numerical difficulties because of large number of unknowns and high degree of polynomials we have to integrate. Last point is crucial for nonlinear problems. Thus Argyris element is not so common in practice and another approaches are used to simulate plate bending.

The first way is to reduce regularity of ζ by introduction of new variables representing curvatures that is go to Reissner-Mindlin theory. This approach is describe in book of Hughes (2000) and is quite efficient for many industrial application where the plate is relatively thick. However for thin film according to Reddy (2003) the Kirchhoff theory is preferable.

Another approach is to use nonconformed elements that is to violate smoothness of approximation and solve problem on V_h which is not subspace of V. Despite that this idea is quite naive it is very efficient in practice Zienkiewicz and Taylor (2005); Reddy (2003). The simplest nonconformed triangular element is Morley element. It has only 6 degrees of freedom, inside the element shape functions define complete space P_2 of second order polynomials, however the full approximation is not even continuous. Nevertheless Morley element is widely used for biharmonic equation. For plate bending it is better to use Zienkiewicz triangle, Zienkiewicz and Taylor (2005); Reddy (2003), because it takes into account physics of the process. We use this element in our simulation and we will discuss it in details in the following subsection.

One more way to simulate plate bending using FEM is to use nonpolynomial elements, for example Clough-Tocher triangle Peker et al (2007). These elements provide continuous and smooth approximation but shape function are piece-wise polynomial inside the element, so we have to use more integration points in Gaussian quadrature.

6.1.1 Zienkiewicz element

Zienkiewicz triangles are relatively simple and commonly used in simulations of plate deformation, Hughes (2000); Zienkiewicz and Taylor (2005). To each node $n \in \{1, 2 \ldots, N\}$, we assign a triplet of shape functions ϕ_{3n-2}, ϕ_{3n-1}, and ϕ_{3n}. These functions are given by cubic 2D polynomials on each element having the node n as one of its vertices and they equal 0 elsewhere in the domain. The shape functions in a triangle element are defined in terms of its barycentric coordinates L_i, $i \in \{1, 2, 3\}$. For each point M inside the

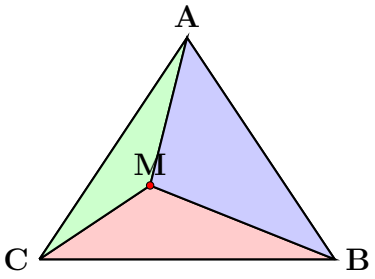

$$L_1 = \frac{S(MBC)}{S(ABC)}$$
$$L_2 = \frac{S(AMC)}{S(ABC)}$$
$$L_3 = \frac{S(ABM)}{S(ABC)}$$

Figure 6.1: L-coordinates of the triangle elements.

triangle ABC, the coordinate L_i is equal to the area of triangle with tip in M and base made by the edge opposite to node i divided by the area of whole triangle (see Figure 6.1). The barycentric coordinates of point M are related to its Cartesian coordinates (x, y) by the formula:

$$\begin{cases} L_1 + L_2 + L_3 = 1, \\ x_1 L_1 + x_2 L_2 + x_3 L_3 = x, \\ y_1 L_1 + y_2 L_2 + y_3 L_3 = y, \end{cases} \tag{6.1}$$

where x_i, y_i are coordinates of i-th vertex. Now the element shape functions are

$$\phi_{3n-2}(L_1, L_2, L_3) = L_i^2(L_j + L_k) + L_i(1 - L_j^2 - L_k^2);$$
$$\phi_{3n-1}(L_1, L_2, L_3) = (x_j - x_i)\left(L_i^2 L_j + \frac{L_i L_j L_k}{2}\right) - (x_i - x_k)\left(L_i^2 L_k + \frac{L_i L_j L_k}{2}\right);$$
$$\phi_{3n}(L_1, L_2, L_3) = (y_i - y_j)\left(L_i^2 L_j + \frac{L_i L_j L_k}{2}\right) - (y_k - y_i)\left(L_i^2 L_k + \frac{L_i L_j L_k}{2}\right).$$

In these formulas, node n is a vertex of the triangle element with index i. The three indexes i, j and k comprise a cyclic permutation of 1, 2 and 3. Figure 6.2 shows the profiles of the shape functions for a node A with global index n defined on a triangle element. Red and blue lines on those figures yield the cross section of the x and y derivatives, respectively. As seen in Figure 6.2, the shape functions and their first derivatives take values 1 or 0 on nodes A, B and C. In Figure 6.2(a), the function ϕ_{3n-2} equals 1 at node A, and 0 at nodes B and C, and it has zero derivatives in all nodes. The function ϕ_{3n-1} of Figure 6.2(b) and its y derivative are zero at all nodes, whereas its x derivative is 1 at node A and zero at nodes B and C.

Zienkiewicz element is not conformed because as it can be seen in Figure 6.2 first derivatives have nonzero value on the edge opposed to node A. A neighbor element which shares edge BC with the considered one cannot

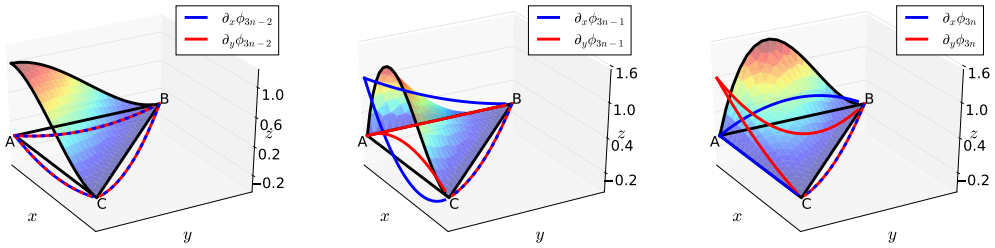

(a) (b) (c)

Figure 6.2: Profiles of shape functions ϕ_{3n-2} (a), ϕ_{3n-1} (b) and ϕ_{3n} (c) of Zienkiewicz element corresponding to node A with index n. Blue and red lines depict cross sections of x and y derivatives respectively.

fit those derivatives since it does not have value in node A. It means that first derivatives of numerical solution may have jumps between elements.

6.1.2 Hseih-Clough-Tocher element

Hseih-Clough-Tocher elements provide a conformed approximation for plate bending problem but their shape functions are not polynomial even on the elements. We will use a reduce Hseih-Clough-Tocher element (rHCT) described in paper Peker et al (2007). Similarly to Zienkiewicz element in each node n we define 3 shape functions ϕ_{3n-2}, ϕ_{3n-1}, ϕ_{3n} corresponding to value of numerical solution in this node and values of first derivatives respect to x and y. In difference with the previous case functions ϕ_i are cubic piecewize polynomial on the element. In order to construct them we split the triangle ABC into three smaller triangle $\mathcal{A} = BCQ$, $\mathcal{B} = ACQ$, and $\mathcal{C} = ABQ$ by point Q inside it (Figure 6.3). Even though it is possible to choose any point inside the triangle we will suppose that Q is the center and its coordinates are $x_0 = \frac{1}{3}\sum_{i=1}^{3} x_i$ and $y_0 = \frac{1}{3}\sum_{i=1}^{3} y_i$. In each subtriangle we define baricentric corrdinate system α_i, β_i, and γ_i, $i = 1, 2, 3$. Shape function will be given by cubic polynomials in each subtriangle and should be continuous and smooth on their edges. Following Peker et al (2007) we will seek the expressions in

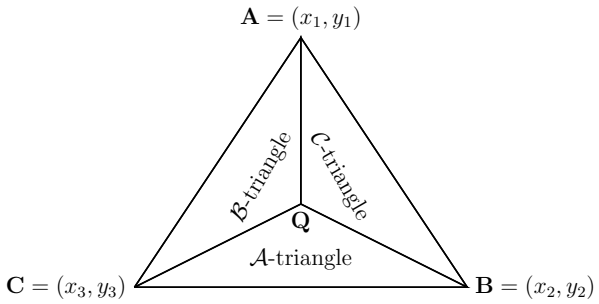

Figure 6.3: Notation of rHCT element and its splitting.

Berstein-Bezier form:

$$z^{(\mathcal{A})}(\alpha_1,\alpha_2,\alpha_3) = \sum_{i+j+k=3} a_{ijk}\frac{3!}{i!j!k!}\alpha_1^i\alpha_2^j\alpha_3^k,$$
$$z^{(\mathcal{B})}(\beta_1,\beta_2,\beta_3) = \sum_{i+j+k=3} b_{ijk}\frac{3!}{i!j!k!}\beta_1^i\beta_2^j\beta_3^k,$$
$$z^{(\mathcal{C})}(\gamma_1,\gamma_2,\gamma_3) = \sum_{i+j+k=3} c_{ijk}\frac{3!}{i!j!k!}\gamma_1^i\gamma_2^j\gamma_3^k.$$

Here $z^{(\mathcal{A})}$, $z^{(\mathcal{B})}$, and $z^{(\mathcal{C})}$ are cubic polynomial which represents shape functions in subtriangles $\mathcal{A}$, $\mathcal{B}$, and $\mathcal{C}$ respectively. Similarly to Zienkiewicz element all 9 shape functions are defined by their values z_i in vertices A, B, and C, and values of derivatives z_i^x and z_i^y in the same vertices. For example for ϕ_{3n-1} which corresponds to vertex A we choose $z_1 = 1$, $z_i = 0$, $i = 1, 2$, and $z_i^x = z_i^y = 0$, $i = 1, 2, 3$. For ϕ_{3n-1} which corresponds to x-derivative in A we have $z_1^x = 1$, $z_i^x = 0$, $i = 1, 2$, and $z_i = z_i^y = 0$, $i = 1, 2, 3$. And for ϕ_{3n} representing y-derivatives we choose $z_1^y = 1$, $z_i^y = 0$, $i = 1, 2$, and $z_i = z_i^x = 0$, $i = 1, 2, 3$.

In order to calculate coefficients a_{ijk}, b_{ijk}, and c_{ijk} we introduces matrices $\mathbf{X}$ and $\mathbf{Y}$ with elements $x_{ij} = x_i - x_j$, $y_{ij} = y_i - y_j$ where $i, j \in \{0, 1, 2, 3\}$.

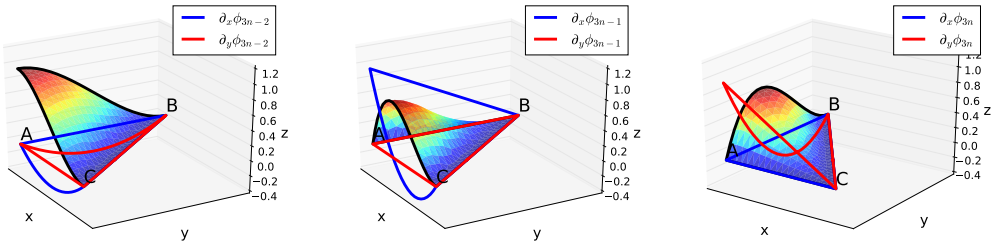

(a) (b) (c)

Figure 6.4: Profiles of shape functions ϕ_{3n-2} (a), ϕ_{3n-1} (b) and ϕ_{3n} (c) of rHCT element corresponding to node A with index n. Blue and red lines depict cross sections of x and y derivatives respectively.

Coefficients for the polynomial $z^{(\mathcal{A})}$ can be found as follows:

$$
\begin{aligned}
&a_{030} = z_2, \quad a_{003} = z_3,\\
&a_{120} = z_2 + z_2^x\frac{x_{02}}{3} + z_2^y\frac{y_{02}}{3}, \quad a_{102} = z_3 + z_3^x\frac{x_{03}}{3} + z_3^y\frac{y_{03}}{3},\\
&a_{021} = z_2 + z_2^x\frac{x_{32}}{3} + z_2^y\frac{y_{32}}{3}, \quad a_{012} = z_3 + z_3^x\frac{x_{23}}{3} + z_3^y\frac{y_{23}}{3},\\
&a_{111} = \frac{a_{120}-a_{021}+a_{102}-a_{012}}{2} + \overrightarrow{CB}\cdot\frac{(z_2-3a_{021})\overrightarrow{QC}-(z_3-3a_{012})\overrightarrow{QB}}{2|\overrightarrow{CB}|^2},\\
&a_{210} = \frac{c_{111}+a_{120}+a_{111}}{3}, \quad a_{201} = \frac{a_{111}+b_{120}+b_{111}}{3}, \quad a_{300} = \frac{a_{201}+b_{201}+c_{201}}{3}.
\end{aligned}
$$

The rest coefficients are defined similarly by cyclic permutations of a, b, and c, indeces 1,2,3 of z, z^x, z^y, $\mathbf{X}$, $\mathbf{Y}$ (note that 0-index is fixed), and points A, B, and C. Profiles of shape functions for vertex A corresponding to node with global index n are depicted in Figure 6.4. Easy to see that now both first derivatives equal to zero on the opposite edge of the triangle hence numerical approximation will be smooth.

6.1.3 Linear element

For in-plane displacements $\mathbf{u}$ we will use linear finite elements which define subspace U_h of $U = W^{1,2}(\Omega) \times W^{1,2}(\Omega)$. These elements have only 3 shape function each of that represents value of numerical approximation in the corresponding node. For each component of vector $\mathbf{u}$ shape function can be written as follows:

$$\phi_n(L_1, L_2, L_3) = L_1, \quad \phi_m(L_1, L_2, L_3) = L_2, \quad \phi_k(L_1, L_2, L_3) = L_3, \qquad (6.2)$$

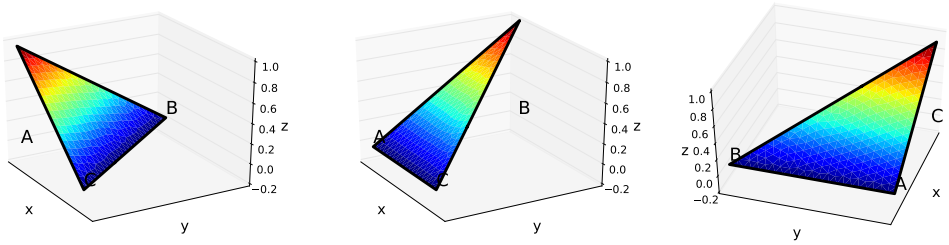

(a) (b) (c)

Figure 6.5: Profiles of shape functions ϕ_n (a), ϕ_m (b) and ϕ_k (c) of linear element.

where n, m, and k are global indeces of first, second, and third vertices, L_i are baricentric coordinates. The profiles and ϕ_n, ϕ_m, and ϕ_k are depicted in Figure 6.5.

6.2 Numerical approximation of energy functional

6.2.1 Airy potential case

We start to construct of finite dimensional reduction of energy functional from simple case (5.36) which was described in our paper Iakunin and Bonilla (2018) and for which we can use Aity potential. A triangularization of the domain Ω by elements with size h defines linear spaces V_h and H_h, which are used to approximate V and H respectively. The finite element method solves the problem (5.36) on those simpler finite-dimensional spaces instead of V and H. The shape functions form a basis of V_h and H_h. Thus the approximations $\hat{\zeta}$ of the deflection and $\hat{\chi}$ of the Airy potential are

$$\hat{\zeta}(x,y) = \sum_{n \in \text{all nodes}} \left(\hat{\zeta}_{3n-2}\phi_{3n-2}(x,y) + \hat{\zeta}_{3n-1}\phi_{3n-1}(x,y) + \hat{\zeta}_{3n}\phi_{3n}(x,y) \right), \quad (6.3)$$

$$\hat{\chi}(x,y) = \sum_{n \in \text{internal}} \left(\hat{\chi}_{3n-2}\phi_{3n-2}(x,y) + \hat{\chi}_{3n-1}\phi_{3n-1}(x,y) + \hat{\chi}_{3n}\phi_{3n}(x,y) \right). \quad (6.4)$$

Here coefficients f_{3n-2}, f_{3n-1} and f_{3n} are the values of f, $f_{,x}$ and $f_{,y}$ at the node n, with $f = \hat{\zeta}$, $\hat{\chi}$. The Airy potential and its normal derivative are zero at the boundary. Thus we calculate it only at internal nodes inside Ω. We

can simplify formulas (6.3) and (6.4) by introducing two vectors $\boldsymbol{\zeta} \in \mathbb{R}^{3N}$, $\boldsymbol{\chi} \in \mathbb{R}^{3M}$ and two vector functions $\boldsymbol{\phi} : \mathbb{R}^2 \to \mathbb{R}^{3N}$, containing all shape functions $\phi_i(x, y)$, and $\boldsymbol{\phi}^{int} : \mathbb{R}^2 \to \mathbb{R}^{3M}$, containing only shape functions corresponding to internal nodes. Now the sums can be written using matrix multiplication:

$$\hat{\zeta}(x, y) = \boldsymbol{\zeta}^T \boldsymbol{\phi}(x, y), \quad \hat{\chi}(x, y) = \boldsymbol{\chi}^T \boldsymbol{\phi}^{int}(x, y). \tag{6.5}$$

Here N and $M < N$ are the total number of nodes and of internal nodes, respectively. $3N$ and $3M$ are the dimensions of V_h and H_h, respectively. Norms $\|\zeta\|_{L^2(\Omega)}$, $\|\chi\|_H$ and seminorm $|\zeta|_V$ can be reduced to the defined spaces and written as:

$$\begin{aligned} \|\hat{\zeta}\|^2_{L^2(\Omega)} &= \boldsymbol{\zeta}^T \mathbf{G} \boldsymbol{\zeta} = \|\hat{\zeta}\|^2_{V_h}, \\ |\hat{\zeta}|^2_V &= \boldsymbol{\zeta}^T \mathbf{G}^{(B)} \boldsymbol{\zeta} = |\hat{\zeta}|^2_{V_h}, \\ \|\hat{\chi}\|^2_H &= \boldsymbol{\chi}^T \mathbf{G}^{(S)} \boldsymbol{\chi} = \|\hat{\chi}\|^2_{2,H_h}, \end{aligned} \tag{6.6}$$

where $\mathbf{G} \in \mathbb{R}^{3N \times 3N}$, $\mathbf{G}^{(S)} \in \mathbb{R}^{3M \times 3M}$ are symmetric positive definite Gram matrices and $\mathbf{G}^{(B)} \in \mathbb{R}^{3N \times 3N}$ is symmetric positive semidefinite. The components of these matrices are

$$\begin{aligned} G_{ij} &= \int_\Omega \phi_i(x, y) \phi_j(x, y) \, dx \, dy, \\ G^{(B)}_{ij} &= a_{bend}(\phi_i, \phi_j), \\ G^{(S)}_{ij} &= a_{stretch}(\phi^{int}_i, \phi^{int}_j), \end{aligned} \tag{6.7}$$

where $a_{bend}(\zeta, v)$ and $a_{stretch}(\chi, \Phi)$ are defined by (5.16) and (5.18), and ϕ_i, ϕ^{int}_i are i-th components of vector-functions $\boldsymbol{\phi}$ and $\boldsymbol{\phi}^{int}$ respectively.

Having approximated the norms in V and H, we can approximate the norm of functional $L(\zeta)\chi$ given by (5.23). We define a new functional $L_h(\zeta)\chi$ that coincides with $L(\zeta)\chi$ for all $\chi \in H_h$. Instead of $\zeta \in V$, we use our approximations $\hat{\zeta} \in V_h$. Thus the functional $L_h(\hat{\zeta})$ can be written as a vector-function $\mathbf{l}(\boldsymbol{\zeta}) : \mathbb{R}^{3N} \to \mathbb{R}^{3M}$, each component of which is given by

$$l_i(\boldsymbol{\zeta}) = L_h(\boldsymbol{\zeta}^T \boldsymbol{\phi}) \phi^{int}_i = L_h(\hat{\zeta}) \phi^{int}_i = L(\hat{\zeta}) \phi^{int}_i. \tag{6.8}$$

We calculate the norm of the functional $L_h(\hat{\zeta})$ on H_h by using a definition of operator norm:

$$\begin{aligned} \|L_h(\hat{\zeta})\|_{H^*_h} &= \sup_{\hat{\chi} \in H_h \setminus \{0\}} \frac{|L(\hat{\zeta})\hat{\chi}|}{\|\hat{\chi}\|_{H_h}} = \sup_{\boldsymbol{\chi} \neq 0} \frac{|\mathbf{l}(\boldsymbol{\zeta})^T \boldsymbol{\chi}|}{\sqrt{\boldsymbol{\chi}^T \mathbf{G}^{(S)} \boldsymbol{\chi}}} \\ &= \sup_{\boldsymbol{\chi} \neq 0} \frac{\left| \left(\mathbf{Q}^{(S)} \boldsymbol{l}(\boldsymbol{\zeta}) \right)^T \mathbf{G}^{(S)} \boldsymbol{\chi} \right|}{\sqrt{\boldsymbol{\chi}^T \mathbf{G}^{(S)} \boldsymbol{\chi}}}. \end{aligned} \tag{6.9}$$

Here we have used the inverse $\mathbf{Q}^{(S)}$ of the symmetric Gram matrix $\mathbf{G}^{(S)}$ with components defined in (6.7). The solution of the maximization problem (6.9) is

$$\boldsymbol{\chi}_0(\boldsymbol{\zeta}) = \mathbf{Q}^{(S)}\boldsymbol{l}(\boldsymbol{\zeta}), \tag{6.10}$$

which corresponds to $\hat{\chi}_0(\zeta)$ that approximates the solution $\chi_0(\zeta)$ of (5.32).

Putting together all the results in this section, we obtain a finite dimensional version of problem (5.36):

$$\begin{aligned}
&\min_{\boldsymbol{\zeta}\in\mathbb{R}^{3N}} J_h(\boldsymbol{\zeta}),\\
&J_h(\boldsymbol{\zeta}) = \frac{1}{2}\left[\frac{1}{\kappa^2}|\boldsymbol{\zeta}|^2_{\mathbf{G}^{(B)}} + \frac{2\beta(1-\nu)}{(1-2\nu)\kappa^2}|\boldsymbol{\zeta}|^2_{\mathbf{G}} + |\mathbf{l}(\boldsymbol{\zeta})|^2_{\mathbf{Q}^{(S)}}\right],\\
&|\mathbf{v}|^2_{\mathbf{A}} = \mathbf{v}^T\mathbf{A}\mathbf{v},\ \mathbf{A}\in\mathbb{R}^{D\times D},\ \mathbf{A}^T=\mathbf{A},\ \mathbf{A}\succeq 0,\ \mathbf{v}\in\mathbb{R}^D.
\end{aligned} \tag{6.11}$$

The main computational challenge in (6.11) is the last term, which is nonlinear and fourth order with respect to the components of $\boldsymbol{\zeta}$. Moreover, the matrix $\mathbf{Q}^{(S)}$ is full-populated, which makes the Hessian of J_h a dense matrix.

6.2.2 General case

Now we can consider general case and construct finite element approximation of the functional (5.66). For vertical deflection ζ we will use similar subspace V_h with elements given by (6.3) and norm given by matrices $\mathbf{G}$ and $\mathbf{G}^{(B)}$ from formula (6.6).

For in-plane displacements we use linear finite elements and define subspace $U_h \subset U = W^{1,2}(\Omega)\times W^{1,2}(\Omega)$. The main challenge here consists in that in-plane displacement is a vector function $\mathbf{u}(x,y) = u_1(x,y)\mathbf{e}_1 + u_2(x,y)\mathbf{e}_2$ where $\mathbf{e}_1$ and $\mathbf{e}_2$ are unite vectors in x and y directions respectively. Linear approximation for each component require N degrees of freedom (one shape function for each node) thus the subspace U_h is isomorphic to $\mathbb{R}^{N\times 2}$ or $\mathbb{R}^{2N}$ where first N components corresponds to displacement in x-direction and last N components to displacement in y direction. Let us call $\hat{\mathbf{u}}(x,y)$ the numerical approximation of $\mathbf{u}(x,y)$. Its components $\hat{u}_1$ and $\hat{u}_2$ are given by:

$$\begin{aligned}
\hat{\mathbf{u}}(x,y) = \begin{pmatrix}\hat{u}_1(x,y)\\ \hat{u}_2(x,y)\end{pmatrix} =\\
\begin{pmatrix}\sum_{n\in\text{all nodes}} u_{1,n}\psi_n(x,y)\\ \sum_{n\in\text{all nodes}} u_{2,n}\psi_n(x,y)\end{pmatrix} = \begin{pmatrix}\boldsymbol{\psi}(x,y) & 0\\ 0 & \boldsymbol{\psi}(x,y)\end{pmatrix}^T\mathbf{U},
\end{aligned} \tag{6.12}$$

where $\boldsymbol{\psi}(x,y) : \mathbb{R}^2 \to \mathbb{R}^N$ is a vector function composed of shape function corresponding to all nodes, $\mathbf{U} = \begin{pmatrix} \mathbf{u_1} \\ \mathbf{u_2} \end{pmatrix} \in \mathbb{R}^{2N}$. Finite dimensional analogs of L^2-norm is given as follows:

$$\|\hat{\mathbf{u}}\|^2_{L^2(\Omega)} = \|\mathbf{U}\|^2_{U_h} = \mathbf{U}^T \begin{pmatrix} \mathbf{H} & 0 \\ 0 & \mathbf{H} \end{pmatrix} \mathbf{U},$$
$$H_{ij} = \int_\Omega \psi_i(x,y)\psi_j(x,y)\ dxdy,\ i,j \in \{1,\dots,N\}, \tag{6.13}$$

Note that in-plane displacements in different directions are separate. It does not happen with stretching energy bilinear form given by (5.56) which finite dimensional approximation has the shape

$$a_{disp}(\hat{\mathbf{u}},\hat{\mathbf{u}}) = \mathbf{U}^T \begin{pmatrix} \mathbf{Q}_{11} & \mathbf{Q}_{12} \\ \mathbf{Q}_{12}^T & \mathbf{Q}_{22} \end{pmatrix} \mathbf{U},$$
$$Q_{11,ij} = a_{disp}(\psi_i\mathbf{e}_1, \psi_j\mathbf{e}_1), \quad Q_{22,ij} = a_{disp}(\psi_i\mathbf{e}_2, \psi_j\mathbf{e}_2),$$
$$Q_{12,ij} = a_{disp}(\psi_i\mathbf{e}_1, \psi_j\mathbf{e}_2). \tag{6.14}$$

Using formulas (6.13) and (6.14) we can write numerical analog of norm in space U:

$$\|\hat{\mathbf{u}}\|^2_U = \beta\gamma^2(\hat{\mathbf{u}},\hat{\mathbf{u}}) + a_{disp}(\hat{\mathbf{u}},\hat{\mathbf{u}})$$
$$= \mathbf{U}^T \begin{pmatrix} \beta\gamma^2\mathbf{H} + \mathbf{Q}_{11} & \mathbf{Q}_{12} \\ \mathbf{Q}_{12} & \beta\gamma^2\mathbf{H} + \mathbf{Q}_{22} \end{pmatrix} \mathbf{U} = \mathbf{U}^T\mathbf{Q}\mathbf{U}. \tag{6.15}$$

Matrix $\mathbf{Q}$ is non degenerate if and only if $\beta > 0$. For the case $\beta = 0$ we can use Airy potential approach without any problems.

Similarly to the previous case we can reduce functional $L(\zeta)$ given by (5.59) on subspace U_h. Since this subspace is isomorphic to $\mathbb{R}^{2N}$ the reduced functional also can be represented as a vector in $\mathbb{R}^{2N}$. Applying the functional $L(\zeta)$ to all shape functions we obtain its reduction to U_h:

$$\mathbf{l}(\zeta) = L(\zeta) \begin{pmatrix} \boldsymbol{\psi}^T & 0 \\ 0 & \boldsymbol{\psi}^T \end{pmatrix},$$
$$l_i(\zeta) = L(\zeta)\psi_i\mathbf{e}_1, \quad l_{N+i}(\zeta) = L(\zeta)\psi_i\mathbf{e}_2, \quad i \in \{1,\dots,N\}. \tag{6.16}$$

In order to calculate norm of reduced functional we can use definition of norm similarly to (6.9)

$$\|\mathbf{l}(\zeta)\|_{U_h^*} = \sup_{\mathbf{U}\neq 0} \frac{|\mathbf{l}^T(\zeta)\mathbf{U}|}{\|\mathbf{U}\|_{U_h}} = \sqrt{\mathbf{l}^T(\zeta)\mathbf{Q}^{-1}\mathbf{l}(\zeta)}. \tag{6.17}$$

Including contributions from (6.7) and (6.17) we obtain numerical approximation $\mathcal{W}_h$ of the energy functional $\mathcal{W}$ given by (5.66)

$$\begin{aligned}
&\min_{\boldsymbol{\zeta}\in\mathbb{R}^{3N}} \mathcal{W}_h(\boldsymbol{\zeta}),\\
&\mathcal{W}_h(\boldsymbol{\zeta}) = \frac{1}{2}\left[\frac{1}{\kappa^2}|\boldsymbol{\zeta}|^2_{\mathbf{G}^{(B)}} + \frac{2\beta(1-\nu)}{(1-2\nu)\kappa^2}|\boldsymbol{\zeta}|^2_{\mathbf{G}} - |\mathbf{l}(\boldsymbol{\zeta})|^2_{\mathbf{Q}^{-1}} + R(\boldsymbol{\zeta})\right], \quad (6.18)\\
&|\mathbf{v}|^2_{\mathbf{A}} = \mathbf{v}^T\mathbf{A}\mathbf{v},\ \mathbf{A}\in\mathbb{R}^{D\times D},\ \mathbf{A}^T=\mathbf{A},\ \mathbf{A}\succeq 0,\ \mathbf{v}\in\mathbb{R}^D.
\end{aligned}$$

where $R(\boldsymbol{\zeta}) = r\left(\boldsymbol{\zeta}^T\boldsymbol{\phi}(x,y)\right) = r\left(\hat{\zeta}(x,y)\right)$.

6.3 Algorithm

In this subsection we provide a minimization algorithm for functional J_h from problem (6.11). We will never use the shape of this functional but only take into account that it is smooth hence our method can be applied to general energy functional $\mathcal{W}_h$ without any changes. Since J_h is smooth, the solution of (6.11) is given by a system of nonlinear equations:

$$\frac{\partial}{\partial\zeta_i}J_h(\boldsymbol{\zeta}) = 0,\ i\in\{1,\dots,3N\} \Leftrightarrow \nabla J_h(\boldsymbol{\zeta}) = \mathbf{0}. \quad (6.19)$$

Instead of solving these equations, it is simpler to go back to the time dependent formulation and look for stationary solutions of the dynamic problem:

$$\frac{d\boldsymbol{\zeta}(t)}{dt} + \nabla J_h(\boldsymbol{\zeta}(t)) = \mathbf{0}. \quad (6.20)$$

To solve this equation, we adopt a Crank-Nicholson scheme that consists of updating of values of $\boldsymbol{\zeta}^{(k)}$ at each time step k using the formula:

$$\boldsymbol{\zeta}^{(k)} = \boldsymbol{\zeta}^{(k-1)} - \frac{\tau}{2}\left(\nabla J_h(\boldsymbol{\zeta}^{(k-1)}) + \nabla J_h(\boldsymbol{\zeta}^{(k)})\right),\ k\in\mathbb{N}, \quad (6.21)$$

with a given initial condition $\boldsymbol{\zeta}^{(0)}$ and time step τ. The equation (6.21) is nonlinear thus we have to use a Newton-Raphson method to solve it numerically. Below we display Algorithm 1 for solving (6.11).

The most complex part of Algorithm 1 is solving the system of linear equations on line 8. The matrix $\mathbf{H}_{\boldsymbol{\eta}}$ is ill-conditioned and it can be indefinite because it contains the indefinite Hessian of $\mathbf{l}(\boldsymbol{\zeta})$ (which is not convex nor concave). This peculiarity of J_h leads to some troubles, as the Newton-Raphson method requires a large number of steps to converge. Nevertheless we can always decrease the time step τ in low convergence intervals, which

Algorithm 1 Numerical method

Require: initial condition $\boldsymbol{\zeta}^{(0)}$, time step τ, approximation J_h of functional J, Newton-Raphson method tolerance $\epsilon_{\text{N-R}}$

$\boldsymbol{\zeta} \leftarrow \boldsymbol{\zeta}^{(0)}$
▷ Main loop for calculating deflection
while convergence doesn't achieve **do**
▷ Initialization for Newton-Raphson method
  $\mathbf{g}_{\boldsymbol{\zeta}} \leftarrow$gradient$[J_h, \boldsymbol{\zeta}]$
  $\boldsymbol{\eta} \leftarrow \boldsymbol{\zeta}$
▷ Newton-Raphson iterations to solve (6.21)
  repeat
    $\mathbf{g}_{\boldsymbol{\eta}} \leftarrow$gradient$[J_h, \boldsymbol{\eta}]$
    $\mathbf{H}_{\boldsymbol{\eta}} \leftarrow$ hessian$[J_h, \boldsymbol{\eta}]$
    $\boldsymbol{\delta} \leftarrow$ solveLinearSystem$\left[\mathbf{I}+\frac{\tau}{2}\mathbf{H}_{\boldsymbol{\eta}}, \boldsymbol{\eta}-\boldsymbol{\zeta}+\frac{\tau}{2}(\mathbf{g}_{\boldsymbol{\eta}}+\mathbf{g}_{\boldsymbol{\zeta}})\right]$
    $\boldsymbol{\eta} \leftarrow \boldsymbol{\eta} - \boldsymbol{\delta}$
  until $\|\boldsymbol{\delta}\| < \epsilon_{\text{N-R}}$
▷ Updating values of deflections
  $\boldsymbol{\zeta} \leftarrow \boldsymbol{\eta}$
end while

improves the numerical properties of $\mathbf{I} + \frac{\tau}{2}\mathbf{H}_{\boldsymbol{\eta}}$ at the expense of a greater number of outer iterations.

Another challenge to implement the algorithm is to find an initial condition $\boldsymbol{\zeta}^{(0)}$, because the vector $\boldsymbol{\zeta}$ approximates $\zeta(x, y)$ and its first derivatives $\zeta_{,x}(x, y)$ and $\zeta_{,y}(x, y)$. Therefore the initial condition should be smooth. One way to generate $\boldsymbol{\zeta}^{(0)}$ is to smoothen a random linear piecewise function by convolution with a kernel (for example, a Gaussian kernel). In order to do it we firstly generate for each node random uniformly distributed values $s_n, n \in \{1, 2, \ldots, N\}$ with mean 0 and dispersion h. Then we assign to each node n a piecewise linear function $\psi_n(x, y)$ of linear finite element given by

formula (6.2). Now a smooth initial condition can be obtained as follows:

$$
\begin{aligned}
s(x,y) &= \sum_{i=1}^{N} s_i \psi_i(x,y), \\
\zeta^{(0)}_{3n-2} &= \int_\Omega s(x,y) K(x,y,x_n,y_n)\, dxdy, \qquad (6.22)\\
\zeta^{(0)}_{3n-1} &= \int_\Omega s(x,y) \frac{\partial}{\partial \xi} K(x,y,\xi,\eta)\, dxdy \Big|_{\xi=x_n,\eta=y_n} \\
\zeta^{(0)}_{3n} &= \int_\Omega s(x,y) \frac{\partial}{\partial \eta} K(x,y,\xi,\eta)\, dxdy \Big|_{\xi=x_n,\eta=y_n} \\
K(x,y,\xi,\eta) &= \frac{1}{2\pi\sigma^2} e^{-\frac{(x-\xi)^2+(y-\eta)^2}{2\sigma^2}}. \qquad (6.23)
\end{aligned}
$$

Here x_n, y_n are the coordinates of node n, and σ can be chosen a few times larger than the element size. In (6.22), the initial conditions $\zeta^{(0)}_{3n-1}$ and $\zeta^{(0)}_{3n}$ correspond to actual derivatives of some function, which saves a few extra iteration steps. We can also note that the solution obtained on a rough mesh can be successfully used as an initial condition for a refined mesh. This helps decreasing the computation time needed to obtain the stationary solution.

During implementation of this algorithm one may face a difficulties related to that most of parameters such as thickness, Young modulus, and growth tensor of the biofilm are not constant values but functions. Thus if we use compiled programming language such as C++ we have to recompile the code for any alteration of parameters that is quite uncomfortable a takes some time. On the other hand scripts and interpreted language such as Python usually do not provide the high performance necessary for simulation of biofilms. The way we chose in our work is to combine these two paradigms that is to develop a library on C++ which allows to perform the heaviest computations and call functions from this library in Python script. This approach requires only one compilation of the library however allows to launch simulation with different parameters in different Python scripts. The interaction between C++ and Python we realized thereby Boost Python library.

Chapter 7

Verification of numerical method

Numerical methods presented in the previous chapter we can verify on examples with known solution. As was consider in chapter 4 if a circular homogeneous biofilm undergoes homogeneous radial or azimuthal growth it bends into a cone or a saddle respectively. Furthermore, if an elastic agar substratum is presented those shapes will corrugate. Thus we will use these examples to verify numerical procedure, compare Zienkiewich and Hseigh-Clough-Tocher (HCT) elements, and analyze when Airy potential simplification (3.43)-(3.44) of the general system (3.38)-(3.39) is possible.

For a circular homogeneous biofilm undergoing azimuthal or radial growth on a viscoelastic substratum equations (3.38)-(3.39) have the following shape

$$\frac{\partial \zeta}{\partial t} = -\frac{\mu_\infty}{\eta}\zeta - \frac{H(1-2\nu)}{2\eta(1-\nu)}\left(\frac{Eh^3}{9}\Delta^2\zeta - h\nabla\cdot\left(\boldsymbol{\sigma}^{(0)}\cdot\nabla\zeta\right)\right), \quad (7.1)$$

$$\frac{\partial \mathbf{u}}{\partial t} = -\frac{\mu_\infty}{\eta}\mathbf{u} + \frac{Hh}{\eta}\nabla\cdot\boldsymbol{\sigma}^{(0)}, \quad (7.2)$$

where ζ is vertical deflection, $\mathbf{u}$ is in-plane displacements, E and h are Young modulus and thickness of the film, η, μ_∞, ν, and H are viscosity, rubbery modulus, Poisson ratio, and thickness of the substratum, $\boldsymbol{\sigma}^0$ is stretching stress, and t is time. Equations (7.1)-(7.2) should be accompanied with boundary conditions:

$$2\Delta\zeta - \frac{1}{r}\zeta_{,r} - \frac{1}{r^2}\zeta_{,\theta\theta} = 0, \text{ at } r = R, \quad (7.3)$$

$$2\frac{\partial}{\partial r}\Delta\zeta + \frac{1}{r}\frac{\partial^2}{\partial r\partial\theta}\left(\frac{1}{r}\zeta_{,\theta}\right) = 0, \text{ at } r = R, \quad (7.4)$$

$$\sigma^{(0)}_{rr} = 0 \text{ at } r = R, \quad (7.5)$$

film	
R, cm	1
h, cm	0.07, 0.035, 0.01
E, Pa	25000
substratum	
η, Pa $\cdot$ s	1
H, cm	0.7
μ_∞, Pa	0 (pure viscous), 25, 50
ν	0.45
growth	
10% radial	$g_r = 0.1$, $g_\theta = 0$
10% azimuthal	$g_r = 0$, $g_\theta = 0.1$

Table 7.1: Main parameters of biofilm and agar substratum used in test examples.

where r and θ are radial and azimuthal coordinates, R is radius of the biofilm, $\sigma_{rr}^{(0)}$ is radial stretching stress. We assume that the biofilm undergoes homoegenous anisotropic growth in polar coordinates which can be written as

$$\mathbf{g}^{(p)} = \begin{pmatrix} g_r & 0 \\ 0 & g_\theta \end{pmatrix} \Rightarrow \mathbf{g}^{(c)} = \frac{1}{x^2+y^2} \begin{pmatrix} g_r x^2 + g_\theta y^2 & (g_r - g_\theta)xy \\ (g_r - g_\theta)xy & g_r y^2 + g_\theta x^2 \end{pmatrix}, \tag{7.6}$$

where g_r is radial growth and g_θ is azimuthal growth. In order to verify numerical method we will consider biofilms with the following parameters:

We can nondimensionalize equations (7.1)-(7.2) by introducing scales from the tables 3.1 and 3.2:

$$\frac{\partial \zeta}{\partial t} = -\beta\zeta - \frac{(1-2\nu)\kappa^2}{2(1-\nu)} \left(\frac{1}{9\kappa^2} \Delta^2 \zeta - \nabla \cdot \left(\boldsymbol{\sigma}^{(0)} \cdot \nabla \zeta \right) \right), \tag{7.7}$$

$$\nabla \cdot \boldsymbol{\sigma}^{(0)} = \gamma^2 \left(\beta \mathbf{u} + \frac{\partial \mathbf{u}}{\partial t} \right) \approx \gamma^2 \beta \mathbf{u}. \tag{7.8}$$

since γ is very small. If β is also small (that is the agar layer is soft and almost purely viscous) we can simplify this system using Airy potential:

$$\frac{\partial \zeta}{\partial t} = -\beta\zeta - \frac{(1-2\nu)\kappa^2}{2(1-\nu)} \left(\frac{1}{9\kappa^2} \Delta^2 \zeta - 2\left[\chi, \zeta\right] \right), \tag{7.9}$$

$$\Delta^2 \chi + [\zeta, \zeta] = \Psi, \tag{7.10}$$

where $\Psi = k\delta(r)/r$ is Gaussian curvature which depends only of difference $k = g_r - g_\theta$ between components of growth. As was shown in chapter 4 if $k > 0$

#	10 % growth	substratum	element type	system type
1	radial	pure viscous	Zienkiewicz	Airy
2	azimuthal	pure viscous	Zienkiewicz	Airy
3	radial	pure viscous	HCT	Airy
4	azimuthal	pure viscous	HCT	Airy
5	radial	stiff (μ_∞ =25 and 50 Pa)	Zienkiewicz	Airy
6	azimuthal	stiff (μ_∞ =25 and 50 Pa)	Zienkiewicz	Airy
7	radial	stiff (μ_∞ =25 and 50 Pa)	Zienkiewicz	General
8	azimuthal	stiff (μ_∞ =25 and 50 Pa)	Zienkiewicz	General

Table 7.2: Test cases for homogeneous anisotropic growth in polar coordinates. Young modulus for all cases is 25 kPa, radius of biofilm is 1 cm, thickness of agar substratum and its Poisson ratio are 0.7 cm and 0.45.

the solution is a cone and if $k < 0$ the solution is a saddle. Furthermore, there are boundary and corner layers which size depends on the film thickness: the thinner the film is the thinner layers are.

To perform numerical simulation we make a triangulation of the circular domain such that the resulting mesh contains 2774 elements and 1452 nodes. To solve discretized problem we will use two types of finite elements: Zienkiewicz and HCT. We will also consider two formulations: the general one (7.7)-(7.8) (GF) and simplified Airy potential formulation (7.9)-(7.10) (AF). Test cases are provided in table 7.2 and for each example we will use 3 different thickness of biofilm provided in table 7.1. In the end of this chapter we will study two cases of heterogeneous growth in order to demonstrate all capacities of the solver.

7.1 Comparison with theory

We start from the first test case in table 7.2. Results of simulation are depicted in Figure 7.1. As was predicted the solution is a cone and it is possible to see that for thinner film this cone has a sharper tip. Analogously Figure 7.2 shows second test example corresponded to azimuthal growth and saddle solution. Again we can see that inclinations near center are sharper for thin film.

The shrinkage of corner and boundary layer can be seen better in cross sections. In the case of radial growth Figure 7.3-(a) depicts the scaled radial derivatives of ζ calculated by solving 1D radial ODEs by finite differences (as it was done in chapter 4) and by solving 2D PDEs (7.9)-(7.10) by finite elements. We see that the radially symmetric solution from chapter 4 and the

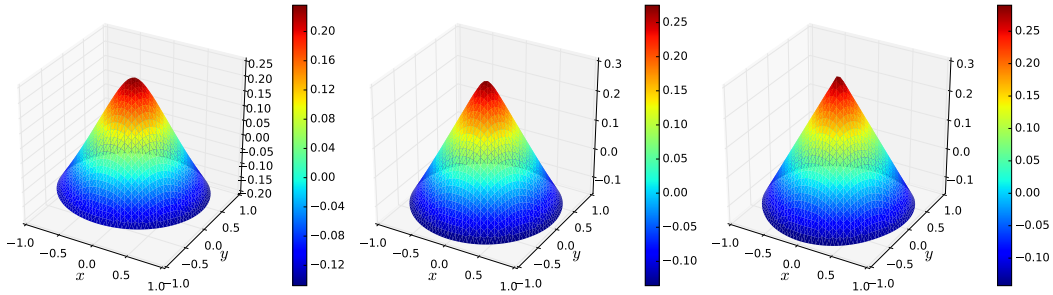

(a) (b) (c)

Figure 7.1: 10% radial growth of films with thickness (a) $h = 0.07$ cm, (b) $h = 0.035$ cm, (c) $h = 0.01$ cm on a pure viscous layer.

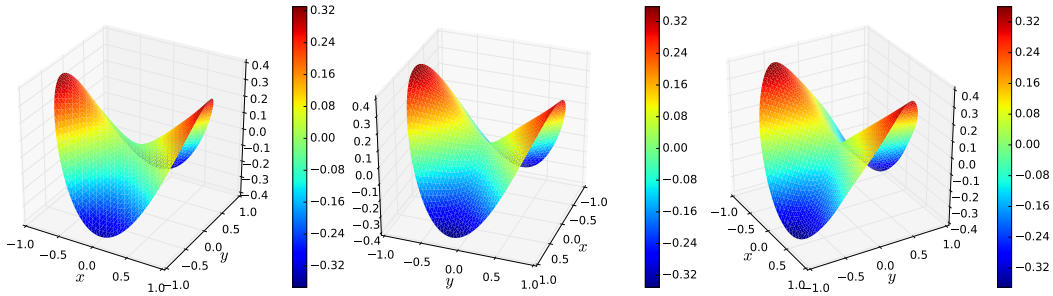

(a) (b) (c)

Figure 7.2: 10% azimuthal growth of films with thickness (a) $h = 0.07$ cm, (b) $h = 0.035$ cm, (c) $h = 0.01$ cm on a pure viscous layer.

2D numerical solution almost coincide. The small difference near $r = 1$ arises because we explicitly set the boundary condition (7.3) in the 1D whereas in the 2D solver it arises naturally from the properties of the vector space where we perform minimization. Another artifact is a jump of ϕ near the origin in 2D solution for $\gamma = 0.01$. It happens because the 2D mesh is too coarse near the origin, whereas the computationally cheaper 1D solver allows to use a sufficiently refined mesh.

In case of azimuthal growth we know that for an infinitely thin film, the geometrical solution is (3.8) and therefore the radial derivative of numerical solution should tend to

$$\zeta_{,r} = \pm 2\sqrt{\frac{k}{n^2-1}}\sin(n\theta+\theta_0), \quad \phi = \zeta_{,r}/\sqrt{2k} = \pm\sqrt{\frac{2}{n^2-1}}\sin(n\theta+\theta_0). \quad (7.11)$$

According to Figure 7.2 we can conclude that in our case $n = 2$. The scaled

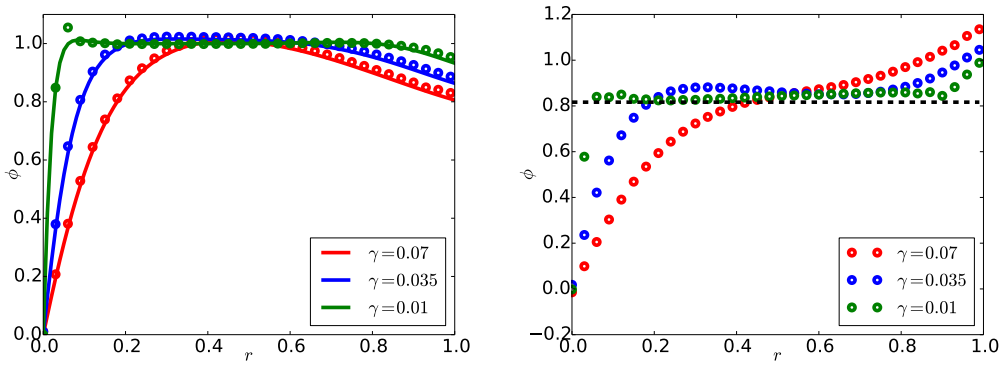

(a) (b)

Figure 7.3: (a) Scaled derivative $\phi = \zeta_{,r}/\sqrt{2k}$ of deflection obtained by 1D (solid) and 2D (markers) solvers for 10% radial growth and three different values of thickness (0.07, 0.035 and 0.01 cm). (b) Scaled radial derivative $\phi = \zeta_{,r}/\sqrt{2k}$ of deflection in the case of 10% azimuthal growth and angle θ given by $n\theta + \theta_0 = \pi/2$.

radial derivatives of the numerical solution is depicted in Figure 7.3-(b) for angle θ such that $n\theta + \theta_0 = \pi/2$, together with geometrical solution (7.11) (dashed line). Similarly to the case of radial growth, we also have boundary and corner layers whose widths decreases as the biofilm thickness does.

7.2 Comparison between different types of finite elements

Test cases 1 and 2 use Zienkiewicz elements for simulation which are not conformed since first derivatives may have discontinuities between elements. Next two test cases are devoted to solution of the similar cone and saddle examples using conformed Hseih-Clough-Tocher (HCT) elements. Results for test case 3 and 4 corresponding to thickness $h = 0.035$ cm are depicted in Figure 7.4. Easy to see that we have quite similar cone and saddle shapes. In order to make more precisely analysis we compare cross sections of radial derivatives of ζ obtained thereby Zienkiewicz and HCT elements. These results are depicted in Figure 7.5, solid lines corresponds to Zienkiewicz elements whereas markers represent HCT elements. We can conclude thus that there is no needs in usage of HCT element, which requires more computations during the integration, so all further simulation we will perform using Zienkiewicz element.

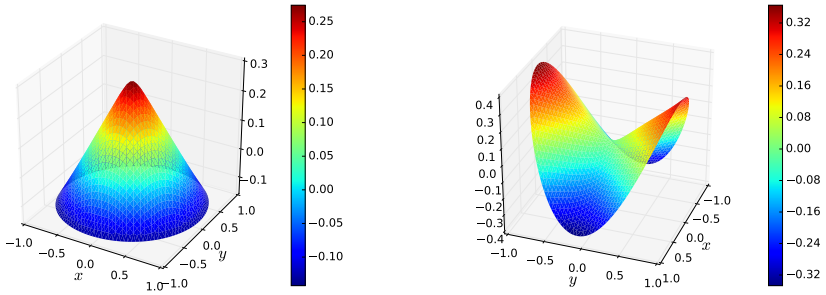

(a) (b)

Figure 7.4: (a) 10% radial growth of film with thickness $h = 0.035$ cm simulated using HCT elements, (b) 10% azimuthal growth of film with thickness $h = 0.035$ cm.

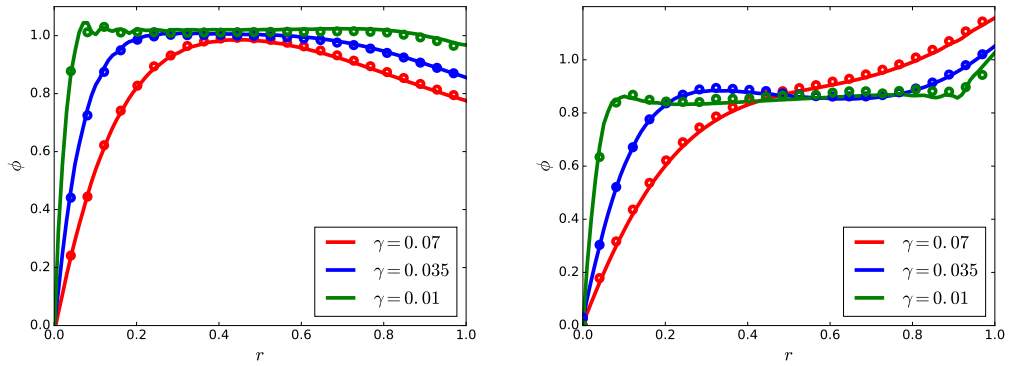

(a) (b)

Figure 7.5: (a) Scaled derivative $\phi = \zeta_{,r}/\sqrt{2k}$ of deflection obtained by 2D solution using Zienkiewicz (solid line) and HCT (markers) elements for 10% radial growth and three different values of thickness (0.07, 0.035 and 0.01 cm). (b) Scaled radial derivative $\phi = \zeta_{,r}/\sqrt{2k}$ of deflection in the case of 10% azimuthal growth and angle θ given by $n\theta + \theta_0 = \pi/2$.

7.3 Comparison between different solvers

All previous examples assume that the layer is purely viscous. What happen if the substratum is viscoelastic? The theory predicts that elasticity of the agar layer decreases deflection of the biofilm from flat state and increases frequency of wrinkles. These expectations are confirmed by numerical experiment depicted in Figure 7.6 related to test case 6 from table 7.2. Easy to see that for stiffer substrate the final shape contains more folds: for film

with thickness $h = 0.07$ cm we can see 4 folds when $\mu_\infty = 25$ Pa whereas for higher $\mu_\infty = 25$ Pa there are 5 folds. Furthermore the thinner is film the higher is influence of the substratum since its deformation energy is bigger than bending energy of the film.

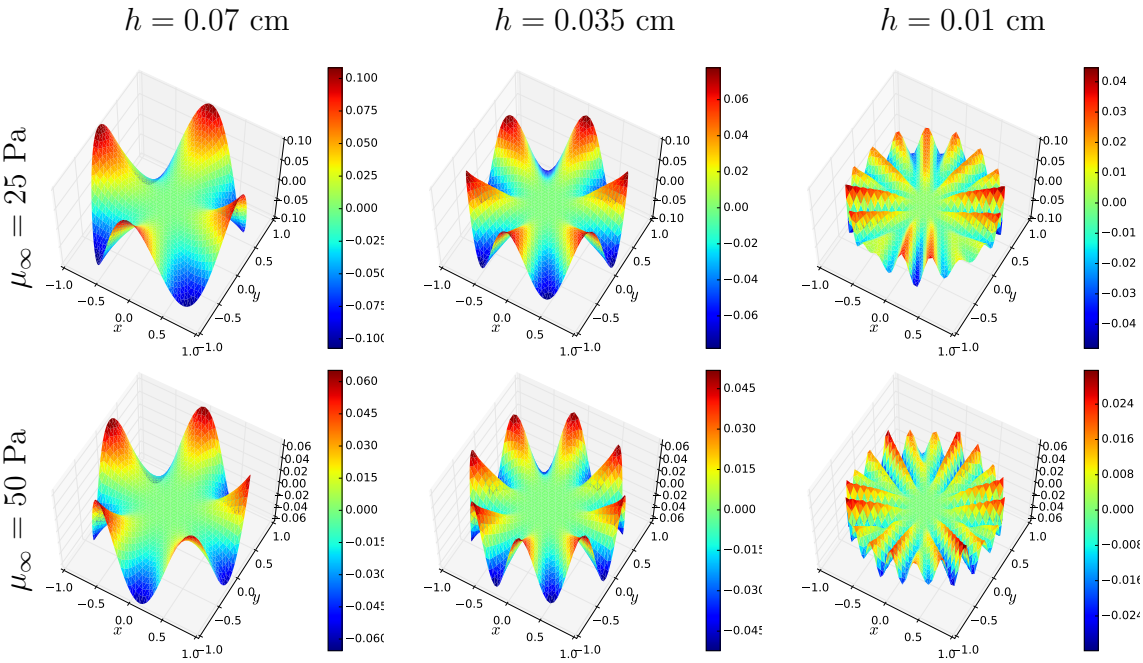

Figure 7.6: 10% azimuthal growth of films with thickness form $h = 0.01$ cm (right) to $h = 0.07$ cm (left) on a viscoelastic layer with $\mu_\infty = 25$ Pa and $\mu_\infty = 50$ Pa. Solution for AF given by (7.9)-(7.10).

Similar effect can be seen for cone solution depicted in Figure 7.7 which correspond to test case 5 from table 7.2. Again we can see increment of frequency of concentric folds and decrement of their amplitude. However, it is possible to note, that alteration of thickness makes much greater impact to the shape of solution than changing of substratum stiffness.

When a stiff substratum is presented the simplified Airy potential formulation (AF) (7.9)-(7.9) is not completely correct and we have to use general formulation (GF) (7.7)-(7.8). However when μ_∞ tends to 0 both formulations are equivalent and since AF is computationally cheaper it is interesting to find a threshold until which we can use this formulation without large error. In Figure 7.8 cross section of conical solution on different substrata and for different thicknesses are presented. Solid lines correspond to solutions of AF (7.9)-(7.10) and markers depict solutions of GF (7.7)-(7.8). The Figure 7.8 shows that there is almost no difference between general and simplified

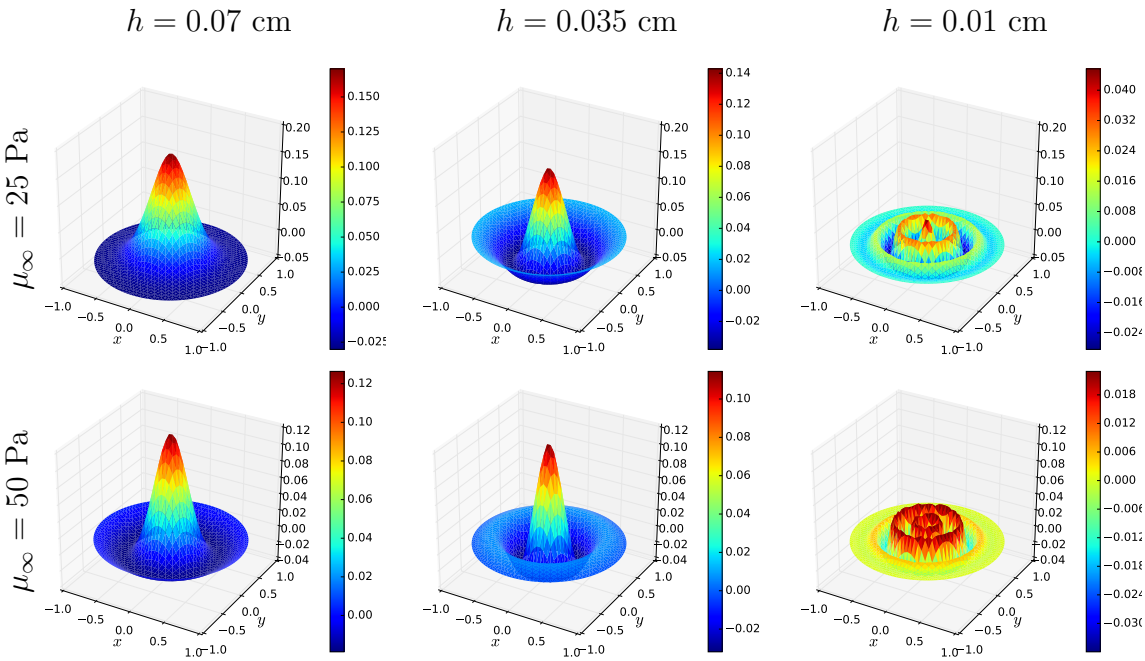

Figure 7.7: 10% radial growth of films with thickness form $h = 0.01$ cm (right) to $h = 0.07$ cm (left) on a viscoelastic layer with $\mu_\infty = 25$ Pa and $\mu_\infty = 50$ Pa. Solution for AF given by (7.9)-(7.10).

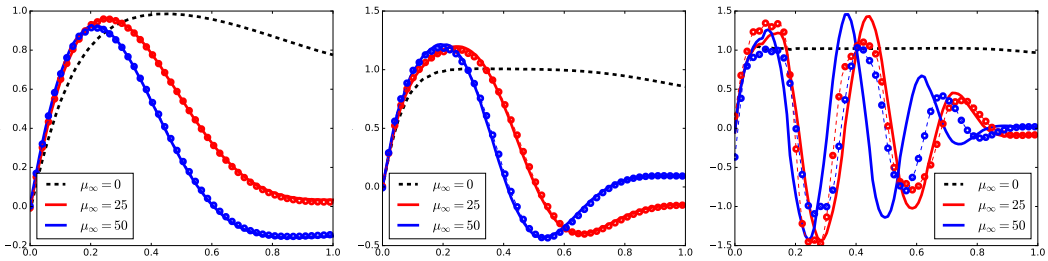

(a) (b) (c)

Figure 7.8: 10% radial growth of films with thickness (a) $h = 0.07$ cm, (b) $h = 0.035$ cm, (c) $h = 0.01$ cm and different stiffness of the substratum. Solid lines represent solution of simplified AF (7.9)-(7.10), markers corresponds to solution of GF (7.7)-(7.8).

systems for thick films, plots (a) and (b), whereas for thin film AF gives incorrect solution even for relatively soft substratum. We can conclude thus the thickness of the film is more sensitive parameter than stiffness of the agar layer, that is quite natural since μ_∞ enters into the equations (7.1)-(7.2) lin-

early whereas h contributes in 3rd power. For sinusoidal wrinkles this effect was noted by Chen and Hutchinson (2004). In that case it is even possible to calculate wave number of wrinkles

$$\lambda = 2\pi h \left(\frac{E}{3E_s} \right)^{1/3}. \tag{7.12}$$

It means that if we want to increase frequency of wrinkles 2 times we have decrease 2 times thickness h of biofilm or increase 8 times stiffness μ_∞ of the substratum. Proportion given in formula (7.12) can be used even in case when wrinkles are not sinusoidal as for example ones depicted in Figure 7.6. Indeed if we change substratum stiffness from $\mu_\infty = 25$Pa to $\mu_\infty = 50$Pa number of wrinkles increase from 4 to 5 for film with thickness $h = 0.07$ cm and from 6 to 8 for film with thickness $h = 0.035$ that is approximately $2^{1/3}$ times. On the other hand when the thickness of film decrease 2 times (from 0.07 cm to 0.035 cm) the number of wrinkles growth from 4 to 6 and from 5 to 8 for stiff and soft substrata respectively. The fact the frequency grows less than 2 times in this case can be explained by that wrinkles in this example are not sinusoidal.

The 3D shape of solutions of general system (7.7)-(7.8) are depicted in Figure 7.9 for different thicknesses, different growth, and rubbery modulus $\mu_\infty = 50$ Pa. These test cases have numbers 7 and 8 in table 7.2 and it is possible to see they are quite similar to test cases 5 and 6 calculated using AF (7.9)-(7.10).

The verification proceeded in this chapter demonstrates that:

- developed numerical algorithm provides results which coincides with theory in cases when analytical solution is known;
- even though Zienkiewicz elements are not conformed they provides similar solution that conformed HCT elements and besides are computationally cheaper;
- in cases of soft substratum and thick film we can use simplified AF (7.9)-(7.10) without any restrictions whereas if the biofilm gets thinner or the agar layer stiffer we should to use general formulation (7.7)-(7.8).

7.4 Heterogeneous growth of a round film

We have verified our numerical solver on a few simple test cases so now we can consider more complex examples. In all previous sections growth was homogeneous in polar coordinates but what happens if we set heterogeneous

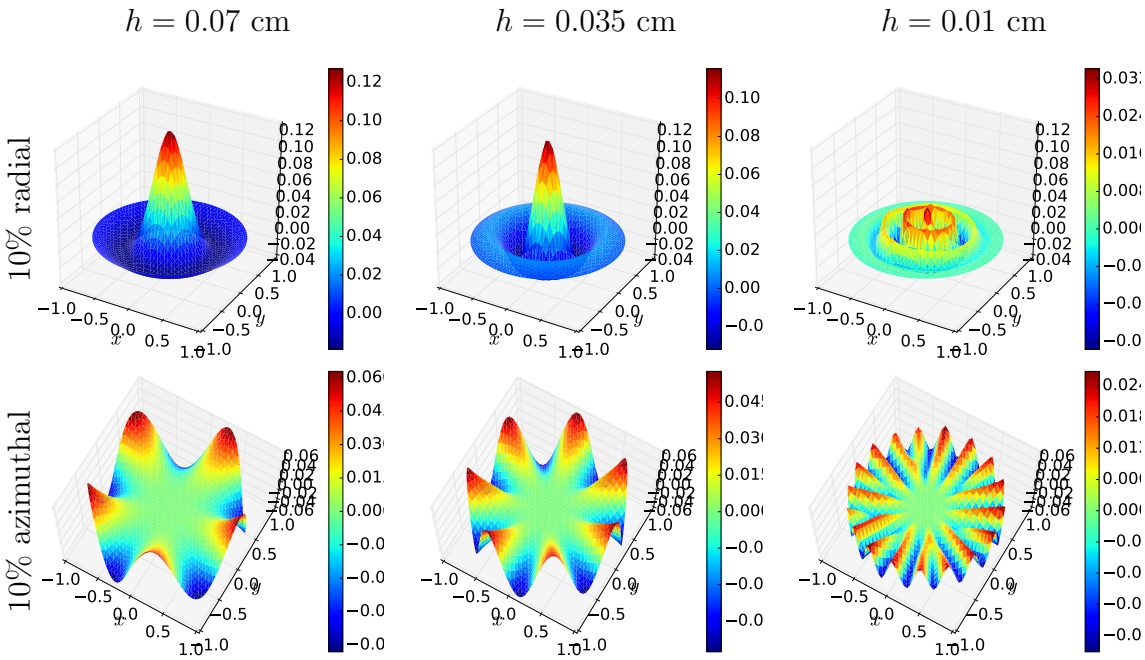

Figure 7.9: 10% radial and azimuthal growth of films with thickness form $h = 0.01$ cm (right) to $h = 0.07$ cm (left) on a viscoelastic layer with $\mu_\infty = 50$ Pa. Solution is obtained for GF (7.7)-(7.8).

growth? This is the issue two following examples are devoted to. In the first one we consider anisotropic heterogeneous growth given in polar coordinates by formula

$$g_r^{(1)} = \begin{cases} 0.2, & \sqrt{x^2+y^2} < 0.7, \\ 0, & \text{otherwise;} \end{cases} \quad g_\theta^{(1)} = \begin{cases} 0, & \sqrt{x^2+y^2} < 0.7, \\ 0.2, & \text{otherwise.} \end{cases} \tag{7.13}$$

It means that the center of biofilm grows radially whereas outer rim grows azimuthaly with the same rate. In the second example we also consider heterogeneous growth but now it will isotropic:

$$g_r^{(2)} = g_\theta^{(2)} = \begin{cases} 0.1, & \sqrt{x^2+y^2} < 0.5, \\ 0.2, & \text{otherwise,} \end{cases} \tag{7.14}$$

that is center of biofilm grows slowly than the outer rim. Similarly to previous sections we will consider growth of round biofilm with homogeneous properties. Test cases for this sections are provided in table 7.3.

In Figure 7.10 solutions for test case 9 are depicted. Obtained result repeats one of Iakunin and Bonilla (2018) that is we have a mixture of solutions

#	growth type	substratum	thickness
9	1	pure viscous	$h = 0.07,\ 0.035,\ 0.01$ cm
10	1	$\mu_\infty = 150$Pa	$h = 0.07,\ 0.035,\ 0.01$ cm
11	2	pure viscous	$h = 0.07,\ 0.035,\ 0.01$ cm
12	2	$\mu_\infty = 150$Pa	$h = 0.07,\ 0.035,\ 0.01$ cm

Table 7.3: Test cases for heterogeneous growth. Young modulus of the biofilm for all cases is 25 kPa, radius of biofilm is 1 cm, thickness of agar substratum and its Poisson ratio are 0.7 cm and 0.45. First growth type corresponds to the growth given by formula (7.13) and the second one to (7.14).

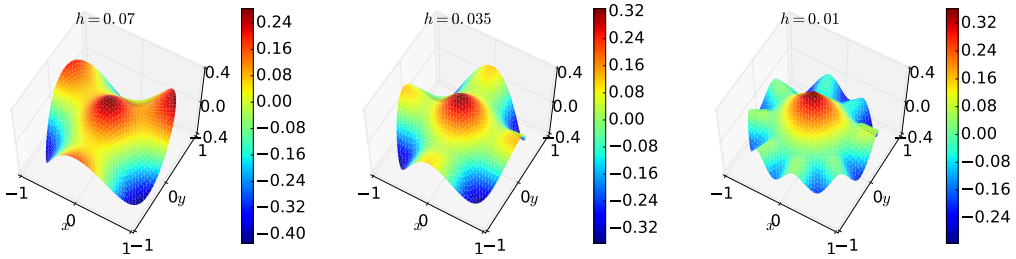

(a) (b) (c)

Figure 7.10: Heterogeneous anisotropic growth defined by formula (7.13) of a round biofilm of thickness (a) $h = 0.07$ cm, (b) $h = 0.035$ cm, (c) $h = 0.01$ cm on a pure viscous substratum.

for a mixture of different growth types: near the origin the solution is a cone (radial growth) but it bends into a corona for the azimuthal growth near the boundary. The number of folds increases when the thickness of biofilm decreases: 3 folds for $h = 0.01$ cm, 4 folds for $h = 0.035$cm, and 10 folds for $h = 0.01$. If we add a stiff substratum the frequency of wrinkles will also increase as it shown in Figure 7.11 corresponding to test case 10. Besides it is possible to note that the smaller is frequency of wrinkles the higher their amplitude is. The connection between frequency and amplitude according to Cerda et al. (1997) shows that we have geometrically nonlinear deformation.

Solution for test cases 11 and 12 related to heterogeneous isotropic growth are depicted in Figure 7.12 and Figure 7.13 respectively. If the agar layer below the biofilm is purely viscous we do not have any wrinkles even though the deflection is quite large (Figure 7.12). When the substratum is stiff the situation changes dramatically. For relatively thick biofilms ($h = 0.07$ cm and $h = 0.035$ cm) the solution is almost flat whereas for thin colony ($h = 0.01$ cm) we obtain a network of wrinkles quite similar to one which is

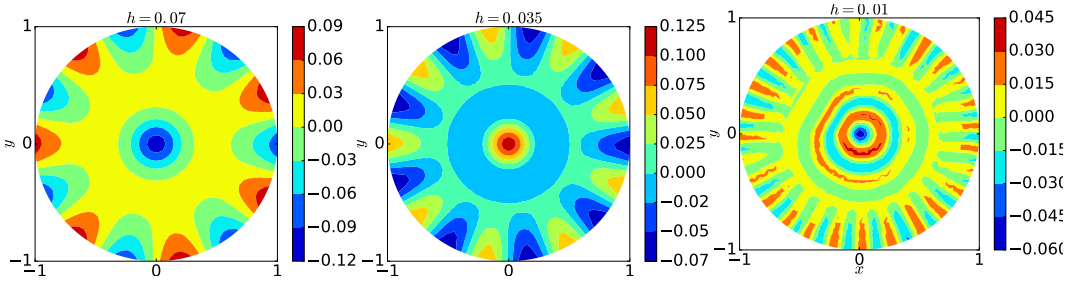

Figure 7.11: Heterogeneous anisotropic growth defined by formula (7.13) of a round biofilm of thickness (a) $h = 0.07$ cm, (b) $h = 0.035$ cm, (c) $h = 0.01$ cm on a agar with rubbery modulus $\mu_\infty = 150$Pa.

possible to see in experiments, Hobley et al. (2015). Besides it is possible to see branching of wrinkles similar to one obtained by Zhang et al. (2016). According to that paper this effect also allows to decrease deformation energy since branching of wrinkles stops increment of frequency.

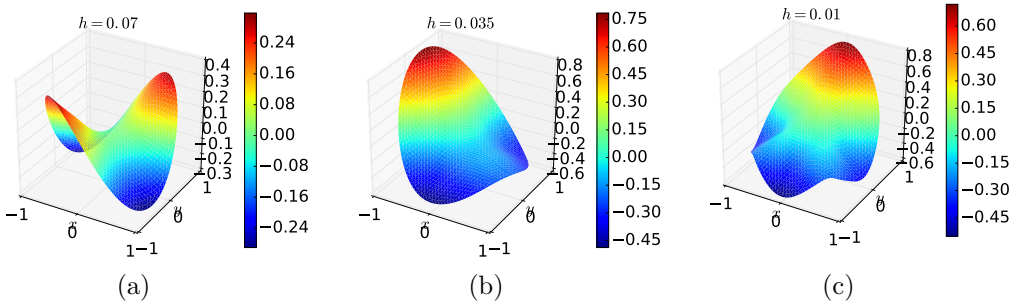

Figure 7.12: Heterogeneous anisotropic growth defined by formula (7.13) of a round biofilm of thickness (a) $h = 0.07$ cm, (b) $h = 0.035$ cm, (c) $h = 0.01$ cm on a agar with rubbery modulus $\mu_\infty = 150$Pa.

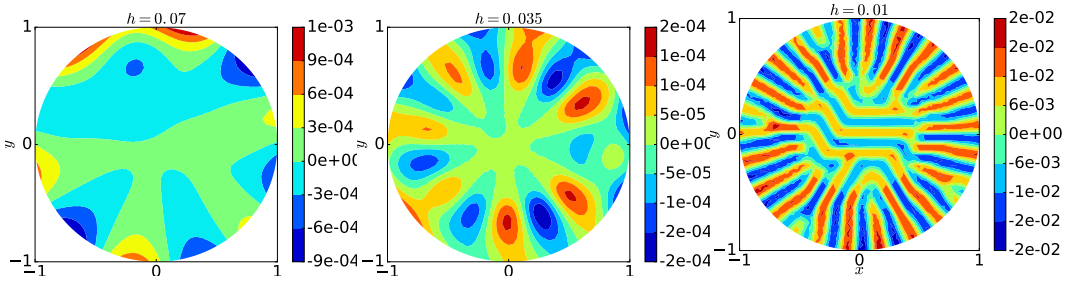

(a) (b) (c)

Figure 7.13: Heterogeneous anisotropic growth defined by formula (7.13) of a round biofilm of thickness (a) $h = 0.07$ cm, (b) $h = 0.035$ cm, (c) $h = 0.01$ cm on a agar with rubbery modulus $\mu_\infty = 150$Pa.

Chapter 8

Bifurcation analysis

In this chapter we will study two bifurcation cases related to critical growth and critical substratum stiffness. In the first case, there is no viscoelastic substratum and we have a scalar growth tensor that departs from identity as a function of the radius. As its intensity ε increases, the flat solution of the nonlinear MAE becomes unstable and the film buckles. We have observed two bifurcation values of ε. At its lowest value, the bifurcation is subcritical and there is a hysteresis region in an interval of ε values. In this interval, numerical simulations show that both the flat solution and a buckled solution with radial symmetry are stable. At a larger value of ε, the buckled solution loses radial symmetry and a solution with more complex ripples appears. This second bifurcation is numerically observed to be supercritical, as there is a continuous transition from radial to non-radial symmetry. The second example of bifurcation is due to the interaction with the viscoelastic substratum. We have shown in chapter 5 that if the agar is purely viscous, then homogeneous isotropic growth is compatible and the film remains flat. However for a viscoelastic substratum, the rubbery modulus reaches a critical value beyond which wrinkles appear. Thus, even compatible growth can provoke wrinkles for a sufficiently stiff viscoelastic substratum. In comparison to the case of heterogeneous growth without viscoelastic substratum, internal growth is not a source of wrinkles by itself but becomes it provokes wrinkles in combination with a viscoelastic agar layer that prevents enlargement of the biofilm and forces it to buckle.

8.1 Bifurcation respect to heterogeneous growth on a pure viscous substratum

Let us consider isotropic heterogeneous growth $\mathbf{g} = g(x, y)\mathbf{I}$ of a circular homogeneous film with radius $R = 1$cm, thickness $h = 0.03$cm, and Young modulus $E = 25000$Pa in the absence of agar substratum. Here $\mathbf{I}$ is identity tensor and function $g(x, y)$ depends only on radial coordinate $r = \sqrt{x^2 + y^2}$:

$$g(x, y) = g(r) = \varepsilon \sin(\omega r), \tag{8.1}$$

where ε and ω are parameters. Since the substratum is purely viscous there is no need in general formulation and we can use simplified Airy potential system which in this case after nondimensionalization can be written as

$$\frac{\partial \zeta}{\partial t} = -\frac{(1-2\nu)\kappa^2}{2(1-\nu)} \left(\frac{1}{9\kappa^2} \Delta^2 \zeta - 2\,[\chi, \zeta] \right), \tag{8.2}$$

$$\Delta^2 \chi + [\zeta, \zeta] = -\Delta g, \tag{8.3}$$

where $\nu = 0.45$ is Poisson ration of agar layer and g is given by .

One can check easily that the given growth is not compatible therefore we can expect bending and wrinkling of the biofilm. However there always is a flat solution since $\zeta = 0$ solves (8.2) and (8.3) has a unique solution respect to χ (see chapter 5). This solution can be found quite easily. Indeed, if $\zeta = 0$ the second equation turns into

$$\Delta^2 \chi = -\Delta g = \varepsilon \left(\omega^2 \sin(\omega r) - \frac{\omega}{r} \cos(\omega r) \right) \tag{8.4}$$

which is linear and equipped with boundary conditions $\chi|_{r=1} = \chi_{,r}|_{r=1} = 0$ have a solution

$$\chi(r) = \frac{\varepsilon}{\omega^2} \left(\omega \sin(\omega r) - \int_0^r \frac{1}{\rho} \sin(\omega \rho) d\rho + \frac{r^2}{2} (\sin \omega - \omega \cos \omega) + c \right), \tag{8.5}$$

where c is chosen to set $\chi|_{r=1} = 0$. The Airy potential and stresses increase when the growth amplitude ε increases. In order to figure out when flat solution is not stable we use linear stability analysis. Assume that $\zeta(t, x, y) = e^{\lambda t} \eta(x, y)$ and consider the equation (8.2) where we plug Airy potential χ for (8.4):

$$\frac{\partial \zeta}{\partial t} = -\frac{(1-2\nu)\kappa^2}{2(1-\nu)} \left(\frac{1}{9\kappa^2} \Delta^2 \zeta - 2[\zeta, \chi] \right). \tag{8.6}$$

This equation turns to an eigenvalue problem respect to λ and η:

$$\lambda\eta = -\frac{(1-2\nu)}{18(1-\nu)}\Delta^2\eta + \frac{(1-2\nu)\kappa^2}{(1-\nu)}[\eta,\chi], \tag{8.7}$$

and the flat solution is unstable if operator on the right hand side has positive eigenvalues. If χ is small all possible λ-s are negative since the bilaplacian is positive definite. However for larger ε the term $\Delta^2\eta$ can be canceled by brackets $[\eta,\chi]$ providing zero or positive λ and non flat stable solution.

It is impossible to solve problem (8.7) analytically so we will solve numerically the equations. We choose $\omega = 30$ and start from random initial condition and small $\varepsilon = 0.06$. As we raise ε in small increments, we use the solution obtained for the previous value of ε as the initial condition for the new one. First bifurcation point depicted in Figure 8.1 corresponds to $\varepsilon \approx 0.08$. At this value, the biofilm buckles from the flat state to a radially symmetric conical shape. The second bifurcation point is close to $\varepsilon = 0.128$ and corresponds to loss of radial symmetry. The shapes on a neighborhood of this bifurcation point are depicted in Figure 8.2. They are quite similar to each other but the azimuthal derivatives $\zeta_{,\theta}$ depicted in Figure 8.3 change dramatically. Beyond this second bifurcation point, the deflection starts to growth quite rapidly and the final shape becomes more and more asymmetric, as depicted in Figure 8.4.

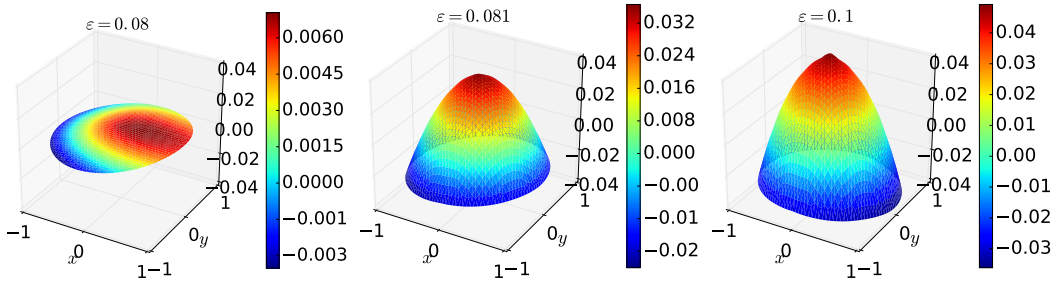

(a) (b) (c)

Figure 8.1: Growth defined by (8.1) of a circular biofilm of thickness $h = 0.03$ cm and Young modulus $E = 25$kPa. Here $\omega = 30$ and ε takes different values (a) $\varepsilon = 0.08$ (b) $\varepsilon = 0.081$ (c) $\varepsilon = 0.1$.

The two previously mentioned bifurcation points can be easily visualized by plotting the bending energy of the biofilm versus the growth intensity ε. In Figure 8.5(a), the blue line corresponds to increasing growth and the red one to decreasing growth. When ε surpasses the first critical value the flat solution becomes unstable and the new buckled solution becomes stable. If we

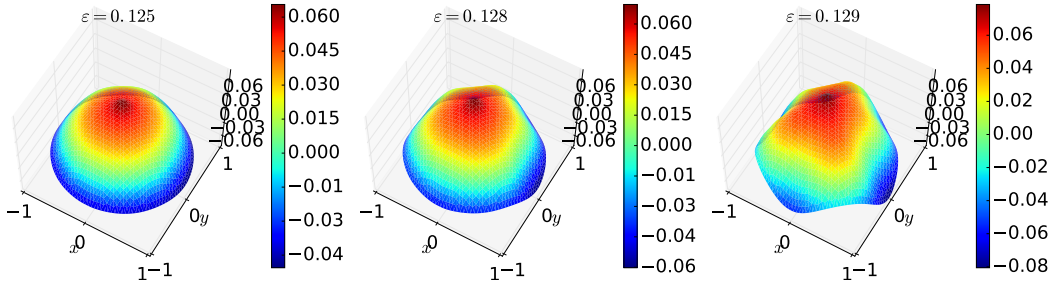

Figure 8.2: Growth defined by (8.1) of a circular biofilm of thickness $h = 0.03$ cm and Young modulus $E = 25$kPa. Here $\omega = 30$ and ε takes different values (a) $\varepsilon = 0.12$ (b) $\varepsilon = 0.128$ (c) $\varepsilon = 0.129$.

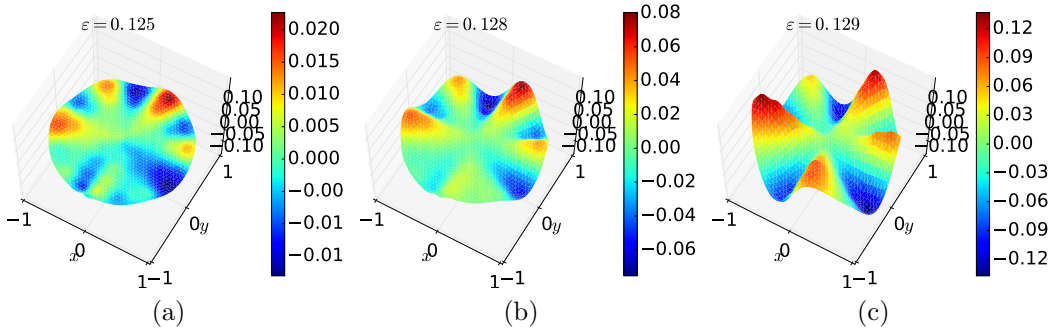

Figure 8.3: Azimuthal derivative $\zeta_{,\theta}$ of vertical deflection calculated for growth defined by (8.1) and circular biofilm with thickness $h = 0.03$ cm and Young modulus $E = 25$kPa. Here $\omega = 30$ and ε takes different values (a) $\varepsilon = 0.12$ (b) $\varepsilon = 0.128$ (c) $\varepsilon = 0.129$.

then ε decreases, we stay on the branch of buckled solutions until $\varepsilon = 0.02$, at which value the stable configuration is again the flat film. Therefore there is a hysteresis loop for ε between 0.02 and 0.08. In Figure 8.5(b) we compare the total mechanical energy of the flat state with that of the bucked configurations depicted in Figures 8.1 – Figure 8.2. We can note that it is almost impossible to distinguish the first bifurcation point in Figure 8.5(b) because the bending energy is very small comparing with the stretching one. However after the second bifurcation point, the bending energy starts to growth until it becomes comparable with the stretching one (for $\varepsilon = 0.3$). Nevertheless, the total mechanical energy of the wrinkled film is never greater than that of the flat film.

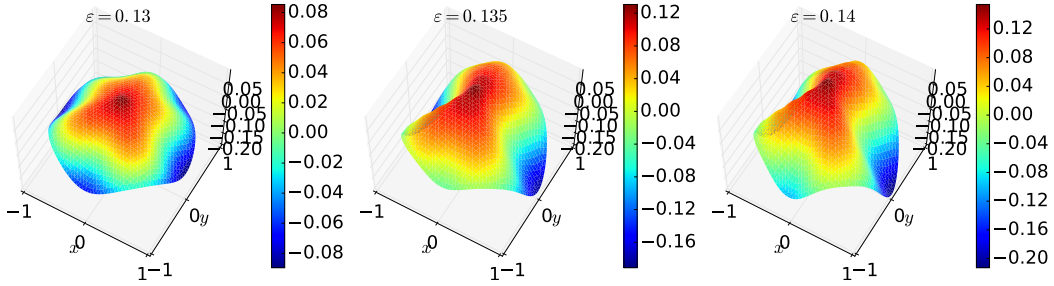

Figure 8.4: Growth defined by (8.1) of a circular biofilm with thickness $h = 0.03$ cm and Young modulus $E = 25$kPa. Here $\omega = 30$ and ε takes different values (a) $\varepsilon = 0.13$ (b) $\varepsilon = 0.135$ (c) $\varepsilon = 0.14$.

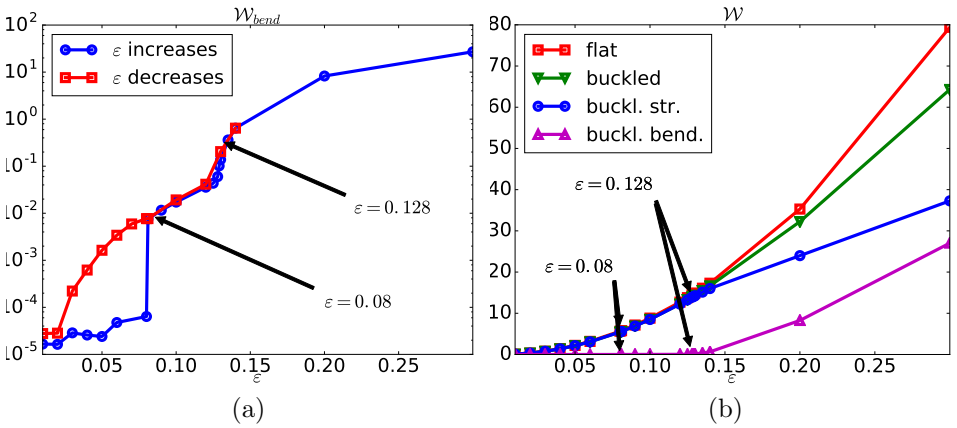

Figure 8.5: Scaled (a) bending energy and (b) total mechanical energy of circular biofilm with thickness $h = 0.03$ cm and Young modulus $E = 25$kPa undergoing growth defined by (8.1). Here $\omega = 30$ and ε takes different values, "buckl. bend." and "buckl. str." stay for bending and stretching energy in the buckled state respectively, arrows indicate bifurcation points.

We can also compare analytical values of principle stresses (eigenvalues of stress tensor) calculated for flat biofilm with ones obtained by solving the problem (8.2)-(8.3) for different ε numerically. According to definition of

Airy potential radial and azimuthal stress are given:

$$\sigma_{rr} = \frac{E\varepsilon}{h\omega^2}\left(\omega\left(\frac{\cos(\omega r)}{r} - \cos\omega\right) - \frac{\sin(\omega r)}{r^2} + \sin\omega\right), \tag{8.8}$$

$$\sigma_{\theta\theta} = \frac{E\varepsilon}{h\omega^2}\left(\left(\frac{1}{r^2} - \omega^2\right)\sin(\omega r) - \frac{\omega}{r}\cos(\omega r) + (\sin\omega - \omega\cos\omega)\right), \tag{8.9}$$

$$\sigma_{r\theta} = -\frac{E}{h}\frac{\partial}{\partial r}\left(\frac{1}{r}\frac{\partial\chi}{\partial\theta}\right) = 0. \tag{8.10}$$

Since stress tensor is diagonal principle stresses can be calculate as

$$\sigma_1 = \max\{\sigma_{rr}, \sigma_{\theta\theta}\}, \quad \sigma_2 = \min\{\sigma_{rr}, \sigma_{\theta\theta}\}. \tag{8.11}$$

These values together with numerical results are depicted in Figure 8.6 (by solid lines and markers respectively). It is possible to see that for small growth numerical approximation of stress coincides with analytic result for flat film given by (8.8)-(8.10). That makes sense because the final numerical solution is also flat as it is depicted in Figure 8.1. However for relatively large $\varepsilon = 0.3$ the solution is not flat (Figure 8.2) and calculated stresses are much smaller then ones obtained for flat configuration. It verifies the idea explained by Cerda and Mahadevan (2003) that thin films wrinkle in order to cancel their stretching stresses.

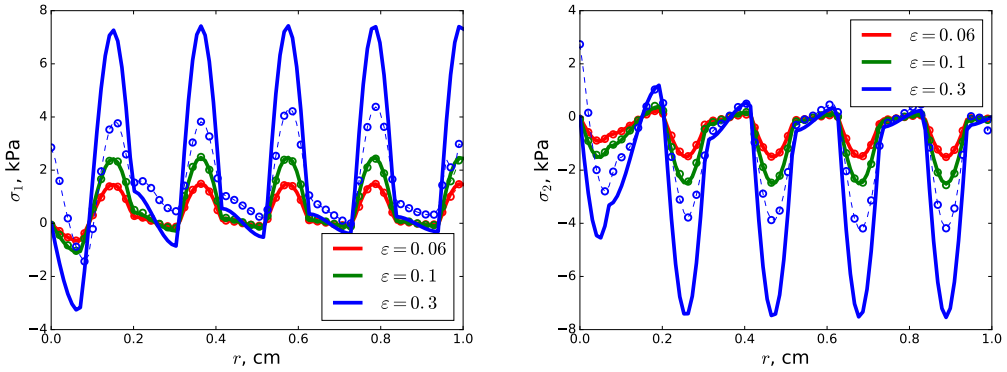

(a) (b)

Figure 8.6: Cross section of first (a) and second (b) principle stresses (eigenvalues of stress tensor) computed for biofilm with thickness $h = 0.03$ cm, Young modulus $E = 25$ kPa which undergoes growth given by (8.1) with $\omega = 30$. Solid lines represent analytical value for flat film and markers corresponds to numerical result for flat (in cases of $\varepsilon = 0.06$ and $\varepsilon = 0.1$) and wrinkled (in case $\varepsilon = 0.3$) film.

8.2 Bifurcation in case of compatible growth respect to stiffness of agar lager

Another interesting bifurcation case is related to interaction with agar substratum. Let us consider a circular homogeneous biofilm with radius $R = 1$cm which undergoes homogeneous isotopic growth given by

$$\mathbf{g} = g\mathbf{I}, \tag{8.12}$$

where $g = 0.1$. If the substratum is pure viscous we can use Airy potential formulation and write that

$$\frac{\partial \zeta}{\partial t} = -\frac{(1-2\nu)\kappa^2}{2(1-\nu)}\left(\frac{1}{9\kappa^2}\Delta^2\zeta - 2\left[\chi,\zeta\right]\right), \tag{8.13}$$

$$\Delta^2\chi + [\zeta,\zeta] = 0. \tag{8.14}$$

The system (8.13)-(8.14) has a pair $\zeta = 0$, $\chi = 0$ as its solution thus if the film undergoes growth given by (8.12) it will always maintain flat (this effect was predicted in theory since this growth is compatible). Airy potential χ is also 0 hence there are no stretching stresses and for in-plane displacement we can write a system

$$\sigma_{rr} = \frac{2E}{3}\left(2\frac{du_r}{dr} + \frac{u_r}{r} - 3g\right) = \sigma_{\theta\theta} = \frac{2E}{3}\left(\frac{du_r}{dr} + 2\frac{u_r}{r} - 3g\right) = 0, \tag{8.15}$$

$$\sigma_{r\theta} = \frac{E}{3}\left(\frac{du_\theta}{dr} - \frac{u_\theta}{r}\right) = 0, \tag{8.16}$$

where u_r and u_θ are radial and azimuthal components of in-plane displacement and radial symmetry of the problem is supposed. Easy to see that $u_r = gr$ and $u_\theta = 0$ solve the system (8.15) - (8.16) that is compatible growth on a pure viscous substrate provides only in-plane enlargement conformed by this growth.

What happens if the substratum is viscoelastic? In this case we already cannot use the simplified formulation and should write equations in general form:

$$\frac{\partial \zeta}{\partial t} = -\beta\zeta - \frac{(1-2\nu)\kappa^2}{2(1-\nu)}\left(\frac{1}{9\kappa^2}\Delta^2\zeta - \nabla\cdot\left(\boldsymbol{\sigma}^{(0)}\cdot\nabla\zeta\right)\right), \tag{8.17}$$

$$\nabla\cdot\boldsymbol{\sigma}^{(0)} = \gamma^2\beta\mathbf{u}, \tag{8.18}$$

where β is given by (3.39) and is proportional to the rubbery modulus μ_∞ of the agar that is to its stiffness. We control the parameter β representing

ratio between stiffness of agar and one of the biofilm thereby alteration of the value μ_∞ which we select as a bifurcation parameter. Flat solution $\zeta = 0$ still resolves first equation (8.17) however the second equation (8.18) changes due to the right hand side is proportional to β. If we plug $\zeta = 0$ and assume radial symmetry this equation can be rewritten as

$$r^2 \frac{d^2 u_r}{dr^2} + r \frac{du_r}{dr} - \left(1 + r^2 \frac{\gamma^2 \beta}{2}\right) u_r = 0, \tag{8.19}$$

where $u_r(r)$ is scaled radial component of in-plane displacement, $u_\theta(r) = 0$. Equation (8.19) is modified Bessel equation and after applying boundary conditions

$$u_r(0) < \infty, \quad \sigma_{rr}|_{r=1} = \left(2\frac{du_r}{dr} + \frac{u_r}{r} - 3g\right)\Big|_{r=1} = 0,$$

we obtain that

$$u_r(r) = \frac{3gI_1(\alpha r)}{2\alpha I_0(\alpha) - I_1(\alpha)}, \quad \alpha = \gamma\sqrt{\beta/2}, \tag{8.20}$$

where $I_n(x)$ is modified Bessel function of the first kind. One can easily check that the substratum is purely viscous that is the bifurcation parameter μ_∞ tends to 0 so β tends to 0 and hence α tends to 0 the solution (8.20) becomes $u_r(r) = gr$ that coincides with the solution for pure viscous substratum. For stiff substratum that for large values of bifurcation parameter μ_∞ we expect emergence of wrinkles.

In order to check when the flat solution becomes unstable we will use linear stability analysis similarly to the previous section. Assume that vertical deflection is $\zeta(t, x, y) = e^{\lambda t}\eta(x, y)$ and in-plane displacements has only radial component given by (8.20). Then equation (8.13) turns into eigenvalue problem for λ and η:

$$\begin{aligned}(\lambda + \beta)\eta = -\frac{(1-2\nu)\kappa^2}{2(1-\nu)}\Bigg(&- \frac{1}{18\kappa^2}\Delta^2\eta + \\ &\frac{2}{3}\Big(\frac{1}{r}\frac{\partial}{\partial r}\left(r\left(2\frac{du_r}{dr} + \frac{u_r}{r} - 3g\right)\eta_{,r}\right) + \\ &\frac{1}{r^2}\left(\frac{du_r}{dr} + 2\frac{u_r}{r} - 3g\right)\eta_{,\theta\theta}\Big)\Bigg),\end{aligned} \tag{8.21}$$

where u_r is given by (8.20). Flat solution is not stable if there is $\lambda \geq 0$ that is eigenvalues of the operator on the right hand side should not be smaller

than β. It is impossible to solve problem (8.21) analytically. Furthermore it is not even clear how to show that such eigenvalue exists. However we can find the bifurcation point numerically for 10% growth and film with thickness $h = 0.01$ cm and Young modulus $E = 25000$Pa. We start from relatively small rubbery modulus μ_∞ when the solution is flat and increase the bifurcation parameter until wrinkles emerge (see Figure 8.8). In each simulation we use the result obtained for previous μ_∞ as a initial conditions.

In Figure 8.8 it is possible to see that flat solution becomes unstable for $\mu_\infty \approx 177.25$ Pa and the transition is sudden. Further increment of bifurcation parameter does not provide crucial changes probably until next bifurcation point: there are almost no difference between Figure 8.8(c) and Figure 8.8(d). The transition between flat state and rugose one is clearly seen in the bifurcation diagram for bending energy of the biofilm, Figure 8.7. We can also note that the obtained patterns are quite complex and asymmetric that distinguishes this bifurcation regime with usual buckling when the first shape is simple and symmetric. The phenomena of emergence of complex network of wrinkles is quite common for bilayer structure not only in biofilms but also in many industrial applications, Chen and Hutchinson (2004); Huang et al. (2010).

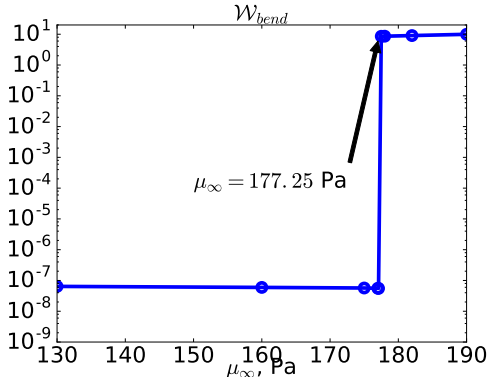

Figure 8.7: Scaled bending energy of circular biofilm with thickness $h = 0.01$ cm and Young modulus $E = 25$kPa undergoing homogeneous isotropic 10% growth on agar substrata with different rubbery modulus μ_∞. Arrow indicates the bifurcation point.

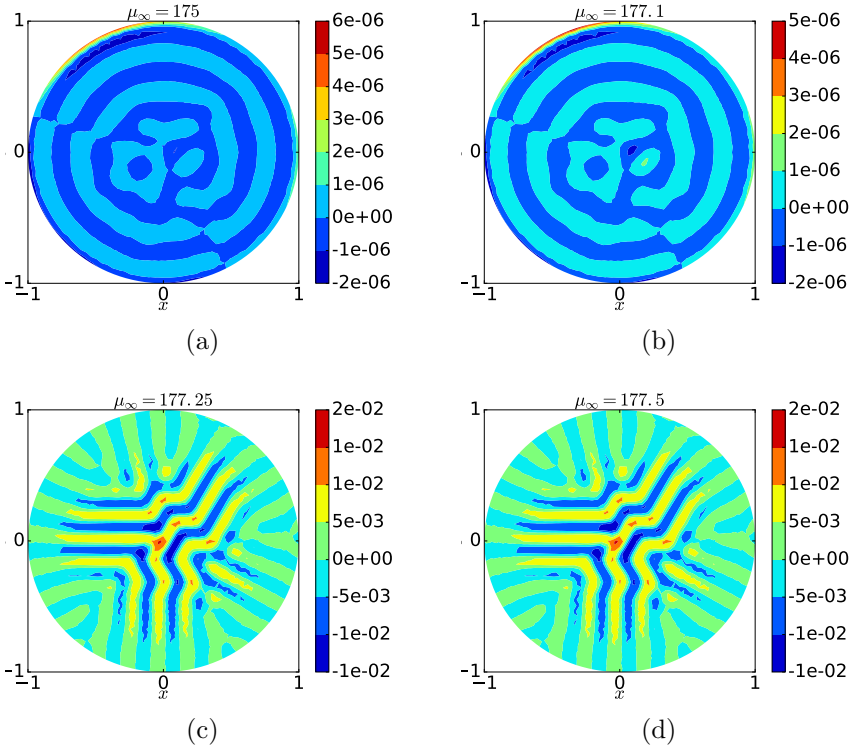

Figure 8.8: Homogeneous isotropic 10% growth of a circular biofilm of thickness $h = 0.01$ cm and Young modulus $E = 25$kPa on a viscoelastic substrate with (a) $\mu_\infty = 175$ Pa, (b) $\mu_\infty = 177.1$ Pa, (c) $\mu_\infty = 177.25$ Pa, (d) $\mu_\infty = 177.5$ Pa

Chapter 9

Conclusions

Formation of wrinkles in bacterial biofilm undergoing growth on an agar substratum (e.g. *Bacillus subtilis*) can be simulated by considering these structure as solid heterogeneous plates bonded to viscoelastic layer. Even though this model is relatively simple and does not include many aspects of behavior of bacteria as cells it yields as results a lot of wrinkling patterns quite similar to ones we can observe in experiments. Furthermore the model can be used for estimation of thickness of corner layer on the edge of wrinkles. Numerical simulation allows us to find bifurcation points corresponding to transition from flat biofilm to a rugose one due to increment of growth factor or due to increment of substratum stiffness. In this chapter we discuss mentioned conclusions in more details and in the end we will formulate open problems related to the present study.

For simulation of biofilm we use Föppl-von Kármán equations (FvKEs) which we moodify including hetergoneity of material, growth following Dervaux et al. (2009), and interaction with the substrtum following Espeso et al. (2015). Proper scaling (Table 3.2) shows that mechanical relaxation in horizontal direction happens much faster than in vertical one. This implies that we can leave only one transient function – vertical (off-plane) displacement ζ. Furthermore, FvKEs are nonlinear only respect to ζ that allows us to express in-plane dispalcements and stresses through vertical deflection leaving thus only one unknown ζ. The procedure of eliminating in-plane displacements is different for viscous and viscoelastic substratum: for visocous agar layer we follow Iakunin and Bonilla (2018) and use Airy potential whereas when agar is viscoelastic we have to solve equations directly in terms of in-plane displacements.

The final simplified equations can be written in weak form as a minimization of a functional respect to ζ that belongs to a Sobolev space. In this functional, we can distinguish three parts: the pure geometrical deformation

of infinitely thin surface; smoother represented by bending energy; and influence of the substratum which tries to cancel large displacements. If we try to minimize only the first term we will note that the solution is unstable and may contain sharp bends and intersections. It happens because the problem of pure geometrical transformation due to growth is ill-posed and has to be regularized by adding constrains or smoothers. Luckily, we have bending energy which regularizes the ill-posed geometrical problem because it does not allow sharp bends. Thus we have a set of well defined, separated solutions from which we should pick one according to the stiffness of the substratum: for pure viscous agar the best one is one with the smallest number of wrinkles and for stiffer agar the deflection amplitude should decrease and frequency increase hence wrinkles emerge.

We note that if we consider pure viscous substratum the geometric part of functional is represented by weak form of Monge-Ampère equation (MAE). In even more simple variation of this case that is for homogeneous radial growth of a round biofilm we perform an asymptotic analysis. For this problem MAE has a conical solution and influence of bending energy term adds a smooth corner layer near the tip and a boundary layer near the rim, which satisfies the incompressibility condition. The thinner the biofilm, the smaller its bending energy is and the thinner these layers are. This analysis thus confirms our expectation that the final shape of biofilm can be obtained as a smoothed solution of MAE and thickness of corner layer coincides with one obtained by Audoly and Pomeau (2010) at that. In general case of biofilm growing on a pure viscous agar we follow Ciarlet and Gratie (2004); Lions (1969) to prove the existence of solution of modified FvKEs if the growth is small enough.

Since it is impossible to find the solution analytically we develop a numerical method based on finite elements. Results of the simulation always coincide with the theoretical predictions. Developed solver allows us to study numerically two interesting bifurcation cases. The first one corresponds to heterogeneous growth of biofilm on a pure viscous substratum. If we start to increase growth factor the film buckles into a simple shape with radial symmetry after certain critical value. Further increment leads to more complex asymmetric shapes. In the second bifurcation case we study influence of the stiffness of the agar layer to emergence of rugose patterns. If the substratum is soft homogeneous growth is compatible and does not provoke any wrinkles. However, if we increase the rubbery modulus μ_∞ of the agar to a certain critical value then a complex network of wrinkle emerges. Thus the presence of stiff substratum allows a quite peculiar behavior: instead of buckling to a simple shape with further complications due to increment of bifurcation parameter we have a sudden wrinkling to a complex asymmetric pattern. These phenomena has place not only in biofilms but also in many industrial

applications where bilayer structures are presented, Chen and Hutchinson (2004); Huang et al. (2010).

9.1 Open problems

The proposed model requires improvements for better description of all features relating to behavior and development of biofilms. In this section we formulate most interesting open questions which may represent topics of our further researches.

- During our study we assumed that the substratum is softer than the biofilm however it is not always true. According to Oyen (2014) rubbery modulus of agar gel may vary from few kPa to 100 kPa that is much stiffer than extracellular matrix. Numerical simulations and theory in this case predict flat solution however in experiments it is possible to see wrinkles even for stiff substratum. To resolve this contradiction probably we should take into account heterogeneity of bacterial colony in vertical direction that is to consider biofilm itself as a mutlilayer structure. This approach was proposed in Wallace (2016) for *Bacillus subtilis* biofilms which according to Hobley et al (2013); Cairns et al (2014) indeed are bilayer. In their researches L. Hobley with coathors note that even though ECM of *Bacillus subtilis* is very soft all colony is covered by extremely thin (order of 1 μm, (Hobley et al (2013))) but quite stiff hydrophobic polymer *BslA*, see Figure 9.1. Thus rugose patterns emergent in *Bacillus subtilis* biofilms may be represented by wrinkles of elastic *BslA* shell covering 3D domain of growing viscoelastic ECM. Furthermore, experiments show that presence of *BslA* is crucial for wrinkles in *Bacillus subtilis* colonies (Hobley et al (2013)). Any quantitative estimation yielding by this model would face troubles in measurements of mechanical properties of *BslA* and the matrix however this approach may provide a good qualitative results. Besides, we can use a diffusion model (for example one proposed by Eberl et al. (2010)) to describe growth of biomass and diffusion of nutrients inside the colony and thus make cellular behavior influential to formation of patterns. Particularly it would be interesting to check if correlation between zone of dead cells and wrinkles seen in experiments by Asally et al. (2012) holds true in this model.

- The bifurcation analysis we do in chapter 8 is pure numeric and is interesting to demonstrate the phenomena but is not enough for its complete understanding. For better studying of stability of the flat

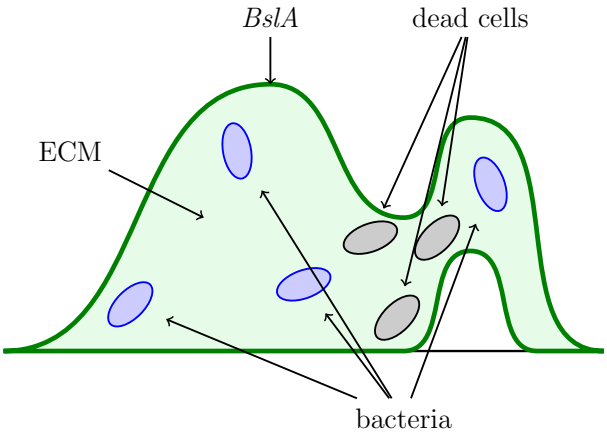

Figure 9.1: Schematic picture of *Bacillus subtilis* biofilm. The colony mostly consists of ECM where dead and alive cells of bacteria are embedded into. From the outside, the biofilm is coverd by thin layer of polymer *BslA*.

solution probably it is useful to find a toy problem (e.g. consider a specific growth) which catches well most of peculiarities of the general problem but can be easily solved analytically. Another way is to develop a special solver for eigenvalue problems arouse from linear perturbation analysis which allows to find bifurcation points rapidly for different types of growth.

- The developed numerical method has a disadvantage: it is necessary to store inverse matrix of stretching energy hessian which is full-populated:

$$\mathbf{A} = \mathbf{B} + \frac{\partial^2}{\partial \boldsymbol{\zeta}^2} \left(\mathbf{l}^T(\boldsymbol{\zeta}) \mathbf{Q}^{-1} \mathbf{l}(\boldsymbol{\zeta}) \right). \tag{9.1}$$

  Here $\mathbf{A}$ is hessian of whole energy functional, $\mathbf{B}$ is linear part corresponding to bending energy and interaction with the substratum, and the second turn corresponds to geometrically nonlinear part and contain full-populated matrix $\mathbf{Q}^{-1}$ which is impossible to store for well refined mesh. This trouble can be resolved by application of iterative solver to matrix $\mathbf{A}$ for which it is not necessary to store whole components but just perform a multiplication $\mathbf{Ax}$ for any vector $\mathbf{x}$. Since this matrix is symmetric and indefinite a good choice would be symmetric LQ (SymmLQ) method discribed in Paige and Saunders (1975). In order to perform multiplication of matrix $\mathbf{A}$ by vector we have to solve a system with matrix $\mathbf{Q}$ which is sparse (in difference of $\mathbf{Q}^{-1}$), symmetric, and positive definite so conjugate gradient method is a good

approach for this problem, Saad (2000). Even though we do not have any problems with memory now the computational time can be quite large since for each iteration of SymmLQ for $\mathbf{A}$ we have to solve a system with matrix $\mathbf{Q}$ hence we would like to minimize number of these iterations. It can be done by application of a preconditioner – a matrix which is easy to calculate and which is supposed to be close to inverse of $\mathbf{A}$. Unfortunately it is quite hard to develop precoditioner for indefinite symmetric matrix which maintains symmetry. A possible solution is multigrid method which approximates $\mathbf{A}^{-1}$ by an inverse matrix for a coarser grid multiplied by intergrid transfer operators (Bramble (1995)). This approach seems quite promising however intergrid transfer for high order differential operators such as bilaplacian faces a lot of troubles related to approximation of first derivatives.

- We have proved existence of solution only for simplified problem (3.43)-(3.44) and only in assumption that Gaussian curvature Ψ is small, that is the system stays almost in linear regime. However numerical simulations show that the behavior of the system is nonlinear (e.g. existence of bifurcation points demonstrates it). Thus a more profound mathematical research is required to prove existence of solutions in general case.

Bibliography

Asally, M., Kittisopikul, M., Rué, P., Du, Y., Hu, Z., Cagatay, T., Robinson, A., Lu, H., Garcia-Ojalvo, J., and Süel, G. (2012). Localized cell death focuses mechanical forces during 3d pattering in a biofilm. *PNAS*, 109:18891–18896.

Audoly, B., and Boudaoud, A. (2010). Buckling of a stiff film bound to a compliant substrate (part III). Herringbone solutions at large buckling parameter. *J. of the Mech. and Phys. of Solids* 56(7):2444–2458.

Audoly, B. and Pomeau, Y. (2010). *Elasticity and Geometry. From Hair Curls to the Non-linear Response of Shells*. Oxford University Press.

Bais, P.H., Fall, R., Vivanco, J.M. (2004). Biocontrol of Bacillus subtilis against Infection of Arabidopsis Roots by Pseudomonas syringae Is Facilitated by Biofilm Formation and Surfactin Production. *Plant Physiol.* 134(1):307–19.

Ben Amar, M. and Pomeau, Y. (1997). Crumpled paper. *Proc. R. Soc. Lond. A*, 453:729–755.

Bjarnsholt, T., Ciofu, O., Molin, S., Givskov, M., Høiby, N. (2013) Applying insights from biofilm biology to drug development — can a new approach be developed?. *Nat Rev Drug Discov.* 12(10):791–808.

Böl, M., Ehret, A.E., Albero, A.B., Hellriegel, J., Krull, R. (2012). Recent advances in mechanical characterisation of biofilm and their significance for material modelling. *Crit Rev Biotechnol.*, 33(2):145–71.

Braess, D. (2007). *Finite elements: Theory, Fast Solvers, and Applications in Elasticity Theory*. Cambridge University Press, New York.

Bramble, J.H. (1995). *Multigrid methods*. Longman Scientific & Technical, Essex CM20 2JE, England.

Brenner, S.C. and Scott, L.R. (2008). *The Mathematical Theory of Finite Element Methods: Third edition*. Springer.

Brenner, K., You, L., and Arnold, F. H. (2008). Engineering microbial consortia: a new frontier in synthetic biology. *Trends in Biotechnology*, 26(9):483–489.

Brezis, H. (2010). *Functional Analysis, Sobolev Spaces and Partial Differential Equations*. Springer.

Budday, S., Steinmann, P., Kuhl, E. (2014). The role of mechanics during brain development. *J. of the Mech. and Phys. of Solids*, 72:75–92.

Cairns, L.S., Hobley, L., Stanley-Wall, N.R. (2014). Biofilm formation by Bacillus subtilis: new insights into regulatory strategies and assembly mechanisms. *Mol Microbiol.*, 93(4):587-98.

Cerda, E. and Mahadevan, L. (1997). Conical Surfaces and Crescent Singularities in Crumpled Sheets. *Phys. Rev. Lett.*, 80(11):2358–2361.

Cerda, E. and Mahadevan, L. (2003). Geometry and physics of wrinkling. *Phys. Rev. Lett.*, 90:074302.

Chai, L., Vlamakis, H., Kolter, R. (2011). Extracellular signal regulation of cell differentiation in biofilms. *MRSBulletin*, 36(5):374–379.

Chen, X. and Hutchinson, J. W. (2004). Herringbone buckling patterns of compressed thin films on compliant substrate. *J. Appl. Mech.*, 71:594–603.

Ciarlet, P.G. (1997) *Mathematical elasticity. Volume II: Theory of Plates*. Elsevier.

Ciarlet, P.G., Gratie, L. (2006). On the Existence of Solutions to the Generalized Marguerre-von Kármán Equations. *Mathematics and Mechanics of Solids*, 11:83–100.

Ciarlet, P.G., Gratie, L., Sabu, N. (2001). An Existence Theorem for Generalized von Kármán Equations. *Journal of Elasticity*, 62:239–248.

Cogan, N.G., Keener, J.P. (2004) The Role of the Biofilm Matrix in Structural Development. *Math Med Biol.*, 21(2):147-66.

Costerton, J. W., Cheng, K.-J., Geesey, G. G., Ladd, T. I., Nickel, J. C., Dasgupta, M., and Marrie, T. J. (1987). Bacterial biofilms in nature and disease. *Ann. Rev. Microbiol.*, 41:435–464.

Costerton, J.W. and Lewandowski, Z. (1995). Microbial biofilms. *Annu Rev Microbiol.*, 49:711–45.

Costerton, J.W., Stewart, P.S., Greenberg, E.P. (1999). Bacterial biofilms: a common cause of persistent infections. *Science*, 284(5418):1318–22.

Dervaux, J. and Ben Amar, M. (2008). Morphogenesis of growing soft tissues. *Phys. Rev. Lett.*, 101:068101.

Dervaux, J., Ciarletta, P., and Ben Amar, M. (2009). Morphogenesis of thin hyperelastic plates: A constitutive theory of biological growth in the Föppl-von Kármán limit. *J. Mech. Phys. Solids*, 57:458–471.

Dhami N.K.,Reddy S.M., Mukherjee A. (2013). Biomineralization of calcium carbonates and their engineered applications: a review. *Front Microbiol.*, 4:314.

Dockery, J., Klapper, I. (2002). Finger Formation in Biofilm Layers. *SIAM J. Appl. Math.*, 62(3):853–869.

Eberl, H.J., Khassehkhana, H., Demaret, L.(2010). A mixed-culture model of a probiotic biofilm control system. *Comp. and Math. Methods in Medicine*, 11(2):99–118.

Eberl, H.J., Parker, D.F., van Loosdrecht, Mark C.M. (2001). A new deterministic spatio-temporal continuum model for biofilm development. *J. of Theoretical Medicine*, 3:161–175.

Espeso, D., Carpio, A., and Einarsson, B. (2015). Differential growth of wrinkled biofilms. *Phys. Rev. E*, 91:022710.

Flemming, H.-C. and Wingender, J. (2010). The biofilm matrix. *Nature Reviews (Microbiology)*, 8:623–633.

Fukaya, M., Park, Y.S., Toda, K. (1992). Improvement of acetic acid fermentation by molecular breeding and process development. *J. of Appl. Bacteriol.*, 73:447-454.

Goriely, A. and Ben Amar, M. (2007). On the definition and modeling of incremental, cumulative, and continuous growth laws in morphoelasticity. *Biomech Model Mechanobiol.* 6(5):289–96.

Gross, R., Lang, K., Buühler, K., Schmid, A. (2009). Characterization of a Biofilm Membrane Reactor and Its Prospects for Fine Chemical Synthesis. *Biotechnol Bioeng.*, 105(4):705–17.

Guelon, T., Mathias, J.-D., Stoodley, P. (2011). Advances in Biofilm Mechanics. *In: Flemming HC., Wingender J., Szewzyk U. (eds) Biofilm Highlights. Springer Series on Biofilms.* vol 5. Springer, Berlin, Heidelberg

Hall, W.C. and Mah, T.-F. (2017). Molecular mechanisms of biofilm-based antibiotic resistance and tolerance in pathogenic bacteria. *FEMS Microbiol Rev.*, 41(3):276–301.

Hammond, J.F., Stewart, E.J., Younger, J.G., Solomon, M.J., Bortz, D.M.(2014). Variable Viscosity and Density Biofilm Simulations using an Immersed Boundary Method, Part I: Numerical Scheme and Convergence Results. *J. of Comp. Phys.*, 317:204–222.

Hentzer, M., Teitzel, G.M., Balzer, G.J., Heydorn, A., Molin, S., Givskov, M., Parsek, M.R. (2001). Alginate Overproduction Affects *Pseudomonas aeruginosa* Biofilm Structure and Function. *J Bacteriol.*, 183(18):5395–401.

Hobley, L., Harkins, C., MacPhee, C. E., and Stanley-Wall, N. R. (2015). Giving structure to the biofilm matrix: an overview of individual strategies and emerging common themes. *FEMS Microbiology Reviews*, 39:649–669.

Hobley, L., Ostrowski, A., Rao, F.V., Bromley, K.M., Porter, M., Prescott, A.R., MacPhee, C.E., van Aalten D.M.F., Stanley-Wall, N.R. (2013). BslA is a self-assembling bacterial hydrophobin that coats the Bacillus subtilis biofilm. *Proc Natl Acad Sci USA*, 110(33):13600-5.

Horn, H. and Lackner, S. (2014). Modeling of Biofilm Systems: A Review. *Adv Biochem Eng Biotechnol.*, 146:53-76.

Høiby, N., Bjarnsholt, T., Moser, C., Bassi, G.L., Coenye, T., Donelli, G., Hall-Stoodley, L.,Hola, V.,Imbert, C., Kirketerp-Moller, K., Lebeaux, D., Oliver, A., Ullmann, A.J., Williams, C. (2015). ESCMID guideline for the diagnosis and treatment of biofilm infections 2014. *Clin. Microbiol. and Inf.* 21:S1–S25.

Huang, J., Davidovitch, B., Santangelo, C., Russel, T., and Menon, N. (2010). Smooth cascade of wrinkles at the edge of a floating elastic film. *Phys. Rev. Lett.*, 105:038302.

Huang, R. (2005). Kinetic wrinkling of an elastic film on a viscoelastic substrate. *J. Mech. Phys. Solids*, 53:63–89.

Huang, R. and Im, S. H. (2006). Dynamics of wrinkle growth and coarsening in stressed thin films. *Phys. Rev. E*, 74:026214.

Huang, R. and Suo, Z. (2002a). Instability of a compressed elastic film on a viscous layer. *Int. J. Solids Structures*, 39:1791–1802.

Huang, R. and Suo, Z. (2002b). Wrinkling of a compressed elastic film on a viscous layer. *J. Appl. Phys.*, 91:1135–1142.

Huang, Z., Hong, W., and Suo, Z. (2005). Nonlinear analysis of wrinkles in a film bonded to a compliant substrate. *J. Mech. Phys. Solids*, 53:2101–2118.

Hughes, T. J. R. (2000). *The finite element method. Linear static and dynamic finite element analysis*. Dover.

Iakunin, S., Bonilla, L.L. (2018). Variational formulation, asymptotic analysis, and finite element simulation of wrinkling phenomena in modified plate equations modeling biofilms growing on agar substrates. *Comp. Methods in Appl. Mech. and Engineering*, 333:257–286.

Jamal, M., Ahmad, W., Andleeb, S., Jalil, F., Imran, M., Nawaz, M.A., Hussain, T., Ali, M., Rafiq, M., Kamil, M. A. (2018). Bacterial biofilm and associated infections. *J Chin Med Assoc.*, 81(1):7–11.

Klapper, I., Dockery, J. (2010). Mathematical Description of Microbial Biofilms. *SIAM Review*, 52(2):221–265.

Kreyszig, E. (1978). *Introductory Functional Analysis with Applications*. John Wiley & Sons.

Kücken, M. and Newell, Alan C. (2005). Fingerprint formation. *J. of Theor. Biol.*, 235(1):71–83.

Landau, L. D. and Lifshitz, E. M. (1986). *Theory of Elasticity*. Pergamon Press, 3rd ed.

Laspidou, C.S., Rittmann, B.E. (2004) Modeling the development of biofilm density including active bacteria, inert biomass, and extracellular polymeric substances. *Water Res.*, 38(14-15):3349–61.

Laspidou, C.S., Spyrou, L.A., Aravas, N., Rittmann, B.E. (2014). Material modeling of biofilm mechanical properties. *Math. Biosci.*, 251:11–15.

Lions, J.L. (1969). *Some methods for solution of nonlinear boundary value problems*. Dunod-Gauthier-Villars, Paris.

Lewicka, M., Mahadevan, L., and Pakzad, M. (2011). The Föppl-von Kármán equations for plates with incompatible strains. *Proceedings of the Royal Society A*, 467:402–426.

López, D., Vlamakis, H., Losick, R., and Kolter, R. (2009). Cannibalism enhances biofilm development in bacillus subtilis. *Mol. Microbiol.*, 74(3):609–618.

Martínez, J.L, and Rojo, F. (2011). Metabolic regulation of antibiotic resistance. *FEMS Microbiol Rev.*, 35(5):768–89.

Mattei, M.R., Frunzo, L., D'Acunto, B., Pechaud, Y., Pirozzi, F., Esposito, G. (2017). Continuum and discrete approach in modeling biofilm development and structure: a review. *J. Math. Biol.*, 76:945–1003

Monds, R.D. and O'Toole, G.M. (2010). The developmental model of microbial biofilms: ten years of a paradigm up for review. *Trends Microbiol.*, 17(2):73–87.

Mora, T. and Boudaoud, A. (2006). Buckling of swelling gels. *Eur. Phys. J. E*, 20:119–124.

Naumann, J. (1974). An Existence Theorem for the v. Karman Equations under the Condition of Free Boundary. *Aplikace matematiky*, 19(1):17–27.

Nyholm, S.V., Stabb, E.V., Ruby, E.G., McFall-Ngai, M.J. (2000). Establishment of an animal-bacterial association: Recruiting symbiotic vibrios from the environment. *PNAS*, 97(18):10231–10235.

Oyen, M. (2014). Mechanical characterisation of hydrogel materials. *International Materials Reviews*, 59:44–59.

Paige, C.C., Saunders, M.A. Solution of Sparse Indefinite Systems of Linear Equations. *SIAM J. Numer. Anal.*, 12(4):617–629.

Peker A.S., Lavery J.E., Fang S.-C. (2007). A reduced Hsieh–Clough–Tocher element with splitting based on an arbitrary interior point. *J. of Math. Anal. and Appl.*, 333(1):500–504.

Picioreanu, C., van Loosdrecht, Mark C.M., Heijnen, J.J. (1998). A New Combined Differential-Discrete Cellular Automaton Approach for Biofilm Modeling: Application for Growth in Gel Beads. *Biotechnol Bioeng.*, 57(6):718–31.

Reddy, J. N. (2003). *Mechanics of Laminated Composite Plates and Shells. Theory and Analysis*. CRC Press LLC

Rodriguez, E., Hoger, A., and McCulloch, A. (1994). Stress-dependent finite growth in soft elastic tissues. *J. Biomech*, 27(4):455–467.

Römling, U., Kjelleberg, S., Normark, S., Nyman, L., Uhlin, B.E., Akerlund, B. (2014). Microbial biofilm formation: a need to act. *J Intern Med.*, 276(2):98–110.

Saad, Y. (2000). *Iterative Methods for Sparse Linear Systems*. SIAM.

Seminara, A., Angelini, T., Wilking, J., Vlamakis, H., Ebrahim, S., Kolter, R., Weitz, D., and Brenner, M. (2012). Osmotic spreading of bacillus subtilis biofilm driven by an extracellular matrix. *PNAS*, 109:1116–1121.

Sonner, S., Efendiev, M., Eberl, H. (2015). *On the well-posedness of mathematical models for multicomponent biofilms. Math. Meth. Appl. Sci.*, 38:3753–3775.

Stotsky, J.A., Hammond, J.F., Pavlovsky L., Stewart, E.J., Younger, J.G., Solomon, M.J., Bortz, D.M. (2016). Variable Viscosity and Density Biofilm Simulations using an Immersed Boundary Method, Part II: Experimental Validation and the Heterogeneous Rheology-IBM. *J. of Comp. Phys.*, 317:204–222.

Trejo, M., Dourarche, C., Bailleux, V., Poulard, C., Mariot, S., Regeard, C., and Raspaud, E. (2013). Elasticity and wrinkled morphology of bacillus subtilis pellicles. *PNAS*, 110:2011–2016.

Turcotte, D.L. and Schubert, G. (1982). *Geodynamics*. Cambridge.

Wallace, H.A. (2016). *Mathematical Modelling of Wrinkle Formation in Bacterial Biofilms*. PhD thesis, University of Dundee, Dundee.

Wanner O. and Gujer W. (1986). A Multispecies Biofilm Model. Biotechnology and Bioengineering, XXVIII:314-328.

Wilking, J. N., Angelini, T. E., Seminara, A., Brenner, M. P., and Weitz, D. A. (2011). Biofilms as complex fluids. *MRS Bull.*, 36:385–391.

Wilking, J. N., Zaburdaev, V., Volder, M. D., Losick, R., Brenner, M., and Weitz, D. (2013). Liquid transport facilitated by channels in bacillus subtilis biofilms. *PNAS*, 110:848–852.

Witten, T.A. (2007). Stress focusing in elastic sheets. *Rev. Mod. Phys.* 79:643.

Xavier, J.B. and Foster, K.R. (2006). Cooperation and conflict in microbial biofilm. *PNAS*, 104(3):876–881.

Zhang, C., Li, B., Huang, X., Ni, Y., Feng, X.-Q., (2016) Morphomechanics of bacterial biofilms undergoing anisotropic differential growth. *Appl. Phys. Lett.* 109:143701.

Zienkiewicz, O. and Taylor, R. (2005). *The Finite Element Method. Method for Solid and Structural Mechanics*. Elsevier-Butterworth-Heinemann, 6th ed.